ARTICLE IN PRESS

Nature Communications

https://doi.org/10.1038/s41467-026-72247-5

Article in Press

Multiomics immune profiling of a patient-relevant orthotopic lung cancer model using SEPARATE-Seq

Received: 13 February 2025

Accepted: 9 April 2026

[redacted]

Cite this article as: Bardet, P.M., Allonsius, L., Hadadi, E. *et al.* Multiomics immune profiling of a patient-relevant orthotopic lung cancer model using SEPARATE-Seq. *Nat Commun* (2026). https://doi.org/10.1038/s41467-026-72247-5

Pauline M. R. Bardet, Lize Allonsius, Eva Hadadi, Daliya Kancheva, Morgane Paque, Sarka Vosahlikova, Aarushi A. Caro, Anouk Van Audenhove, Ayla Debraekeleer, Ria Roelandt, Kevin Verstaen, Michal Hensler, Delphine Hoton, Gisèle Mateu Cabrera, Louis Boon, Arnaud Blomme, Sofie Deschoemaeker, Geert Raes, Elly Marcq, Ahmed E. I. Hamouda, Jan P. Böttcher, Jitka Fucikova, Pierre Close, Frank Aboubakar Nana & Damya Laoui

We are providing an unedited version of this manuscript to give early access to its findings. Before final publication, the manuscript will undergo further editing. Please note there may be errors present which affect the content, and all legal disclaimers apply.

If this paper is publishing under a Transparent Peer Review model then Peer Review reports will publish with the final article.

ARTICLE IN PRESS

© The Author(s) 2026. **Open Access** This article is licensed under a Creative Commons Attribution-NonCommercial-NoDerivatives 4.0 International License, which permits any non-commercial use, sharing, distribution and reproduction in any medium or format, as long as you give appropriate credit to the original author(s) and the source, provide a link to the Creative Commons licence, and indicate if you modified the licensed material. You do not have permission under this licence to share adapted material derived from this article or parts of it. The images or other third party material in this article are included in the article's Creative Commons licence, unless indicated otherwise in a credit line to the material. If material is not included in the article's Creative Commons licence and your intended use is not permitted by statutory regulation or exceeds the permitted use, you will need to obtain permission directly from the copyright holder. To view a copy of this licence, visit http://creativecommons.org/licenses/by-nc-nd/4.0/.

Multiomics immune profiling of a patient-relevant orthotopic lung cancer model using SEPARATE-Seq

Pauline M.R. Bardet[1,2,#], Lize Allonsius[1,2,#], Eva Hadadi[1,2,#], Daliya Kancheva[1,2], Morgane Paque[3], Sarka Vosahlikova[4], Aarushi A. Caro[1,2,5], Anouk Van Audenhove[1,2,6], Ayla Debraekeleer[1,2], Ria Roelandt[7,8], Kevin Verstaen[7,8], Michal Hensler[4], Delphine Hoton[9], Gisèle Mateu Cabrera[1,2], Louis Boon[10], Arnaud Blomme[3,11], Sofie Deschoemaeker[1,2], Geert Raes[1,2], Elly Marcq[1,2], Ahmed E.I. Hamouda[1,2], Jan P. Böttcher[12,13], Jitka Fucikova[4,14], Pierre Close[3,15], Frank Aboubakar Nana[6,16], Damya Laoui[1,2,*]

[1]Laboratory of Dendritic Cell Biology and Cancer Immunotherapy, VIB Center for Inflammation Research, Brussels, Belgium.

[2]Lab of Cellular and Molecular Immunology, Brussels Center of Immunology, Vrije Universiteit Brussel, Brussels, Belgium.

[3]Laboratory of Cancer Signaling, GIGA-Institute, University of Liège, Liège, Belgium.

[4]Sotio Biotech a.s., Prague, Czech Republic.

[5]Lab of Tumor Immunology and Immunotherapy, Department of Oncology, Leuven Cancer Institute, KU Leuven; Leuven, Belgium

[6]Institut de Duve, Université Catholique de Louvain, Brussels, Belgium

[7]VIB Single Cell Core, VIB, Ghent/Leuven, Belgium.

[8]Department of Biomedical Molecular Biology, Ghent University, Ghent, Belgium.

[9]Department of Pathology, Cliniques universitaires Saint Luc, Université catholique de Louvain (UCLouvain), Brussels, Belgium.

[10]JJP Biologics, Warsaw, Poland.

[11]Laboratory of Metabolic Regulation, GIGA-Institute, University of Liège, Liège, Belgium.

[12]Department of Experimental Immunology, Institute of Immunology, University of Tübingen, Tübingen, Germany.

[13]Institute of Molecular Immunology, TUM University Hospital, School of Medicine and Health, Technical University of Munich (TUM), Munich, Germany.

[14]Department of Immunology, Charles University, 2nd Faculty of Medicine and University Hospital Motol, Prague, Czech Republic.

[15]WELBIO department, WEL Research Institute, avenue Pasteur, 6, Wavre, Belgium

[16]Service de Pneumologie, Cliniques Universitaires Saint-Luc, Brussels, Belgium.

[#]These authors contributed equally

[*]Correspondence: dlaoui@vub.be

ABSTRACT

Relevant pre-clinical models are essential for driving progress in cancer therapy research. Here, we develop a pre-clinical study framework using an injectable orthotopic lung adenocarcinoma (LUAD) model (ORTHO) that replicates key features of human LUAD patients and is dissectible into tumoural and non-tumoural adjacent tissue, in analogy with patient samples. We also present SEPARATE-Seq, a broadly applicable technique enabling the partitioning of vascular and intratissue immune cells along with scRNA-Seq. By applying both SEPARATE-Seq and spatial transcriptomics to our dissectible ORTHO model, we confirm that our model replicates key immune features of human LUAD patients. Similarly to these patients, we observe NK-cell dysfunction and neutrophil dichotomy, and show that these are affected by their vascular/intratissue or tumour/adjacent location, highlighting the need for these spatial distinctions. Additionally, we show that several immune populations are restricted to specialised, local niches within the tumour, including a ring of lipid-associated TAMs lining the tumour edge and hubs of interferon-stimulated cells. Overall, our resource, available through an interactive tool, provides a comprehensive multiomics immune characterisation of a reproducible pre-clinical LUAD mouse model.

INTRODUCTION

Worldwide, lung cancer is the most prevailing and deadliest cancer type, with almost 2.5 million newly diagnosed cases and over 1.8 million deaths in 2022[1]. Non-small cell lung cancer (NSCLC) is the most common type of lung cancer, accounting for approximately 90% of all lung cancer cases, and is further classified according to histological subtypes, with lung adenocarcinoma (LUAD) and squamous cell carcinoma (LUSC) being the most common[2]. Immune cells infiltrate the tumour microenvironment (TME) of NSCLC in large numbers, making up more than 50% of its total cellular composition. The main tumour-infiltrating immune fraction in NSCLC is comprised of neutrophils, T cells and B cells[3,4]. The presence of each of these has been linked to both better and worse prognoses[5–9], highlighting their broad diversity and the need for a better understanding of specific cell subsets and states. These cell-specific analyses and their resulting therapeutic research have mainly been performed in pre-clinical mouse models. To enable the effective translation of such pre-clinical research to clinical applications, it is essential to use appropriate and representative (animal) models. The available pre-clinical lung cancer models range from spontaneous and inoculable mouse models to innovative organoid and organ-on-a-chip models[10,11]. The advantage of using inoculable (syngeneic) models lies in their relatively fast tumour growth, the presence of a fully functional immune system, reproducibility, and the relative ease, cost and availability compared to genetically engineered mouse models. Historically, syngeneic subcutaneous tumour models have played a crucial role in cancer research, but their drawbacks are significant, specifically when focusing on the immune compartment. Indeed, under homeostatic conditions, the lung harbours a vast array of immune cells, comprised of alveolar (AMs) and interstitial macrophages (IMs), dendritic cells (DCs), neutrophils, T and B cells, among others[12], which all can play a part in anti-/pro-tumour immune responses[13–17]. Hence, there is a need for models that combine the advantages of subcutaneous models, while also capturing the immune complexity of the lung environment.

In this paper, we introduce an LLC-Thy1.1 orthotopic murine LUAD model (ORTHO), where adjacent non-tumoural tissue can be precisely dissected from tumour nodules, allowing the simultaneous characterisation of the immune cell composition in both compartments individually, similar to what is routinely done for patient samples. We performed a complete multiomics immune profiling of this ORTHO model, using multiparameter flow cytometry, spatial transcriptomics (Vizgen MERSCOPE), and scRNA-/CITE-Seq (10X Genomics) coupled with our newly developed SEPARATE-Seq (**S**treptavidin **E**nabled **PAR**titioning **A**nd **T**ag **E**valuation for RNA-**Seq**uencing) technique. SEPARATE-Seq enables the characterisation of (post-perfusion) vascular and intratissue (immune) cells separately and can be widely applied to (other) biological research fields wherein this vascular-intratissue separation exists. As such, we show that the ORTHO model replicates specific tumour-driven immune phenotypes and features observed in patients, such as NK-cell dysfunctionality, T cell exhaustion and regulatory T cell (Treg) increase in the tumour, neutrophil dichotomy in adjacent *versus* tumour tissue, and the exclusion of AMs from the tumour. Moreover, we reveal distinct spatial patterns within ORTHO tumours, including the formation of a ring-like structure of lipid-associated macrophages along the tumour edge and the presence of defined hubs composed of immune and non-immune cell subsets with an interferon-stimulated gene (ISG) signature, an architecture that is recapitulated in tumours of LUAD patients. Overall, we provide a thoroughly characterised pre-clinical LUAD model, with the SEPARATE-Seq data made available through an interactive webtool (https://single-cell.be/Laouimmunology/SEPARATESeq).

RESULTS

Introducing a reproducible LLC-derived orthotopic NSCLC model

To investigate how the immune compartment of the widely used subcutaneous LLC murine model[18] diverges from human disease, we analysed scRNA-Seq data on FACS-isolated viable CD45$^+$ cells and compared the immune composition to that of human LUAD tumours, using the publicly available NSCLC scRNA-Seq atlas generated by Salcher *et al.*[14] (Fig. 1A-1B). Within the human NSCLC atlas, we only retained studies that sequenced either the whole tissue or sorted CD45$^+$ cells (106 LUAD patients; Supplementary Data 1) to ensure that quantitative information could be obtained. However, it is important to acknowledge that certain immune cells are more challenging to capture via scRNA-Seq, exemplified by human neutrophils which are underrepresented in this dataset[3,14]. After cell cluster annotation using canonical markers (Supplementary Fig. 1A-1B), a large contrast in lymphoid representation was observed when comparing the immune composition of subcutaneous tumours with LUAD tumours of patients. B, T and NK cells accounted for less than 5% in subcutaneous LLC tumours, whereas these lymphoid cells made up over 50% of the total immune compartment in LUAD tumours (Fig. 1C)[3,4].

To counter this mouse-human discrepancy and incorporate the important role of the lung environment, we evaluated several injectable orthotopic models based on the following criteria: (1) high technical feasibility and reproducibility, (2) ease of separating tumour nodules from adjacent non-tumoural tissue, as typically done for patient samples (Fig. 1C, 1D), and (3) ethical considerations, including reducing the number of animals and minimising suffering. We used an LLC-Thy1.1 cell line, allowing Thy1.1$^+$ cancer cell identification via flow cytometry, and compared retro-orbital (RO), transthoracic (TT), intratracheal with intubation (ITI) and direct intratracheal (ITD) inoculations (Fig. 1E). RO and TT routes were withdrawn due to adverse side effects (occasional eye tumour occurrence upon RO inoculation) or technical difficulties (tumour growth inside the pleural cavity upon TT inoculation) (Supplementary Fig. 2A). Both ITI and ITD models generated easily dissectible tumour nodules, but ITD was technically easier and faster to perform (Supplementary Movie 1). ITD (further referred to as ORTHO) was therefore chosen as the preferred method and resulted in tumours that could easily be followed up via micro computed tomography (µCT) (Supplementary Fig. 2B). To increase tumour take rates, we passaged the original LLC-Thy1.1 cell line (P0) twice *in vivo*, yielding the LLC-Thy1.1 P2 (P2) cell line (Fig. 1F-1G), which showed significant increase in take rate when inoculated using the ITD/ORTHO method (Fig. 1G, Supplementary Fig. 2C). To evaluate the relevance of the LLC-Thy1.1 P2 ORTHO model to human LUAD, we performed histopathological analysis and benchmarked it against the widely used $\mathrm{Kras}^{\mathrm{LSL\text{-}G12D/+}}$;$\mathrm{Trp53}^{\mathrm{fl/fl}}$ (KP) genetically engineered LUAD model. While both models recapitulated features of human LUAD tumours (Supplementary Fig. 2D), they represented different disease grades. The KP model resembled more differentiated tumours with mixed acinar (grade 2), papillary (grade 2), and solid (grade 3) components, whereas the LLC-Thy1.1 P2 ORTHO model displayed a more aggressive, high-grade, uniformly solid and sarcomatoid (grade 3) LUAD phenotype. Importantly, consistent with most human LUAD cases, tumour growth in the ORTHO model was predominantly localised, whereas the KP model developed widely spread multifocal primary tumours, a pattern that can occur in patients but is less commonly observed (Supplementary Fig. 2E).

Additionally, the ORTHO model is compatible with both male and female mice. At comparable tumour volumes, no significant differences were observed in the overall immune cell composition between sexes, although there was a trend toward increased neutrophil infiltration in male samples (Supplementary Fig. 3A-D).

To unravel the intrinsic differences between the P0 and P2 cell lines, we conducted a crystal violet colony formation assay and a limiting dilution spheroid assay. Unexpectedly, P2 cells formed fewer colonies than P0 in the proliferation assay (Supplementary Fig. 4A) and displayed inferior spheroid formation potential at lower dilutions (50 and 100 cells) (Supplementary Fig. 4B), conflictingly suggesting that P2 hold a smaller proportion of tumour initiating cells. Moreover, the tumour mutational burden (TMB) did not reveal a difference between the two cell lines ($\mathrm{TMB}_{\mathrm{P0}}$=13.0, $\mathrm{TMB}_{\mathrm{P2}}$=13.2) and were in line with reported LUAD patient TMBs (11.8-12.9, 95% confidence interval)[19]. Next, we performed scRNA-Seq on the P0 and P2 cell lines (Supplementary Fig. 4C-4D). Gene set enrichment analysis (GSEA) using the MSigDB database highlighted a positive enrichment for "MYC_TARGETS_V1", "MYC_TARGETS_V2", "G2M_CHECKPOINT" and "INFLAMMATORY_RESPONSE" in P2 *versus* P0 cells (Supplementary Table 1). At the protein level, tumourigenic pTBK1, and to some extent also c-Myc oncoprotein expression were enhanced in the P2 cell line (Supplementary Fig. 4E).

Interestingly, scRNA-Seq revealed that our P2 cell line was heterogeneous and subclustered in $Ly6a^{+}$ and $Ly6a^{-}$ P2 cell states, which could also be distinguished by flow cytometry (Fig. 1H, Supplementary Fig. 4F-

2H). Previously, Ly-6A/E (Sca-1) has been identified as a cancer stem cell marker in murine gastric cancer cells, with Sca-1^{high} cells showing an increased tumourigenic potential[20]. The *Ly6a*$^{+}$ P2 cluster also showed enhanced *Ly6c1*, *Krt8* and *Krt18* expression (Supplementary Fig. 4F), markers which have been associated with increased invasiveness[21,22]. Upon culture of sorted Ly-6A/E^{+}Ly-6C^{+} or Ly-6A/E^{-}Ly-6C^{-} P2 cells (hereafter referred to as Ly-6A^{+} and Ly-6A^{-}, respectively), the bimodal Ly-6A/E and Ly-6C expression reappeared in both parent populations, suggesting that these represent dynamic cell states, rather than intrinsic cell clones (Supplementary Fig. 4H). Additionally, we evaluated cell death and cell cycle activity using flow cytometry and applied the CellCycleScoring function to the scRNA-Seq data to assess cell cycle phases. The Ly-6A^{+} P2 state exhibited higher viability and a stronger tendency for proliferation compared to the Ly-6A^{-} cells (Supplementary Fig. 4I-4K), suggesting that the Ly-6A^{+} P2 may represent the main tumour-initiating subset despite the contrasting *in vitro* growth results. This is in line with findings in a *Kras*$^{lox\text{-}stop\text{-}lox(lsl)\text{-}G12D/+}$; *p53*$^{flox/flox}$ (KP)-derived model, where *Sca-1*$^{+}$ cells were identified as the population with the highest tumour-propagation, self-renewal and differentiation capacity *in vivo*[23].

Overall, we developed an LLC-derived cell line with a high and reproducible tumour take rate when inoculated orthotopically in the lungs.

SEPARATE-Seq allows for the compartmentalisation of immune cells into vascular and intratissue populations

Immune cells in the lung reside in distinct compartments, of which the major are the alveolar space, the interstitial/intratissue compartment and the vascular compartment. The latter harbours circulating blood cells, which can be cleared out via cardiac perfusion, but also intravascular marginated/adhered cells that persist after cardiac perfusion[24,25]. To unravel which immune cells reside in the distinct lung compartments, we present SEPARATE-Seq (**S**treptavidin **E**nabled **PAR**titioning **A**nd **T**ag **E**valuation for RNA-**Seq**uencing). This technique involves intravenous injection (via the retro-orbital sinus) of a biotinylated CD45-specific antibody simultaneously with overdose of anaesthetics, followed by *ex vivo* extracellular labelling with oligonucleotide-STREP conjugates (Fig. 2A). The STREP-tags specifically labelled the vascular cells and not the intratissue and alveolar cells[24]. Fluorescent STREP conjugates were used in parallel to also assess the compartmentalisation of immune cells via flow cytometry on the same samples. We performed this experimental procedure on three distinct mice cohorts: (1) subcutaneous LLC-Thy1.1 P2 tumour-bearing mice (SUBCUT); (2) ORTHO LLC-Thy1.1 P2 tumour-bearing mice, from which tumour tissue (ORTHO-Tumour, ORTHO-T) and adjacent tissue (ORTHO-Adjacent, ORTHO-A) were dissected; and (3) ORTHO HBSS mock-inoculated mice (ORTHO-Mock, ORTHO-M). Additionally, for SEPARATE-Seq, antibody hashing with hashtag oligos (HTOs) was performed to enable deconvolution into individual murine samples and to match adjacent and tumour tissues from individual ORTHO-inoculated mice after sequencing.

The HTO and STREP demultiplexing steps were optimised, whereby three different algorithms (HTODemux[26], DeMULTIplex[27] and DeMULTIplex2[28]) with varying quantile settings (Q) were compared

(Supplementary Fig. 5A, Supplementary Data 2). Optimisation criteria for the algorithm choice included the maximisation of (1) the number of recovered demultiplexed vascular and intratissue cells and (2) the correlation with flow cytometry data for the proportion of vascular/intratissue immune cells. Differences in affinity of the HTO/biotinylated CD45 antibodies to distinct cell types could potentially lead to variability in the HTO/STREP counts. To test for this, we ran the demultiplexing methods either in the whole dataset or for each major cell type separately (respectively *algorithm* and *algorithm*_CT in Supplementary Fig. 5B), which did not improve the amount of HTO$^+$ cells (Supplementary Fig. 5B, Supplementary Data 2). The demultiplexed cells were then assigned as intratissue (HTO$^+$STREP$^-$) or vascular (HTO$^+$STREP$^+$). Importantly, we enforced an additional criterium for vascular cells, whereby only matching HTO and STREP cells were retained (e.g. STREP1-HTO1 cells were retained, but not STREP1-HTO4). Finally, DeMULTIplex2 (for HTO) and DeMULTIplex Q0.9 (for STREP) were selected as the most optimal (Supplementary Fig. 5C-5D), as this combination provided the best cell recovery rate and correlation between SEPARATE-Seq and our paired flow cytometry data (Supplementary Fig. 5E, Supplementary Data 2).

SEPARATE-Seq was performed on FACS-isolated viable CD45$^+$ cells for the four different sample types (SUBCUT, ORTHO-T, ORTHO-A, ORTHO-M) and datasets were merged for analysis, allowing the identification of main immune cell types based on the expression of canonical mRNA and protein markers (Fig. 2B, Supplementary Fig. 5F, Supplementary Table 2). The HTO labelling allowed us to visualise how the frequencies of immune cell types varied in individual samples and in samples originating from the same mice in the case of ORTHO-T/-A (Supplementary Fig. 6A-6B). Intriguingly, the SEPARATE-Seq vascular-intratissue separation revealed that a large fraction of immune cells, mainly neutrophils and lymphoid cells, resided in the post-perfusion vasculature of the lung tissue, and demonstrated that the different immune cell types localised distinctly across the sample types (Fig. 2C, 2E). A similar separation between the vascular and intratissue compartment was observed via flow cytometry (Fig. 2D), where the main cell populations in each sample type were identified via canonical markers (Supplementary Fig. 3D, Supplementary Fig. 6C, 6D).

In all, we introduced SEPARATE-Seq, an scRNA-Seq based method that enables the differentiation of distinct immune cell populations based on their intravascular or intratissue localisation and showcased this application in murine lung cancer.

Spatial transcriptomics maps the cell types identified through SEPARATE-Seq

To assess how distinct cell types identified by SEPARATE-Seq, were spatially distributed in P2 tumour-bearing lungs, we performed targeted spatial transcriptomics using the Vizgen MERSCOPE spatial profiling platform (Fig. 3A, Supplementary Table 3, n=2). Individual tumours were delineated from adjacent tissue based on DAPI staining and the tumour core was set as the centroid of the tumour (Fig. 3A). Immune and non-immune cells were subclustered separately and annotated based on relevant marker genes (Fig. 3B, Supplementary Fig. 7A, 7B, 8, Supplementary Table 4). We were able to identify the same main immune cell types by SEPARATE-Seq and spatial transcriptomics and observed similar trends in cell ratios across adjacent and tumour tissue with both techniques (Fig. 3B). Of note, neutrophil identification on a spatial level was cumbersome as *Ly6g, S100a8* and *S100a9* were non-targetable. Hence, neutrophils were identified using a combination of the non-canonical markers *Il1b, Mmp9, Cxcr2 and Hdc* (Supplementary Table 4, Supplementary Fig. 8), likely leading to their underrepresentation (Fig. 3B).

While our 287-gene panel was mainly immune-focussed (Supplementary Table 3), we could also confidently identify various non-immune cells (Fig. 3A, Supplementary Fig. 7A-7B, Supplementary Table 4). We found that most epithelial cells (alveolar type 1 (AT1), AT2 and ciliated cells) were enriched in the adjacent tissue (Supplementary Fig. 7B). Among mesenchymal cells, smooth muscle cells (SMCs) predominantly localised in the adjacent tissue, whereas distinct fibroblast states resided in different regions within the tumour. While *Lrrc15*$^{+}$ fibroblasts, previously reported to be pro-tumoural and terminally differentiated[29,30], were found within the tumour core, *Ptgs2*$^{+}$ fibroblasts were dispersed across the tumour (Supplementary Fig. 7B). Moreover, *Plau* (encoding uPA) expression was higher in tumour-restricted fibroblasts (Supplementary Fig. 7B, 8, Supplementary Table 4), in line with the increased uPA secretion by cancer associated fibroblasts (*versus* normal fibroblasts) reported in oesophageal squamous cell carcinoma patients[31].

Lastly, endothelial cells (ECs) could be differentiated based on *Hif1a* expression, with *Hif1a*$^{+}$ ECs localising within the tumour (Supplementary Fig. 7B, 8, Supplementary Table 4) and co-expressing *Ndrg1*, which was shown to be increased in ECs upon hypoxic exposure[32]. This points to a hypoxic and inflammatory remodelling of ECs and fibroblasts within the tumour.

NK cells adopt an immature, dysfunctional state upon tumour entry

To further explore the diverse cell states and their distribution in LUAD tumours and adjacent tissue, we subclustered the myeloid and lymphoid cells individually in the human dataset (Fig. 4A-4C, Supplementary Fig. 9A-9C). We confirmed that the annotated cell types in the human (tumour and adjacent tissue) and mouse (ORTHO-T/-A) datasets show a high degree of correlation at the average gene expression levels, both at the general annotation level and at the deeper cell subtype level (Supplementary Fig. 10).

Considering that within the immune compartment, lymphoid cells were underrepresented in the subcutaneous LLC tumour model as compared to patient samples, we initially set out to explore these in the orthotopic setting.

In our ORTHO model, we observed a maturity shift in the NK-cell compartment from ‘mature’ *Itgam*$^{+}$ (encoding CD11b) CD27^{-} NK cells (Mature NK; *Klrg1*/KLRG1, *S1pr5*, *Itgb2*[33,34]) in ORTHO-A and -M, present in both the vascular and intratissue compartment, to ‘immature’ *Itgam*$^{-}$CD27^{+} NK cells (Immature NK_1 and Immature NK_2) in the tumour, mostly present intratissue, with immature NK_1 significantly enriched in ORTHO-T versus ORTHO-A ($p<0.0001$) and mature NK significantly enriched in ORTHO-A versus ORTHO-T ($p<0.0001$) (Fig. 5A-5B, Supplementary Fig. 11A-11B, Supplementary Data 3). The immature NK subsets displayed common features that distinguished them from Mature NK, including the expression of several chemokine receptors and adhesion molecules (*Ccr2*, *Ccr5*, CD29, CD31), chemokines (*Xcl1*), activation/exhaustion markers (*Tigit*, *Tnfrsf18* (GITR), PD-L1), ribosomal proteins (including *Rplp0*, *Rpl13*, *Rpl32*) and glycolysis-related genes (*Ldha*, *Aldoa*) (Supplementary Fig. 11A).

Interestingly, in subcutaneous MC38 colon carcinoma, a similar shift from a mature CD11b$^+$CD49a$^-$ to a CD11b$^-$CD49a$^+$ state was reported, which was associated with a loss of effector functions[35]. The immature NK_2 cluster, displaying increased *Itga1*/CD49a expression, was predominantly retrieved in the subcutaneous model and showed an enrichment in the CD11b$^-$CD49a$^+$ NK gene signature compared to the Immature NK_1 cluster, which was more prevalent in ORTHO-T (Supplementary Fig. 11C). This could potentially hint to this state being dictated by the organ-specific TME. Moreover, Immature NK_2 also expressed several 'orphan' granzymes (*Gzmc*, *Gzmd*, *Gzme*, *Gzmf*, *Gzmg*), which were not expressed by lung NK cells. On the other hand, the immature NK_2 did not express *Ccl5,* which was restricted to lung NK cells (Supplementary Fig. 11A). These observations were in line with a study from Dean *et al.*[35] showing an altered granzyme expression and loss of CCL5 production upon NK-cell entry into subcutaneous tumours. Notwithstanding their low CD11b$^-$CD49a$^+$ NK score, Immature NK_1 in ORTHO-T also displayed signs of dysfunctionality in their reduced *Prf1* expression and increased expression of inhibitory receptors (Supplementary Fig. 11A). The tumour enrichment of such dysfunctional, immature NK cells was also confirmed via spatial transcriptomics (Fig. 5C, Supplementary Fig. 11D). Murine Mature NK and Immature NK_1 exhibited expression of phenotype-specific genes corresponding respectively to human CD56^{dim}/NK1 (*Cma1*, *Ly6c2*, *Lgals1*, *Gzmb*) and CD56^{bright}/NK2 (*Ctla2a*, *Xcl1*, *Cd7*) NK cells, as identified by Crinier *et al.*[33] (Supplementary Fig. 11A). We also observed an analogous NK-cell heterogeneity in human LUAD sample with NK1 (*FCGR3A*, *FGFBP2*) and NK2 (*CD44*, *NCAM1*, *XCL1*, reduced *PRF1*) clusters being identified along a proliferating NK-cell cluster (Fig. 4A-4C, Supplementary Fig. 9A-9B). Similar to our findings in mice, the NK1 population showed a reduced infiltration into the tumour ($p<0.001$) (Fig. 4C).

T cells encompass both exhausted and effector states in orthotopic tumours

The majority of CD4$^+$ and CD8$^+$ T cells in ORTHO-M and ORTHO-A encompassed a naive-like state (*Sell*$^+$CD62L$^+$*Cd44*$^-$CD44$^-$*Lef1*$^+$*Tcf7*$^+$*Ccr7*$^+$) with a preferential vascular localisation (vascular vs intratissue ORTHO-A: $p = 0.21$-0.35; ORTHO-M: $p<0.0001$) (Fig. 5A-5B, Supplementary Fig. 11A, 11E, Supplementary Data 3). Other T cell states in ORTHO-M/-A were also mostly confined to the vascular space and included CD4$^+$ effector memory T cells (TEM) (*Sell*$^-$CD62L$^-$*Cd44*$^+$CD44$^+$*Lef1*$^-$*Tcf7*$^-$*Ccr7*$^-$), CD8$^+$ TEM (*Sell*$^-$CD62L$^-$CD44$^+$*Lef1*$^-$*Tcf7*$^-$*Ccr7*$^-$*Ccl5*$^+$), and proliferating cells (*Mki67*, *Top2a*) (Fig. 5B, Supplementary Fig. 11A, 11E). Of note, the CD4$^+$ Th1 cells (*Tbx21*, *Ifng*) observed in ORTHO-M were almost exclusively originating from one mouse (HTO2) (Supplementary Fig. 11F), emphasising the benefit of hashing when pooling samples.

Within the ORTHO-T compartment, a shift in activation state was observed, with most T cells adopting effector and exhausted profiles with an intratissue localisation ($p<0.0001$) (Fig. 5B). This increased infiltration of Treg cells (*Foxp3*) ($p<0.05$) and exhausted (CD4$^+$ and CD8$^+$; *Ctla4*, *Pdcd1*/PD-1, *Tigit*, *Lag3*/LAG-3, *Icos*/ICOS) ($p<0.0001$) subsets, was confirmed via spatial transcriptomics (Fig. 5C, Supplementary Fig. 11D) and was in line with patient samples, in which the Treg cells ($p<0.001$) and exhausted CD8$^+$ T cells ($p<0.001$) were also increased in the tumour (Fig. 4A, 4C). In ORTHO-T, a cluster of CD8$^+$ T cells with a central memory state (TCM; Sell/CD62L, CD44, *Lef1*, *Tcf7*, *Ly6c2*/Ly-6C, *Ccl5, Cst7, Cd7, Ahnak, Ctla2a)* and a smaller cluster of CD8$^+$ TEM were identified by SEPARATE-Seq, spatial transcriptomics and flow cytometry (Fig. 5B-5C, Supplementary Fig. 11D-11E, 11G). In contrast, subcutaneous tumours showed an overall poor infiltration of T cells (Fig. 2C, 2E), which mainly encompassed Treg cells and exhausted subsets, with very few effector/activated T cells, such as CD8$^+$ TCM and TEM, being identified (Fig. 5B). We confirmed the highly increased presence of functional, IFNγ-producing CD8$^+$ and CD4$^+$ T cells in ORTHO-T compared to subcutaneous tumours via flow cytometry ($p<0.01$, Supplementary Fig. 11H). Hence, our ORTHO model better recapitulated the patient T cell compartment in terms of number, distribution and also activation state, as patient samples harboured an effector CD8$^+$ T cluster alongside the exhausted cluster (Fig. 4A, 4C).

ILC2s and unconventional T cells are lung-restricted and intratissue

Via SEPARATE-Seq, we also identified an innate lymphoid cell type 2 (ILC2) and an unconventional T cell cluster, which were only present in the lung samples (Fig. 5A-5B, Supplementary Fig. 11A). ILC2s made up a considerable fraction of the cells in ORTHO-M lungs and were found to reside solely intratissue, consistent with their known tissue distribution[36]. In tumour-bearing lungs, ILC2s were reduced in the adjacent tissue compared to ORTHO-M ($p<0.001$) and they remained largely excluded from the tumour itself (Fig. 5B). A mixed ILC2-unconventional T cell population was identified via spatial transcriptomics in VIZ1, which also displayed some tumour infiltration similar to the unconventional T cell cluster identified via SEPARATE-Seq (Fig. 5B-5C). Of note, this cluster was not identified on the VIZ2 region, likely reflecting technical and/or biological variability. In this study, spatial transcriptomics is primarily used as a hypothesis-generating approach rather than for robust statistical testing, given the limited sample size. The unconventional T cell cluster was almost exclusively present intratissue ($p<0.001$) and presented markers of both mucosal-associated invariant T (MAIT) (*Cxcr6*, CD44, *Il18r1*, *Il7r*, *Il23r*) and γδT cells (*Tcrg-C1, Il7r*, *Il23r*) with a type 17 signature (*Il18r1, Ramp1, Tmem176a*)[37,38] (Fig. 5A-5B, Supplementary Fig. 11A). A type 17 signature was also observed in patient samples in the Th17 cluster, present in both adjacent and tumour tissue (Fig. 4A-4C, Supplementary Fig. 9A-9B).

Plasma cells are enriched in the tumour compartment of mice and LUAD patients

Subcutaneous B cells resided intratissue ($p<0.001$) and were very scarce compared to the vast population in LUAD tumours (Fig. 4A, 4C, 6A-6C). More B cells were present in ORTHO-T ($p<0.0001$), where they divided equally over the tissue and vasculature compartments (Fig. 6A-6C). A relative increased tissue infiltration was observed in ORTHO-T compared to ORTHO-A and -M, where in the two latter the majority of naive B cells remained vascular ($p<0.0001$) (Fig. 6A-6C). Most B cells in subcutaneous tumours and ORTHO-T adopted a specific *Junb*$^+$*Ccr7*$^+$ phenotype, mostly absent in ORTHO-A and -M (Fig. 6A-6C, Supplementary Fig. 12A). Alongside *Junb*, these cells also showed increased *Fos*, *Btg1*, *Klf2*, and *Ubb* (Ubiquitin) expression, each of which have been linked to B-cell receptor (BCR) stimulation and/or negative regulation of B-cell proliferation[39–44]. Additionally, increased ICAM-1/CD54 was observed on these tumour-infiltrating cells, which was shown to be important for B-T interactions[45,46] (Supplementary Fig. 12A). A *Lars2*-expressing B-cell population (*Lars2*, *S100a8*, *S100a9, Cmss1*) was identified, predominantly present in ORTHO-A ($p<0.0001$) (Fig. 6A-6C, Supplementary Fig. 12A). We could also identify B1 cells (*Mzb1*, *Plac8*, *Ass1*, CD5, and absence of *Fcer2a*)[47] in all lung-derived samples as well as vascular-restricted transitional B cells (*Vpreb3*, *Iglc1*) in ORTHO-A and -M (Fig. 6A-6C, Supplementary Fig. 12A).

Patient samples showed a clear overall B-cell increase in the tumour as compared to the adjacent tissue ($p<0.001$) (Fig. 1D, 4A, 4C). Notwithstanding the larger B-cell fraction compared to the subcutaneous model, this tumour-specific B-cell enrichment was not observed in our ORTHO model, showing its limitations (Fig. 2C, 2E, 4A, 4C). Plasma cells (*Jchain*, *Sdc1*/CD138) were almost absent in our SEPARATE-Seq dataset (generated from sorted CD45$^+$ cells), likely due to their loss of CD45 (low *Ptprc* and CD45R/B220) (Fig. 6A-6C, Supplementary Fig. 12A). However, we could clearly identify them via spatial transcriptomics. Plasma cells preferentially infiltrated the tumour (Fig. 6C, Supplementary Fig. 12B) and this tumour-specific enrichment of plasma cells was also observed in LUAD patients ($p<0.001$) (Fig. 1D, 4A, 4C). While the majority of murine models do not harbour tertiary lymphoid structures (TLS), interestingly, lymphoid aggregates of T and/or B cells could be observed in the tumour periphery of our ORTHO model, covering varying degrees of organisation (defined T- and B-cell zones) and sizes (Fig. 6D, Supplementary Fig. 12C-12E).

Overall, ORTHO-T harboured significantly more B cells than subcutaneous tumours ($p<0.0001$) and even showed plasma cell presence. In this aspect, our model better mirrors the patient situation, although it does not entirely recapitulate the human B-cell landscape.

Tumour-infiltrating cDCs adopt a mature or ISG phenotype

Within the dendritic cell (DC) compartment, our SEPARATE-Seq dataset identified plasmacytoid DCs (pDCs), DC3s and distinct clusters of conventional DCs (cDCs) (Fig. 7A-7B, Supplementary Fig. 12F). Subcutaneous tumours harboured similar DC subsets as ORTHO-T, though with lower abundance ($p<0.001$) (Fig. 7B). The majority of DCs resided intratissue irrespective of the sample origin ($p<0.001$), with pDCs and *Mgl2*$^-$*Cd209a*$^+$*Il1r2*$^-$ cDC2s being the main vascular cells in respectively ORTHO-M and -A (Fig. 7B).

pDCs were enriched in ORTHO-T compared to ORTHO-A ($p<0.001$), as confirmed via spatial transcriptomics, and resided intratissue (Fig. 2E, 7B-7C). No such clear increase was seen in the human dataset (Fig. 1D, 4B, 4C), though this has been reported in several studies[4,48].

The rather homogeneous cDC1 cluster (*Xcr1*/XCR1, *Clec9a*) appeared to give rise to an intermediate state of maturing *Ccl17*$^+$ cDC1s (*Xcr1*/XCR1, *Clec9a*, *Ccl17*) and to *Ccl17*$^+$ mature DCs (*Ccr7, Ccl17*) (Fig. 7A, Supplementary Fig. 12F). These all poorly infiltrated the TME and preferentially resided in ORTHO-A and -M, which was confirmed spatially (Fig. 7B-7C). Within ORTHO-T, cDC1s displayed a high expression of interferon- (IFN-) stimulated genes (ISGs) (*Ifitm1/2/3/6, Ifi205*), IFN mediators (*Stat1*, *Stat2*, *Irf9*) and *Plet1* (Fig. 7B, Supplementary Fig. 12F). *Plet1* has been associated with enhanced DC motility in extracellular matrix[49], hinting to their enhanced ability to infiltrate tumours.

In contrast to cDC1s, cDC2s (*Itgam*, *Sirpa*) were more heterogeneous (Fig. 7A, Supplementary Fig. 12F). Three major cDC2 subsets could be distinguished based on *Mgl2 (*CD301b), *Cd209a* (DC-SIGN) and *Il1r2* expression (Fig. 7A, Supplementary Fig. 12F). SEPARATE-Seq and spatial transcriptomics showed that the majority of cDC2s infiltrating tumours (ORTHO-T and SUBCUT) adopted an *Mgl2*$^+$*Cd209a*$^-$*Il1r2*$^+$ or, to a lesser extent, an *Mgl2*$^-$*Cd209a*$^+$*Il1r2*$^-$ phenotype, whereas *Mgl2*$^+$*Cd209a*$^+$*Il1r2*$^-$ cDC2s were restricted to ORTHO-M and -A (Fig. 7B-7C, Supplementary Fig. 12F). Similar as for cDC1s, an ISG cDC2 subset was identified and was enriched in ORTHO-T ($p<0.05$), which could also be confirmed in the spatial transcriptomic dataset (Fig. 7B-7C). ISG cDC2s exhibited an even more pronounced ISG signature than cDC1s and were characterised by *Rsad2*, *Cxcl10* and *Oasl2* expression (along with *Ifitm1/2/3/6, Ifi205*, *Stat1*, *Stat2*, *Irf9*) (Supplementary Fig. 12F). Furthermore, we identified a cluster of maturing cDC2s (*Itgam*, *Sirpa*, *Ccr7*), which was also enriched in ORTHO-T ($p<0.05$), as confirmed via spatial transcriptomics (Fig. 7A-7C, Supplementary Fig. 12F). Overall, cDC2s made up the bulk of DCs in ORTHO-T and were significantly enriched compared to ORTHO-A ($p<0.0001$), which was also the case in the human dataset ($p<0.001$) (Fig. 1D, 4B-4C, 7B).

Interestingly, *Ccl17*$^-$ mature DCs, expressing the highest levels of *Ccr7*, were restricted to the TME (ORTHO-T and SUBCUT) and exhibited an upregulation of immunoregulatory and activation markers (*Cd200*/CD200, *Cd274*/CD274 (PD-L1), *Pdcd1lg2*/CD273 (PD-L2), Cd80/CD80, *Cd86*, *Cd83*, CD40) (Fig. 7B, Supplementary Fig. 12F). Spatially, mature DCs (*Ccl17* being non-targetable) were also enriched in tumour tissue (Fig. 7C), which was also observed in patients (Fig. 4B-4C).

Altogether, SUBCUT and ORTHO tumours largely harboured the same DC subsets, yet the overall DC population was greatly expanded in ORTHO-T, better reflecting reported DC numbers in patients (Fig. 7B, 4C). In tumours, cDCs mostly acquired a mature or ISG phenotype and differed greatly from those found in ORTHO-A and -M.

Tumour presence is accompanied by increased tissue infiltration of neutrophils, along with a hypoxic signature

We investigated whether other cell types, besides cDCs, exhibited an ISG signature and observed this phenotype in neutrophils and macrophages as well (Fig. 2B, 7D). Upon neutrophil subclustering, we identified ISG neutrophils (*Rsad2*, *Usp18*, *Ifit1*) with an increased intratissue tumour presence ($p<0.0001$) (Fig. 7E-7F, Supplementary Fig. 12G). In the orthotopic setting, these neutrophils mainly localised in the outer region of the tumour (Fig. 7G). Though neutrophil numbers in the human NSCLC dataset are limited due to their difficult capture via scRNA-Seq, we could observe an *Rsad2*$^{+}$*Ifit1*$^{+}$ ISG neutrophil phenotype in patients in both adjacent and tumour tissue (Supplementary Fig. 13A).

Neutrophils in NSCLC patients were previously shown to adopt either a 'normal adjacent tissue-associated' neutrophil (NAN) or a 'tumour-associated' neutrophil (TAN) phenotype with more aging/chronic activation/exhaustion features[14]. In LUAD patient samples, *SELL*$^{+}$ neutrophils (NAN phenotype) and *SELL*$^{-}$ neutrophils (TAN phenotype) showed an enrichment in adjacent tissue ($p<0.001$) and tumour tissue ($p=0.12$) respectively (Fig. 4B-4C). Interestingly, we observed a similar dichotomy in murine ORTHO-A and -T neutrophils. As such, CD62L^{+} Neutro_2 formed the majority of neutrophils in ORTHO-A and expressed high levels of *Sell/*CD62L, *Cxcr2*/CD182, *Csf3r*, *Rasgrp4* and *Msrb1*, reminiscent of the human NANs[14], along with high expression of several granule-associated genes (*Lrg1*, *Mmp9*, *Hp* and *Pglyrp1*) (Fig. 7E-7F, Supplementary Fig. 12G). These ORTHO-A neutrophils adopted a phenotype similar to the ORTHO-M neutrophils (CD62L^{+} Neutro_1), yet were characterised by a higher expression of *Wfdc17*, *Lrg1*, *Tspo* and *Ifitm1* (Supplementary Fig. 12G). Within the adjacent tissue, spatially identified neutrophils displayed a *Lrg1*$^{+}$*Cd14*$^{-}$ phenotype, largely consistent with the CD62L^{+} Neutro_2 cluster, but with only a fraction expressing *Cxcr2* (*Lrg1*$^{+}$*Cd14*$^{-}$*Cxcr2*$^{+}$) (Fig. 7G, Supplementary Fig. 8, Supplementary Table 4).

Interestingly, we observed a substantial increase in overall neutrophil numbers in ORTHO-A/-T compared to ORTHO-M ($p<0.0001$) (Fig. 7F), consistent with neutrophilia observed in various human and murine cancer types, often associated with cancer stage[50–54]. This emergency granulopoiesis hypothesis was further supported by the almost exclusive presence of immature neutrophils (*Mmp8*, *Camp*, *Ltf*, *Ngp*) in tumour-bearing mice (Fig. 5E-5F, Supplementary Fig. 9A). While more than half of the neutrophils in ORTHO-A and ORTHO-M resided in the vasculature, this fraction was greatly reduced in ORTHO-T, supporting an increased tissue infiltration in the tumour ($p<0.001$) (Fig. 5E-5F). In the vasculature, the ORTHO-T neutrophils retained a CD62L^{+} phenotype, whereas upon tissue entry, they adopted a distinct 'TAN-like' phenotype (*Tnf*$^{+}$*Hdc*$^{+}$ and *Tnf*$^{+}$*Fnip2*$^{+}$) (Fig. 7E-7F, Supplementary Fig. 12G). This phenotype was characterised by a high levels of inflammation/activation-related markers (CD11b, PD-L1/CD274, CD39, CD73, CD14, *Ier3*, *Basp1*, *Fth1*) and, consistent with the phenotype seen in human TANs[14], displaying a higher expression of ICAM-1/CD54, CD83, *Ccrl2*, *Ccl3* and *Cxcl2*[14] (Supplementary Fig. 12G). Interestingly, the *Tnf*$^{+}$ neutrophils in ORTHO-T also displayed increased expression of SiglecF/CD170 and the anti-apoptotic *Bcl2l1* and *Bcl2a1b* (Supplementary Fig. 12G), consistent with the pro-tumoural, long-lived neutrophils observed in injectable and genetic KP mouse models[55,56]. Moreover, hypoxic neutrophil clusters were observed in both tumour models (Hypoxic *Hdc*$^{+}$, Hypoxic *Fnip2*$^{+}$ and subcutaneous-specific Hypoxic *Ltb4r1*$^{+}$ neutrophils*)* and presented a similar increase in several TAN markers[14] (*Cxcl2*, *Ccl3, Vegfa*, *Hif1a)* along with the aforementioned inflammation/activation-related markers and other hypoxia-related genes (*Mif*, *Slc2a1*, *Bnip3*, *Hilpda*, *Egln3*, *Ndrg1*) (Fig. 7E-7F, Supplementary Fig. 12G), pointing to a non-organ-specific, tumour-driven signature. In ORTHO-T, hypoxic *Cxcl2*$^{-}$ neutrophils were found in the tumour core, whereas the other tumour-infiltrating clusters (*Tnf*$^{+}$ and Hypoxic *Cxcl2*$^{+}$) were observed along the tumour edge (Fig. 7G).

Notably, subcutaneous tumours contained a CD62L^{-}*Pglyrp1*$^{+}$ neutrophil cluster, which could represent recently infiltrated neutrophils, given their resemblance with the CD62L^{+} Neutro_2 cluster in ORTHO-A/-T (*Pglyrp1*, *Wfdc17*, *Lrg1*, *Tspo*, *Ifitm1*) (Fig. 7E-7F, Supplementary Fig. 12G). Indeed, reduced *Pglyrp1* expression has been correlated with neutrophil maturity, hence its loss in the other tumour-specific intratissue clusters (Supplementary Fig. 12G) points to aged neutrophils and prolonged tissue-residency[57].

Overall, the majority of tumour-infiltrating neutrophils adopted a tumour-specific signature, regardless of the tissue. However, the NAN-TAN dichotomy, as observed in patients, was solely observed in the ORTHO setting.

ORTHO-T-specific Lipid TAMs form a ring along the tumour edge

The main resident lung macrophage population, namely the alveolar macrophages (AMs), was largely excluded from the tumour as shown by SEPARATE-Seq ($p<0.0001$) and spatial transcriptomics, in agreement with their significant reduction in patient tumours ($p<0.001$) (Fig. 1D, 2C, 2E, 8A-8B, Supplementary Fig. 13B-13C). Subclustering of the other monocyte and macrophage subsets, confirmed that, apart from AMs, interstitial macrophages (IMs) constituted a major intratissue, resident lung macrophage subset that was confined to ORTHO-M and -A, which was confirmed via spatial transcriptomics (Fig. 8B-8E). However, we identified an ORTHO-T-restricted *Ltc4s*$^{+}$ tumour-associated macrophage (TAM) cluster, sharing a gene signature similar to previously reported Lyve1^{high}MHCII^{low} IMs[58] (*Fcna*, *Prg4*, *Cd4b*, *Ednrb*, *Ltc4s*, *Ccl24*, *Icam2*, *Serpinb2/6a*, *Marco*, *Cd38*/CD38, *Padi4*, and low MHCII-related genes and *Cx3cr1*; no detected *Lyve1* via scRNA-Seq consistent with Chakarov *et al.*[58]) and reminiscent of *Ltc4s*^{high}*Fn1*^{high} resident macrophages in the infarcted heart (*Ltc4s*, *Fn1*, TIM-4, *Msr1*, *Saa3*, *Arg1*, *Sdc3*, *Slpi*, *C4b*, *Ecm1*, *Ccl6*, and low *Ccr2*)[59] (Fig. 8D-8F, Supplementary Fig. 13E). Hence, we hypothesised that *Ltc4s*$^{+}$ TAMs could arise from 'healthy' Lyve1^{high}MHCII^{low} IMs. Of note, at present, only a few studies conflictingly identified human IM-resembling cells at the transcriptomics level, without flow cytometric identity confirmation[60–62], preventing us from confidently identifying these cells in our human dataset. Though IMs were shown to contribute to the pool of TAMs in intravenously injected lung tumour-bearing mice, the majority of TAMs were of monocytic origin[63]. As expected, classical and non-classical monocytes were mainly present in the lung vasculature and were overall reduced in ORTHO-T compared to ORTHO-A, in line with spatial transcriptomics and consistent with the reduced presence of *CD14*$^+$ and *CD16*$^+$ monocytes, respectively, in patient tumours (Fig. 8C-8D, 4B-4C, Supplementary Fig. 13D, 13G). In subcutaneous tumours, monocytes likely differentiated rapidly upon tissue/tumour entry into TAMs. Therefore, we further referred to them as immature TAMs (Fig. 8C-8D). However, within subcutaneous tumours and ORTHO-T, we did observe distinct neutrophil-like monocyte (NeuMono) clusters (Fig. 8C-8D, Supplementary Fig. 13D), which were recently shown to expand under various inflammatory conditions (emergency myelopoiesis) in mice and humans[64–69].

When subclustering the TAMs from subcutaneous tumours and ORTHO-T separately, comparable intratissue macrophage phenotypes were identified, including immature (*Chil3*, *Plac8*), hypoxic (*Slc2a1*, *Bnip3*, *Hilpda*, *Vegfa, Egln3*, *Ndrg1*), MHCII$^+$ (MHC class II genes and protein), *Folr2*$^+$*C1q*$^+$ (*Folr2*, *C1qa*/*b*/*c, Mrc1*) and ISG (*Isg15*, *Rsad2*) TAM subsets (Fig. 8E-8F, Supplementary Fig. 13E-13F). Importantly, Lipid TAMs (*Gpnmb*, *Syngr1*, *Lipa*, *Cstb*, *Ctsd*, *Fth1*, *Psap*), which have previously been identified in orthotopic murine and human tumours[60,70–76], formed the main ORTHO-T TAM population, and were entirely missing in subcutaneous tumours (Fig. 8C-8F, Supplementary Fig. 13D-13F). Lipid TAMs (*Spp1*, *F7*, *Cd63*, *Cd9, Ctsb*, *Cd68*, *Lgals3*) consisted of three subpopulations, with Lipid TAM_1 (*Pf4*, *Plp2*, *Arg1*, *Vcan*) as a more intermediate state, and Lipid TAM_2 (*Gpnmb*, *Syngr1*, *Lipa*, *Pf4*, *Slc48a1*, *Hmox1*, *Arg1*) and Lipid TAM_3 (*Gpnmb*, *Syngr1*, *Lipa*, *Plaur*, *Gpr137b*, *Gdf15*) displaying the most pronounced lipid-associated phenotype[72,77] (Fig. 8E, Supplementary Fig. 13E). In the human dataset, *SPP1*$^+$*FBP1*$^+$ and *FOLR2*$^+$*PLTP*$^+$ macrophages exhibited a clear lipid-associated signature and were also significantly enriched in the tumour (Fig. 4B-4C, Supplementary Fig. 9C). Of note, AMs, which naturally clear lipids under homeostasis[78], also exhibited this signature in patients (Supplementary Fig. 9C). In mice, we identified a small, distinct Lipid AM population, which preferentially resided in ORTHO-T (Fig. 8A, Supplementary Fig. 13B-13C). Remarkably, we found that the Lipid TAMs formed a ring-like structure along the tumour edge, which was already apparent in smaller nodules (T4) (Fig. 8B, S13G). Deeper in the tumour core, hypoxic TAMs were surrounding *Folr2*$^+$*C1q*$^+$ TAMs (Fig. 8B, Supplementary Fig. 13G). The latter resembled the murine/human evolutionarily conserved *FOLR2*$^+$ TAMs (*Mrc1/MRC1*, *Maf/MAF*, *C1qa/C1QA*) observed in breast cancer, apart from their lack of *Lyve1* expression[79] (Supplementary Fig. 13E). We identified two similar *LYVE1*$^-$*FOLR2*$^+$ populations in LUAD patients, namely the lipid-associated *FOLR2*$^+$*PLTP*$^+$ and *FOLR2*$^+$*PLTP*$^-$ macrophages (Fig. 4B-4C, Supplementary Fig. 9C). In contradiction with the breast cancer FOLR2$^+$ macrophages, which were enriched in the breast adjacent tissue[79], the *FOLR2*$^+$*PLTP*$^+$ population was significantly expanded in LUAD tumours ($p<0.001$) (Fig. 4C). No hypoxic TAM cluster could be identified in LUAD patients, though hypoxic markers (*NDRG1*, *BNIP3*, *ERO1A*, *HK2*, *LDHA*, *MIF*) were upregulated in heat-shock protein (HSP)-enriched *HSP*$^+$ and lipid *SPP1*$^+$*FBP1*$^+$ TAMs (Supplementary Fig. 9C).

In orthotopic samples, immature macrophages and MHCII$^+$ TAMs were dispersed throughout the tumour, with the latter more densely populating smaller tumour nodules (nodule T4 in Fig. 3A) (Fig. 8B, S13G). The human MHCII$^+$ counterpart was identified as the *SPP1*$^+$*C3*$^+$ cluster, using the 'antigen-presenting macrophage' phenotype proposed by Guimarães *et al.*[60], and was also confined to the tumour (Fig. 4B-4C, Supplementary Fig. 9C). Similar to neutrophils and DCs, an ISG signature was found in the TAMs of both subcutaneous tumours and ORTHO-T (Fig. 8D-8F, Supplementary Fig. 13D-13F). ISG TAMs (*ISG15*, *CXCL9/10*, *GBP1*, *STAT1*) were also observed in human patients (Fig. 4B-4C).

Overall, the well-known macrophage plasticity led to the presence of different comparable intratissue TAM phenotypes in subcutaneous tumours and ORTHO-T; several of which had distinct human counterparts. Importantly, the majority of human TAMs displayed a clear lipid signature and Lipid TAMs were solely identified in ORTHO, where they specifically formed a ring around the tumour edge.

Spatial transcriptomics reveals Lipid-TAM- and ISG-niches in lung tumours

The distinct spatial organisation of TAM states prompted us to investigate whether specific cellular niches/neighbourhoods could be distinguished in our ORTHO model. To identify these niches in an automated, unbiased fashion, we used the Monkeybread package[80], incorporating both immune and non-immune cells in the analysis. Eleven different spatial neighbourhoods were identified, named Niche_1 to Niche_11 (Fig. 9A, Supplementary Data 4). Niche_1, Niche_2 and Niche_3, located in the adjacent tissue, primarily comprised *Hif1a*$^-$ endothelial cells, AT2 cells, SMCs and B cells (Fig. 9A-9C), with Niche_1 covering the largest area, while Niche_2 and Niche_3 appeared as distinct hubs. Niche_2 and Niche_3 were driven by the specific presence of *Lrg1*$^+$*Cd14*$^-$*Cxcr2*$^+$ and ISG neutrophils in Niche_2 and *Mgl2*$^-$*Cd209a*$^+$*Il1r2*$^-$ cDC2s in Niche_3. Ciliated cells, SMCs and IMs defined Niche_4, clearly lining the airways in the adjacent tissue. Some ciliated cells were also observed within the tumour core, in Niche_10 (Fig. 9A-9C, Supplementary Fig. 7B), pointing to the probable entry point of the inoculated cancer cells. Niche_5 was located close to the airways and was mainly composed of *Plau*^{low} fibroblasts (Fig. 9A-9C). Additionally, it was enriched in MHCII$^+$ and *Folr2*$^+$*C1q*$^+$ TAMs, and Treg cells. Niche_6 and Niche_7 located at the tumour edge and showed the highest immune infiltration. Niche_6 lined the tumour edge at the tumour/adjacent tissue interface, with the Lipid-TAMs specifically defining this neighbourhood. Interestingly, Niche_7 formed distinct ISG-enriched hubs, most notably enriched by ISG cDC2s, but also comprising ISG CAFs and ISG TAMs. Niche_8 outlined the space between the tumour core and its edge and resembled the composition of ISG hubs, except for the absence of cDC1 and ISG cDC2 clusters and the increased presence of hypoxic *Cxcl2*$^-$ neutrophils and *Ptgs2*$^+$ fibroblasts. Niche_9 and Niche_10 made up the tumour core, characterised by minimal immune and abundant fibroblast infiltration (*Lrrc15*$^+$ and proliferating), with the presence of *Folr2*$^+$*C1q*$^+$ TAMs or ciliated cells and hypoxic *Cxcl2*$^-$ neutrophils driving the respective niches. Around and within the tumour core, immune cells were mainly concentrated in Niche_11; hubs which specifically harboured maturing cDC2s and mature DCs, as well as fibroblasts (*Ptgs2*$^+$, proliferating and ISG), and immature and hypoxic TAMs (Fig. 9A-9C). The specific maturing/mature DC enrichment in these hubs suggests local, intratumoural DC maturation and resembles the CCR7$^+$ DC clusters observed in several murine and human cancers[81,82].

The shared ISG phenotype of the Niche_7 cell types (fibroblasts, DCs, macrophages and neutrophils) and the previous identification of such a signature via SEPARATE-Seq (Fig. 7D) prompted further investigation. Individual ISG localisation (*Rsad2, Ifit3, Ifit1, Cxcl10, Oasl2 and Oas3)* clearly placed these genes at the tumour edge, forming discrete hubs (Fig. 9D, Supplementary Fig. 14A). Wondering whether these ISG hubs were model-/mouse-specific, we queried publicly available spatial transcriptomics data (Xenium) and confirmed a similar ISG spatial distribution in a NSCLC patient sample along the tumour edge, which was analogously restricted to the tumour area (Fig. 9E). Moreover, we confirmed the tumour-specific enrichment of this ISG signature in LUAD patients (Fig. 9F).

Overall, we identified distinct spatial niches in our ORTHO model, including an intratumoural ring-like Lipid TAM niche. Interestingly, we also observed specific sites of ISG cell-enrichment and confirmed the tumour-specific enhanced ISG signature and presence of such ISG hubs in NSCLC patients.

Combined chemotherapy and immune checkpoint blockade therapy elicits responses in ORTHO but not SUBCUT tumours

To evaluate the translational relevance of the ORTHO model relative to the SUBCUT model, we conducted therapeutic experiments using a clinically inspired regimen combining immune checkpoint blockade with platinum-based chemotherapy, reflecting standard-of-care for NSCLC[83]. Mice received multiple cycles of anti-PD-1 (αPD-1) and cisplatin (Fig. 10A), with the first two doses of αPD-1 administered during the early active phase (zeitgeber time 13) to optimise therapeutic efficacy, in line with recent evidence highlighting the importance of dosing timing[84].

In the ORTHO model, both chemotherapy alone and combination therapy conferred a significant survival benefit (Fig. 10B). While the combination therapy did not reach statistical significance over chemotherapy alone, a clear trend toward improved response was observed (Cis vs Combo, $p=0.08$), mirroring clinical observations in advanced NSCLC patients[85,86]. In contrast, the SUBCUT model showed no significant survival benefit under the same regimen (Fig. 10C), highlighting the superior translational relevance of the ORTHO model for pre-clinical evaluation of novel therapeutic strategies.

Analysis of early immune changes after a single therapy cycle in the ORTHO model revealed no major shifts in the overall distribution of main immune populations (Supplementary Fig. 14B), except for the expected cisplatin-induced decrease in AMs[87]. Within the T cell compartment, combination therapy induced a significant expansion of anti-tumour $CD44^+CD62L^-$ effector $CD8^+$ T cells ($p<0.0001$) and granzyme B^+ cytotoxic $CD8^+$ T cells ($p<0.05$) (Supplementary Fig. 14C-D), potentially underlying the enhanced survival benefit. Notably, $CD39^+$ $CD8^+$ T cells ($p<0.05$), linked to tumour reactivity and therapy responsiveness[88], and $Tim3^+$ $CD8^+$ T cells ($p<0.05$), indicative of chronic activation/exhaustion, were also increased, reflecting a therapy-driven immune activation.

Collectively, these findings demonstrate the translational relevance of the ORTHO model, with combination therapy significantly extending survival while producing incomplete responses, thereby mirroring the limited clinical benefit of current standard-of-care treatments in NSCLC and highlighting the model's value for testing novel immunotherapy strategies.

DISCUSSION

The cancer treatment landscape has dramatically been transformed through the incorporation of immunotherapy. However, recent failures in immuno-oncology trials prompt the question as to where issues arise in the research pipeline and how they can be addressed. Among the critical challenges identified is the need for preclinical models that accurately mimic human tumours[89,90]. Subcutaneous cancer models are widely used despite their limitations in replicating key aspects of the human disease, likely due to their ease of tumour establishment and growth monitoring. Here, we presented an injectable, orthotopic, LLC-derived pre-clinical lung cancer model (ORTHO) that provides a plethora of advantages to the currently used models: (1) predictable growth and reproducibility, (2) overall high technical feasibility, allowing the quick implementation in any laboratory equipped with an inhalation anaesthetic setup, (3) limited hands-on time (approximately 1.5 minutes per mouse after anaesthetic induction), (4) Thy1.1 expression allows for easy cancer cell identification via flow cytometry, enabling the detection of a low number of cancer cells and their quantification, (5) working with an injectable model allows researchers the flexibility to modify the cell line or to use genetically altered mouse strain, and (6) adjacent non-tumoural tissue can be easily dissected from tumour nodules, enabling the immune characterisation of both compartments individually, similar to patient samples. The ORTHO model is compatible with both sexes, with a trend toward higher neutrophil infiltration in males, consistent with reported sex-biased neutrophil responses in other cancer models[91,92]. While the ORTHO model recapitulates key features of human LUAD, including the suboptimal response to standard NSCLC therapies, some differences in immune cell composition remain. These likely stem from limitations of human scRNA-seq for quantitative comparisons, interpatient variability in relatively small cohorts, and the presence of circulating immune cells in non-perfused patient samples[93], which can artificially inflate the apparent abundance of T cells and other easily captured populations.

Moreover, we established SEPARATE-Seq; a widely applicable technique that enables the compartmentalisation of (immune) cells into vascular and genuine intratissue cells in parallel with scRNA-/CITE-Seq. While the intravenous injection of fluorescently labelled antibodies (CD45 or cell-specific markers) has proven its usefulness to distinguish vascular/marginated and extravascular/intratissue cells of the lung, heart, liver and other organs[24,94–98], its use has not yet been integrated in scRNA-Seq-based studies. Previous studies employing scRNA-Seq either relied on intravenous labelling, followed by vascular/intratissue cell sorting[96,97] or performed a full organ *versus* blood comparison[59]. SEPARATE-Seq avoids these cumbersome and costly experiments and reduces the number of animals needed, as it can simultaneously be used with flow cytometry. Moreover, building on the same biotin-STREP usage, SEPARATE-Seq could allow for the addition of a personalised CITE-Seq marker by combining a biotinylated antibody of interest with a STREP-tag.

Putting SEPARATE-Seq into practice, we show that the majority of vascular immune cells are neutrophils in our ORTHO model, and that these display a distinct phenotype (NAN-like) compared to the intratissue, tumour-infiltrating neutrophils (TAN-like). Recently, several studies described the tumour-driven reprogramming of neutrophils across different cancer types in both mice and humans[14,99–101], matching the reprogramming we observe to a TAN-like phenotype. Moreover, Ng *et al.* investigated distinct neutrophil states in the bone marrow, blood, spleen and tumours of an orthotopic pancreatic cancer model and described a tumour-infiltrating, pro-tumoural hypoxic neutrophil subset, that, similar to our hypoxic subsets, showed an infiltration deep into the tumour core[99]. Ng *et al.* also mapped the neutrophils from the intravenous KP1.9 lung cancer dataset of Zilionis *et al.*[69] to their reference UMAP and detected KP neutrophils across both tumour and peripheral neutrophil states[99]. The peripheral-matched KP neutrophils most likely match our adjacent-enriched CD62L$^+$ neutrophils, suggesting that the neutrophils defined in Zilionis *et al.* contained both tumour and adjacent neutrophils. This highlights the importance of adjacent and tumour tissue separation prior to cell identification, as such limiting the contamination of adjacent cells in tumour-focussed analyses (and *vice versa*) and thus allowing for the robust identification of mouse-human conserved subsets. Regrettably, intravenously established cancer models complicate such a separation due to the formation of numerous small tumour nodules throughout the lung tissue.

The differentiation of monocytes into TAMs upon tumour entry has been extensively described, along with their inherent plasticity, as such giving rise to a wide variety of TAM subsets[69,102–105]. We show that our ORTHO model harbours distinct TAM states, several of these holding conserved counterparts in LUAD patients, including the lipid-associated TAMs, which are absent in subcutaneous tumours. Lipid-associated macrophages have only recently gained attention in different cancer types[71–76,106–109]. However, they have been well described in atherosclerosis[110], where they are often referred to as foam cells. We showed that these cells formed a ring-like structure along the ORTHO-T edge, akin to the immunosuppressive foam-cell (FC) wall observed in colorectal cancer (CRC) patients[74]. In CRC, a higher abundance of lipid-associated TAMs/FCs (FC^{high}) was associated with worse disease outcome, reduced activated CD8$^+$ T cells, and an enrichment of exhausted T cells and Treg cells compared to FC^{low} patients. Similarly, we observe a high infiltration of Treg cells and exhausted T cells in ORTHO-T, alongside the presence of a functional IFNγ-producing CD8$^+$ T cell state. In the future, lipid TAM-specific depletion could validate similar Lipid TAM^{high} *versus* Lipid TAM^{low}-driven remodulation of the TME in mice.

We also observed tumour-driven rewiring of various other cell types, including T cells, NK cells and DCs. Whereas T cell rewiring has been extensively studied and forms the foundation of the earliest immunotherapies[111–113], insights into tumour-driven NK-cell phenotypes have only emerged recently. In our ORTHO model, NK cells were primarily driven to an ‘immature’ dysfunctional state, consistent with the rapid loss of effector functions observed when circulating NK cells enter the TME[35]. The exact mechanism underlying this dysfunction remains unclear, though PGE_2 and TGFβ were reported to be involved[35]. In a murine lymphoma model, NK dysfunctionality was more progressive and induced by tumour recognition[114]. However, NK dysfunction was proven to be reversible, with a return to reactivity either by removal from the highly stimulatory environment or by IL-15/IL-15RA treatment[35,114]. Our ORTHO model provides a valuable tool to further investigate the drivers of this dysfunction and evaluate therapies targeting its reversal or inhibition. Additionally, it allows to investigate whether non-marginated NK cells already display a certain degree of dysfunction, as observed in breast and lung cancer patients[115,116].

DCs are crucial in mounting durable anti-tumour responses, exemplified by the various DC-based/-focussed cancer therapies currently under investigation[117–119]. However, tumour-driven phenotypic changes can hamper DC functionality on different levels, including altered antigen uptake and presentation, reduced tumour infiltration and, non-responsiveness to stimulation[120–124]. In our ORTHO model, both cDC1s and cDC2s underwent phenotypic shifts upon tumour entry, with intratumoural cDCs adopting a mature state, while subsets could adopt an ISG state. The ISG cDC2s resembled inflammatory cDC2s (inf-cDC2), identified under various inflammatory and infectious conditions[125], and tumour-induced ISG$^+$ DCs[126]. Both were shown to efficiently activate CD8$^+$ T cells, potentiated in the tumour context via MHCI dressing. In breast and head and neck cancer, IFN signalling in cDC1s was shown to be crucial for anti-tumour responses[127,128], suggesting that ISG cDCs are critical anti-tumour mediators and opening new avenues for strategies to enhance the shift of cDCs to an ISG phenotype.

Intriguingly, we observed a similar ISG phenotype in T cells, TAMs, AMs, neutrophils, and fibroblasts, mostly enriched within ORTHO tumours. We identified similar ISG TAMs, T cells and neutrophils in LUAD patients. In a recent pancreatic cancer study, IFNα-induced BST2$^+$ macrophages were linked to poor patient prognosis[129]. These pro-tumoural macrophages arose following ‘mitochondrial DNA damage’-induced cGAS-STING activation and drove CD8$^+$ T cell exhaustion. As such, the ISG *Bst2* was increased in all identified ISG cell types in our model, including the ISG TAMs. Contrastingly, Ly6E^{high} IFN-induced neutrophils were shown to be anti-tumoural, drove cytotoxic CD8$^+$ T cell activation and accumulated following immunotherapy in different human and murine cancer types[130,131]. Additionally, the STAT3–STING–IFN axis was recently shown to control the metastatic spread of small cell lung cancer[132]. Our study to identifies spatially distinct ISG-enriched regions, termed ISG hubs, in a tumour context. Importantly, we observed a similar spatial distribution of ISGs in a NSCLC patient tumour. Similar ISG hubs, termed interferon-induced cell (IFNIC) colonies, have recently been observed in the border zone (separating (non-)injured regions) of murine and human myocardial infarcted hearts[133]. These colonies formed as a result of high mechanical stress, leading to nuclear rupture and loss of DNA compartmentalisation in cardiomyocytes and fibroblasts. This promoted activation of the cGAS–STING–IRF3 DNA-sensing pathway and subsequent production of IFNs, which in turn generated IFNICs. Accumulating evidence points to the importance of high mechanical, compressive stress in tumours[134] and could potentially explain the presence of ISG hubs at the border regions of tumours. The clinical relevance of the observed ISG hubs and the potentially contrasting pro- and anti-tumoural functions of the cells therein, warrants further research and could provide insights into the use of IFN-based therapies.

Overall, we introduce the SEPARATE-Seq technique, which can be used throughout the whole (immuno-)biological field for the identification of cellular compartments (vascular *versus* intratissue). Most importantly, our resource provides a platform for further preclinical NSCLC research via our ORTHO model and its thorough immune characterisation via SEPARATE-Seq (interactive tool: single-cell.be/Laouimmunology/SEPARATESeq), and its demonstrated responsiveness to combination therapy, displaying strong similarities in terms of cell types and their location within human LUAD tumours.

METHODS

Specifics regarding materials and reagents used in this study are listed in Supplementary Table 5.

All procedures followed the guidelines of the Belgian Council for Laboratory Animal Science (BCLAS), based on policies of the Federation of European Laboratory Animal Science Associations (FELASA). All experiments were approved by the Institutional Animal Care and Use Committee (IACUC) of the Vrije Universiteit Brussel (Ethische Commissie voor Dierproeven (ECD), LA 1210220; licenses 20-220-23, 20-220-27, 21-220-04, 21-220-05, 22-220-10, 23-220-07, 23-220-23, 23-220-42, 25-220-24, 25-220-28, 25-220-34 and 25-220-38) and by the IACUC of the University of Liege (license 20-2267).

Mouse strains

6-8 weeks old C57BL/6 mice were purchased from Janvier Labs. Unless otherwise specified, mice were female. All mice were group housed in the animal facility of the Brussels Center for Immunology (BCIM) laboratory (Vrije Universiteit Brussel, Elsene, Belgium) under standard conditions, notably 12-hour light/dark cycle, temperature of 20-24°C, relative humidity of 45-65%, access to environmental enrichment, ad libitum food and water and daily health checks. Mice were weighed every two to three days. Euthanasia was performed according to approved IACUC-protocols once the endpoint criteria were met. $Kras^{G12D/+}$;$Trp53^{lox/lox}$ (KP) mice were obtained from Dr. Pierre Close (GIGA-Institute, University of Liège, BE). All mice were housed and bred in institutional specific pathogen-free facilities, maintained in a 12-hour light-dark cycle and had access to ad libitum food and water. Both male and female mice (10-weeks old) were used in similar proportions for Cre recombination. Genetic recombination was induced following intratracheal administration of Cre-containing Adeno-Associated Viruses (AAV6.2ff Spb-Cre). Mice were sacrificed at ethical endpoint (90-120 days post AAV delivery).

Cell lines

Lewis Lung Carcinoma (LLC)-Thy1.1 P0 (kind gift from Prof. Massimiliano Mazzone) and P2 cancer cell lines were cultured in DMEM supplemented with 10% (v/v) heat-inactivated FCS, 300 µg/mL L-glutamine, 100 units/mL penicillin, and 100 µg/mL streptomycin (DMEM culture medium), at 37°C and 5% CO_2. Cells were checked for mycoplasma contamination regularly using the Venor GeM Classic kit (cat. nr. 11-1025).

In vivo passaging of cancer cells

The LLC-Thy1.1 P2 cell line was obtained by serial *in vivo* passaging via intratracheal injections with intubation (ITI; see Fig. 1F). For the first passage, $2*10^6$ LLC-Thy1.1 cells P0 were injected. 28 days post injection (dpi), the full lung was processed to a single cell suspension and Thy1.1$^+$ cells were isolated using CD90.1/Thy1.1 MicroBeads according to the manufacturer's instructions. Obtained cells were then cultured for 8 days, before being injected into new mice. The full lung was again processed 21 dpi and cultured. The supernatant was replaced after 24h to remove non-attaching cells. After 4 days of culture, tumour cells were detached and separated from fibroblasts via pipetting. Stable and consistent Thy1.1 expression was confirmed via flow cytometry.

Crystal violet (CV) colony formation assay

200 cancer cells/3 mL DMEM culture medium were seeded in triplicate in a 6-well plate (n=3). After 6 days, wells were washed with PBS and subsequently fixed with 4% PFA in PBS for 20 min at RT. After a PBS wash step, wells were incubated for 15 min with 600 µL of Crystal Violet (CV) staining mixture (2.5% (w/v) CV in 4:1 water-methanol) at RT. After a final wash under a deionised water tap, pictures were taken of individual wells. Colonies were quantified using ImageJ (Manual Thresholding: default method, black and white, 0-80, followed by Analyse Particles: size ≥15, circularity 0-1).

Limiting dilution assay (spheroid formation)

Cancer cells/200 µL 3D Tumorsphere Medium XF were seeded at different cell numbers (10000, 5000, 1000, 500, 100, 50, 10 and 1) in quadruplicate in round bottom 96-well ultra-low attachment microplates (Corning, # 7007) (n=3). Wells were imaged using the Incucyte S3 on day 3, 5 and 7 using the standard single spheroid scan settings.

Western blot

Cells were lysed with 150-250 µL of 2% protease inhibitor solution (cOmplete Tablets EASYpack; 1 tablet/1 mL 1% SDS) and 98% phosphatase inhibitor solution (Pierce Phosphatase Inhibitor Mini Tablets, 1 tablet/10 mL 1% SDS). Samples underwent 10 s sonication, followed by 5 min heating at 99°C. Protein concentration was determined with the Pierce BCA Protein Assay Kit (cat. nr. 23225) according to the manufacturer’s instructions. 20 µg of samples were run on SDS-PAGE gels and transferred to PVDF membranes. Membranes were washed with 0.1% Tween 20 in TBS (TBS-T), blocked for 1h using 5% milk in TBS-T and washed again. Next, they were incubated overnight at 4°C with primary antibodies (1:1000 in 5% BSA, except for PCNA 1:1000 in 5% milk). Membranes were washed three times for 10 min each, after which they were incubated with HRP-conjugated secondary antibodies (1:3000 in 5% milk) for 1h at RT. After three 10 min washes, membranes were developed using Pierce ECL Western Blotting Substrate (cat. nr. 32106) and imaged via chemiluminescence detection using the ImageQuant LAS 4000 (GE Healthcare Life Sciences).

Apoptosis staining

Cancer cells were collected together with the supernatant (0.25-1*10^6 cells) and centrifuged (450g, 5 min, 4°C). Cells were washed twice with MACS (0.5% FCS, 2 mM EDTA in HBSS) (450g, 5 min, 4°C), after which they were resuspended in 100 µL Annexin V Binding Buffer (BioLegend). 5 µL of APC Annexin V and 5 µL of 7-AAD were added, the cells were vortexed gently and incubated for 15 min at RT in the dark. 400 µL of Annexin V Binding Buffer was added and data was acquired within 4h.

Cancer cell injections

For subcutaneous (SUBCUT) injections, 1*10^6 LLC Thy1.1 P2 cells/100 µL HBSS were injected subcutaneously into the right flank. Tumour volumes were determined by calliper measurements and calculated using the formula: $V = \pi * \frac{(d^2 * D)}{6}$, where d is the shortest and D is the longest diameter. The maximal tumour volume allowed by the IACUC of the Vrije Universiteit Brussel is 2000 mm^3, which was not exceeded in this study.

For retro-orbital injections (RO), mice were anaesthetised via isoflurane inhalation (2-3% isoflurane at a flow rate of 1.0 L/min), followed by the subsequent injection of 2*10^5 LLC Thy1.1 P0 cells/100 µL HBSS and 100 µl HBSS into the RO venous sinus. The latter was done to eliminate any remaining cancer cells at the injection site. A 0.3 mL insulin syringe was used, and its needle was positioned at a 45° angle for injection.

For transthoracic injections (TT), mice were anaesthetised with ketamine (14 mg/mL) and xylazine (1 mg/mL) (anaesthetic dose (AD) = 7 µL per g body weight) through intraperitoneal (IP) injection. A 5-10 mm skin incision was made in the left chest, after which fat and muscle tissue were gently pulled away from the ribs and the left lobe was visualised. A 0.3 mL insulin syringe was advanced into the left lobe between the ribs and 1*10^6 cancer cells/50 µL 50%-50% HBSS-Matrigel or 100% HBSS were slowly injected intrapulmonary.

For intratracheal injections with intubation (ITI), mice were anaesthetised with ketamine/xylazine (1x AD) through IP injection. Mice were hung by their superior incisors on an intubation stand. A blunted catheter was inserted into the trachea, after which the needle was removed. 1-2*10^6 LLC-Thy1.1 cells/50 µL HBSS were administered through the catheter using a pipette. To ensure all cells were injected, 300 µL of air was subsequently injected into the catheter using a 'pre-filled' syringe.

For the direct intratracheal inoculation (ITD or ORTHO) (Supplementary Movie 1), mice were anaesthetised via isoflurane inhalation (3-4% isoflurane at a flow rate of 1.0 L/min). Once adequate anaesthesia was observed, mice were partially suspended by their superior incisors, their tongue was gently pulled out to one side using small tweezers and then kept in this position during the procedure using index finger and thumb. 1*10^6 LLC-Thy1.1 cells/50 µL HBSS were administered into the mouth using a pipette and subsequently inhaled by the mouse. Inhalation was promoted via gentle massaging of the mouse thorax. After inhalation of the cancer cells, an additional 20 µL of HBSS was administered in the same manner to ensure that all cancer cells reached the lungs and were cleared from the mouth. Mock injections with 50 µL HBSS, followed by 20 µL HBSS served as a control.

Micro-CT (µCT) imaging

Orthotopic tumour growth was followed-up via µCT scanning (MILabs) under isoflurane anaesthesia (2-3% isoflurane at a flow rate of 1.0 L/min), with the standard full body image settings (voltage 50 kV, current 0.39 mA, exposure time 40 ms, voxel size 80 µm, scan angle 360°, step degree 0.75°) in a single mouse bed. The image was reconstructed using the MILabs Auto Rec software and 3D reconstruction and analysis were done using the Imalytics Preclinical software (v3.1). Lungs were segmented by thresholding the image at -250 Hounsfield units (HU), selected using autofill and finally smoothened. Tumour nodules were delineated manually.

Therapy

Mice received multiple cycles of anti-PD-1 mAb (clone RMP1-14 200 µg; 10 mg/kg; three times per week i.p.), cisplatin (70 µg; once per week i.p.) or the combination of the two as from the presence of tumour foci was confirmed by µCT for ORTHO tumours or as from a tumour size round 100 mm^3 for SUBCUT tumours (Schematic overview in Fig. 10A). Isotype mAb (anti-βGAL, clone GL117) and vehicle (0,9% saline) were given as control. For ORTHO, the end point was defined as a weight loss (20% of max body weight) of in combination with a high tumour burden observed on µCT. Of note, mice were considered dropouts if they exhibited chemotherapy-related weight loss (max body weight as reference point) accompanied by low tumour burden. For SUBCUT, the end point was defined as a tumour reaching 1400 mm^3 or the occurrence of ulceration.

Lung collection and dissociation

For the SEPARATE-Seq samples, mice were sacrificed via anaesthetic overdose through RO injection of 100 µL ketamine (14 mg/mL) and xylazine (1 mg/mL), containing 2 µg of CD45-biotin antibody. In experiments where no vascular/intratissue distinction had to be made, anaesthetic overdose was given through an IP (2x AD) or RO (100 µL) injection. The inferior vena cava was exposed and cut, after which lungs were perfused with 20 mL HBSS via the right heart ventricle using a 27G needle. Perfused lungs were harvested and collected in 500 µL RPMI+10% FCS. In the case of tumour-bearing lungs, tumour and adjacent tissue were separated using spring scissors, after which both tissues were processed according to the following protocol. Samples were cut into very small pieces and 250 µL of enzyme mix (10 U/mL collagenase I, 400 U/mL collagenase IV, 30 U/mL DNase I in HBSS) was added for digestion. The suspension was incubated in a ThermoMixer C (Eppendorf) (1500 rpm, 25 min, 37°C). After incubation, 750 µL of RPMI+10% FCS was added. The suspension was mixed extensively through pipetting and transferred over a 70 µm nylon filter. The cell suspension was centrifuged (450g, 6 min, 4°C), after which the supernatant was discarded. The cell pellet was resuspended in 1 mL of lysis buffer (155 mM ammonium chloride, 10 mM potassium bicarbonate, 500 mM EDTA in Milli-Q water). Samples were incubated for 3 min at room temperature (RT) and then neutralised by adding 5 mL of RPMI+10% FCS. Suspensions were filtered and centrifuged (450g, 6 min, 4°C). The supernatant was discarded, and the pellet was resuspended in the desired amount of MACS or HBSS, resulting in a single-cell suspension.

Subcutaneous tumour processing

Animal sacrifice was performed in the same manner as for lung collection. No perfusion was performed. Subcutaneous tumours were collected in 1 mL of RPMI+10% FCS for processing. Tumours were extensively cut before the addition of 500 µL of enzyme mix. Samples were incubated with enzyme mix in a ThermoMixer C (1500 rpm, 25 min, 37°C). After incubation, each sample was transferred to a well in a 6-well plate and the tissue was further dissociated by squashing with the backside a syringe plunger. Samples were then transferred over a 70 µm nylon filter, followed by centrifugation (450g, 6 min, 4°C). The supernatant was discarded, and the cell pellet resuspended in 1 mL of lysis buffer. Samples were incubated for 3 min at RT and then neutralised by adding 5 mL of RPMI+10% FCS. Suspensions were filtered and centrifuged (450g, 6 min, 4°C). The supernatant was discarded, and the pellet was resuspended in the desired amount of MACS or HBSS, resulting in a single-cell suspension.

Flow cytometry and cell sorting

Samples for flow cytometry analysis were incubated with Fixable Viability Dye eFluor 575 (1:2000 in HBSS) for 30 min at 4°C. Next, cell suspensions were washed with HBSS (450g, 6 min, 4°C) and resuspended in MACS buffer. To prevent non-specific antibody binding to Fcγ receptors, cells were preincubated with anti-CD16/CD32 (clone 2.4G2, in house) antibody. Cell suspensions (1-2*10^6 cells/tube) were then incubated for 30 min at 4°C with fluorescently labelled antibodies diluted in MACS buffer and 5 µL/tube BD Horizon Brilliant Stain Buffer, then washed with MACS buffer (450g, 6 min, 4°C). From this one on, all incubation steps were performed in the dark.

For IFNγ staining, after obtention of a single cell suspension, cells were incubated for 4h in 200 µL of RPMI supplemented with 10% (v/v) FCS, 300 µg/mL L-glutamine, 100 units/mL penicillin, 100 µg/mL streptomycin, 1% (v/v) MEM nonessential amino acids, 1 mmol/L sodium pyruvate, and 0.02 mmol/L 2-mercaptoethanol, 0.1% (v/v) Brefeldin A (1:1000), ionomycin (1µg/mL) and PMA (20ng/mL). Cells were then washed with HBSS (450g, 6 min, 4°C) and subjected to the previous extracellular labelling steps, followed by the intracellular staining explained below.

For intracellular staining, after extracellular staining was completed, samples were centrifuged (450g, 6 min, 4°C), resuspended in 100 µL eBioscience Fixation Buffer (75% Diluent, 25% Concentrate) and incubated for 30 min at 4°C. Next, cells were washed with eBioscience Permeabilization Buffer (1:10 in Milli-Q water) (800g, 6 min, 4°C). Cells were resuspended in Permeabilization Buffer containing the intracellular antibodies of interest. After incubation at 4°C overnight, cells were washed with Permeabilization Buffer (800g, 6 min, 4°C). The supernatant was discarded and the FACS tubes were vortexed before data acquisition.

Flow cytometry data were acquired using a BD FACSCanto II or a BD FACSymphony A3 and analysed using FlowJo. The gating strategy to identify the main immune cell populations is shown in Supplementary Fig. 4C. Notably, alveolar macrophages (AMs) were outgated prior to the vascular-intratissue separation, due to their intrinsic autofluorescence and their residence in the alveolar space.

Human scRNA-Seq data processing and analysis

The human single-cell atlas dataset of Salcher *et al.* (2022)[14], which included samples from 19 studies and 318 NSCLC patients, was downloaded from https://luca.icbi.at (LuCA extended atlas) as a Seurat v5 R object. Further processing of the data was done in R using Seurat v.4.3.0. We extracted all immune cells, using the provided “ann_coarse” cell type labels in the Seurat object metadata. Additionally, we subsetted only the cells from primary tumours and non-tumoural ‘normal’ adjacent tissue (using the “origin” cell metadata) of patients. Of note, only the studies in which the full tissue or isolated CD45$^+$ cells were sequenced, were included, and not those where enrichment for a certain cell type was done. Supplementary Data 1 shows included samples and patient metadata. Gene names were converted from Ensembl ID to gene symbol using the mapIds function of the ensembldb v2.18.4 package and the EnsDb.Hsapiens.v86_2.99.0 package. The immune myeloid and the lymphoid compartments were subclustered and processed separately. Raw gene expression counts of each compartment were normalised, followed by the selection of highly variable genes (HVG), scaling by gene and principal component analysis (PCA). Next, batch correction was performed on the PCA embeddings using harmony v1.2.0 with theta=1 and the originating study identity as batch parameter. The corrected PCA embeddings were used for downstream analysis, including Louvain clustering and Uniform Manifold Approximation and Projection (UMAP). The cell type identity of each cluster was determined by their expression of specific cell type marker genes. Clusters that were outliers due to low library size and number of expressed genes and lacked a distinct gene signature compared to the remaining clusters were excluded. The full immune cell dataset was further processed by selection of HVG, scaling, PCA, batch correction using harmony with theta =1 and UMAP analysis. Some cell populations, including macrophage/monocyte, proliferating lymphoid cells, CD4$^+$ T cells, ISG-expressing T cells, neutrophils and NK cells, were extracted and further subclustered to annotate them in more detail. Signature scores were calculated using the AddModuleScore function from Seurat.

scRNA-Seq of cancer cell lines: data acquisition and library preparation (10x Genomics)

After 7 days in culture, supernatant was removed and 2*10^6 LLC-Thy1.1 P0 and 2*10^6 LLC-Thy1.1 P2 cells were collected using HBSS+1% FCS. Cells were centrifuged (400g, 5 min, 4°C) and resuspended in 45 µL PBS+1% BSA. The cells were incubated for 30 min at 4°C with a unique TotalSeq-A cell hashing antibody (HTO; 1:250; P0 and P2 labelled with TotalSeq-A0314 and -A0315 resp.) and TruStain FcX PLUS (1 µL/sample). Cells were washed (400g, 5 min, 4°C) and the supernatant discarded. Next, cells were incubated at RT for 5 min with 100 µL cell multiplexing oligonucleotides (CMOs; P0 and P2 labelled with CMO-310 and -311 resp.). Samples were washed (400g, 5 min, 4°C) and resuspended in PBS+1% BSA for sorting. 7-AAD was added to sort out live cells using a BD FACSAria II. Sorted single-cell suspensions were centrifuged and the cell pellet resuspended at an estimated final concentration of 1000 cells/µL. Cells were loaded on a Chromium GemCode Single Cell Instrument (10X Genomics) to generate single-cell Gel beads-in-EMulsion (GEM). The scRNA-Seq libraries were prepared using the GemCode Single Cell 3′ Gel Bead and Library kit version Next GEM v3.1 (cat. nr. 1000121) according to the manufacturer's instructions (10X Genomics, User Guide CG000388) with the addition of the amplification primer 5’-GTGACTGGAGTTCAGACGTGTGCTCTTCCGAT*C*T-3´ (3 nM) during cDNA amplification to enrich the TotalSeq-A hashing protein oligos. Size selection with SPRIselect Reagent Kit (Beckman Coulter, cat. nr.

B23318) was used to separate amplified cDNA molecules for 3′ gene expression, hashing protein and hashing lipid construction. TotalSeq-A protein library construction including sample index PCR using Illumina's Truseq Small RNA primer sets and SPRIselect size selection was performed according to the manufacturer's instructions. The cDNA content of pre-fragmentation and post-sample index PCR samples was analysed using the 5200 Fragment Analyzer (Agilent). Sequencing libraries were loaded on an Illumina NovaSeq flow cell at VIB Nucleomics Core with sequencing settings according to the recommendations of 10X Genomics. The Cell Ranger pipeline (10X Genomics, version 7.1.0) was used to perform sample demultiplexing and to generate FASTQ files for read 1, read 2, and the i5, i7 sample index for the gene expression, HTO and CMO libraries. Read 2 of the gene expression libraries was mapped to the reference genome (mouse mm10). Subsequent barcode processing, unique molecular identifiers filtering, and gene counting was performed using the Cell Ranger software (10X Genomics).

scRNA-Seq of cancer cell lines: data analysis

The multi pipeline of the Cell Ranger software (10x Genomics) v.7.1.0 was used to perform alignment of the RNA sequencing reads to the reference genome (*Mus musculus* mm10-2020-A), demultiplexing of the CMO-labelled samples and generation of the RNA and HTO/CMO UMI count matrices. The mean number of RNA reads per cell was 10,561 with a sequencing saturation metric of 31.26%. The HTO and the CMO libraries yielded 98 and 3,793 mean reads per cell, and 92.57% and 20.23% sequencing saturation, respectively. Of all cell-associated barcodes (as defined by Cell Ranger), 88.9% were assigned to a single CMO sample and 7.71% were assigned as CMO multiples. The gene expression matrix processing and analysis was performed as described below in the SEPARATE-Seq data analysis section. The HTO count matrix processing was performed as described below in the SEPARATE-Seq data analysis section. The HTO demultiplexing was performed with the 'DeMULTIplex' method[27] using Seurat's MULTIseqDemux function with default parameters.

SEPARATE-Seq: data acquisition and library preparation (10x Genomics)

Lungs of mock injected and tumour-bearing mice (21 dpi) and subcutaneous tumours (18 dpi with tumour size (TS) and tumour weight (TW) for HTO1: TS=1086.02 mm^3, TW=0.5 g; HTO2: TS=1154.32 mm^3, TW= 0.44 g; HTO3: TS=1016.18 mm^3, TW= 0.56 g; HTO4: TS=972.00 mm^3, TW= 0.46 g) were processed according to the regular tissue processing procedures, with the addition of actinomycin D (ActD) to each buffer to block transcription during the processing. The ActD concentration was decreased along the way: 30 µM during initial cutting, 15 µM during the enzymatic digestion and 3 µM for all the following steps up until staining. Of note, we used the same murine samples to perform both flow cytometry and SEPARATE-Seq (combined with scRNA-/CITE-Seq) in parallel to allow for the correlation between protein and transcriptomic data. Thus, 2*10^6 cells were used for CITE-Seq and leftover cells were used for flow cytometry analysis. For adjacent and mock samples, exact sample matching was not feasible as the entire adjacent tissue was used for sequencing due to the limited cell numbers. Cells were incubated in PBS+1% BSA with TruStain FcX PLUS (1 µL) at 4°C. The staining mix was added to obtain a final volume of 50 µL, containing PBS+1% BSA with fluorescent antibodies (CD45 APC-Cy7 and Thy1.1 APC; 1:666), a unique mouse TotalSeq-C cell hashing antibody (HTOs;1:1000), a unique TotalSeq-C Streptavidin (STREPs; 1:833) and a mouse CITE-Seq antibody panel. The latter contains 193 unique oligoconjugated antibodies and isotype controls (Supplementary Table 2). Four replicates were tagged and pooled using HTOs specific against mouse CD45 and MHC class I (TotalSeq-C0301, TotalSeq-C0302, TotalSeq-C0303, TotalSeq-C0305) and STREPs (TotalSeq-C971, TotalSeq-C972, TotalSeq-C973, TotalSeq-C974). HTOs were used to (i) be able to discriminate from which mouse a cell originated and to distinguish the origin of cell from different mice and (ii) relate adjacent- and tumour-derived cells from individual mice (in the case of ORTHO lungs). STREPs were used to verify whether analysed cells were present in the tissue or in the vasculature at the moment of sacrifice. Additionally, HTOs and STREPs were used to remove doublets in analysis steps, by matching STREP and HTO. After 20 min of incubation at 4°C, cells were washed (400g, 5 min, 4°C) and resuspended in PBS+1% BSA. 7-AAD (5 µL) staining was used to exclude dead cells. 7-AAD$^-$CD45$^+$Thy1.1$^-$ cells were sorted from single-cell suspensions using a BD FACSAria II and BD FACSAria III.

Sorted single-cell suspensions were centrifuged and the cell pellet resuspended at an estimated final concentration of 1,400 cells/µL. Cells were loaded on a Chromium GemCode Single Cell Instrument (10X Genomics) to generate single-cell Gel beads-in-EMulsion (GEM). The DNA libraries were prepared using the GemCode Single Cell 5′ Gel Bead and Library kit, version Next GEM v2 (cat. nr. 1000263) according to the manufacturer's instructions (10X Genomics, User Guide CG000330). Size selection with SPRIselect Reagent Kit (Beckman Coulter, cat. nr. B23318) was used to separate amplified cDNA molecules for 5′ gene expression and cell surface protein construction. The cDNA content of pre-fragmentation and post-sample index PCR samples was analysed using the 5200 Fragment Analyser (Agilent). Sequencing libraries were loaded on an Illumina NovaSeq flow cell at VIB Nucleomics Core with sequencing settings according to the recommendations of 10X Genomics, pooled in a 75:25 ratio for the combined 5′ gene expression and cell surface protein samples, respectively. The Cell Ranger pipeline (10X Genomics, version 7.1.0) was used to perform sample demultiplexing and to generate FASTQ files for read 1, read 2, and the i5, i7 sample index for the gene expression and cell surface protein libraries. Read 2 of the gene expression libraries was mapped to the reference genome (mouse mm10). Subsequent barcode processing, unique molecular identifiers filtering, and gene counting was performed using the Cell Ranger software (10X Genomics).

SEPARATE-Seq: CITE-Seq analysis

The Cell Ranger software v7.1.0 (10x Genomics) was used to perform alignment of the RNA sequencing reads to the reference genome (*Mus musculus* mm10-2020-A) and generation of the RNA and ADT/HTO/STREP UMI count matrices. The average of the mapped mean RNA reads per cell was 30,034 ± 1,046 SD, with an average sequencing saturation metric of 70.3% ± 8.2% SD. The ADT/HTO/STREP libraries yielded 10,346 ± 1,948 SD mean reads per cell, with 55.13% ± 5.02% SD sequencing saturation. Further analysis of UMI count data was performed using R v4.3.1. and the Seurat v4.3.0/5.0.3 R package, developed by the Satija lab. The R packages SCRAN v1.22.1, Scater v1.22.1 and DropletUtils v1.14.2 were used to pre-process and filter the gene expression matrices. Cell barcodes associated with empty droplets were removed from the raw expression data using the EmptyDrops function of DropletUtils. The data was then subjected to further quality control. Outliers for total RNA UMI counts, number of genes and percent mitochondrial genes per cell were determined using the Scater package. Outliers were defined using as a threshold three median absolute deviations (MAD) away from the median for each quality control parameter, independently for each scRNA-seq library (above the median for the percent mitochondrial genes and below the median for UMI counts and number of genes). Additionally, all cells with percent mitochondrial genes above 20% were removed. Potential cell doublets were tagged by calculating a doublet score per cell, using the random approach of the scDblFinder function from the scDblFinder v1.8.0 package. Subsequently, the data was normalised and scaled to ensure that the mean expression of each gene across all cells was 0 and the standard deviation was equal to 1. Next, HVG were selected, and dimensionality reduction was performed using PCA. The number of principal components used for downstream analysis was chosen based on heatmaps of the expression of the top genes driving each principal component and an Elbow plot. Unsupervised clustering was performed on the top PCA embeddings using Seurat. The genes and surface proteins, specifically expressed in each cluster, were identified via differential expression (DE) analysis with the FindMarkers function of Seurat (Wilcoxon Rank Sum test). The p-values of DE were adjusted for multiple testing with Bonferroni correction. UMAP allowed for a two-dimensional visual representation of the data.

The ADT, HTO and STREP count matrices were denoised using CellBender v0.3.0, using fpr=0.1 as recommended for CITE-Seq data. This package removes counts due to ambient RNA, not associated with intact cells, random barcode swapping, or unbound and unwashed antibodies. Then the ADT, HTO and STREP matrices were further processed as described previously[135]. In brief, the cell barcodes, associated with artefact cells based on the RNA expression analysis were discarded, and the remaining data was normalised using the ASINH_GEOM transformation (inverse hyperbolic sine transformation with a cofactor).

For the HTO and STREP count matrices demultiplexing, three methods were tested: (i) Seurat's HTODemux algorithm[26], (ii) the DeMULTIplex classification algorithm[27] as implemented in Seurat, using the MULTIseqDemux function and, (iii) the DeMULTIplex2 algorithm[136] using deMULTIplex2 v1.0.1. For the STREP demultiplexing, we varied the quantile threshold between the default (0.99) and 0.999999, while for HTO the default threshold was used. When applying DeMULTIplex for the STREP matrix, we used either the default quantile threshold of 0.7, or 0.9. The default threshold was used for the HTO matrix. Finally, DeMULTIplex2. For both HTO and STREP, we ran the three demultiplexing methods either on the whole dataset, or for each major cell type separately (*algorithm*_CT; neutrophils, non-classical monocytes, classical monocytes, macrophages, proliferating macrophages, AMs, DC, T/ILC, NK, B cells, proliferating lymphocytes, doublets, artefacts). The demultiplexing results were evaluated qualitatively by UMAP diagnostic plots, based on the normalised and scaled HTO or STREP counts, using 100 n.neighbours. Then, the cells were assigned to the intratissue category, if they were classified as negative for all STREPs and positive for one of the HTOs. Alternatively, the cells were assigned to the vascular category, if they were classified as STREP positive and HTO positive for the same corresponding sample. STREP-X-HTO-Y combinations, along with STREP$^+$HTO$^-$ or STREP$^-$HTO$^-$ were identified as technical artefacts. Different combinations of demultiplexing methods were used during this assignment (Supplementary Data 2). The results of the vascular/intratissue assignment for the different demultiplexing method combinations were correlated with the proportions of vascular/intratissue cells identified by flow cytometry for neutrophils, monocytes, macrophages, cDC1, cDC2, CD8$^+$ T, CD4$^+$ T, Treg, NK and B cells, using the Pearson statistic. Ultimately, DeMULTIplex with quantile threshold of 0.9 for the STREP matrix, and DeMULTIplex2 for the HTO matrix were chosen as an optimal demultiplexing strategy based on the correlation with flow cytometry data and the number of recovered intratissue/vascular cells.

Multiplets and negative cells, as well as the cells assigned to non-matching HTO-STREP samples, were excluded from further analysis. Hence, our final dataset solely contained vascular (HTO$^+$STREP$^+$) and intratissue (HTO$^+$STREP$^-$) cells with matching tags.

We excluded artefact cells, identified by the final HTO and STREP demultiplexing, as well as those cell populations that showed both a high doublet score and expression of markers specific for two different cell types. Additionally, we excluded clusters that were outliers due to low RNA counts and number of expressed genes and/or high percentage of mitochondrial genes, and that lacked a distinct gene signature compared to the other clusters. Finally, we repeated the HVG selection, scaling, PCA dimensionality reduction and UMAP projection on the cleaned gene expression matrix. Some of the identified compartments were extracted and further subclustered, following the same procedure: HVG selection, scaling, PCA, clustering and UMAP analysis. Despite quality control and filtering steps, several cell types (B cells, T cells, cDCs, neutrophils, AMs, macrophages) showed a population with a high mitochondrial gene signature (Mito^{high}) upon subclustering, generally present in all SEPARATE-Seq sample types. Signature scores were calculated using the AddModuleScore function from Seurat.

Human – mouse gene correlation

Gene symbols were converted between human and mouse based on one-to-one orthology using biomartR v2.64.0. Then, 2000 shared highly variable genes (HVG) were selected using the “SelectIntegrationFeatures” function (Seurat), and their scaled expression was averaged per cell cluster. Pearson correlation coefficients were calculated between the corresponding mouse and human cell clusters, both for the broad immune cell types and subsets.

Vizgen MERSCOPE spatial transcriptomics: sample preparation

Slides from ITI inoculated LLC-Thy1.1 P2 lungs (n=2; referred to as VIZ1 and VIZ2) were analysed using the Vizgen MERSCOPE spatial profiling platform, based on Multiplexed Error-Robust Fluorescence in situ Hybridization (MERFISH). Mice were euthanised by IP anaesthetic overdose (2x AD). The lungs were perfused with 10 mL HBSS, followed by inflation with OCT:HBSS (1:1). The inflated lungs were transferred to HBSS (4°C) to separate the lobes for freezing. The separated lobes were embedded in Tissue-Tek O.C.T. Compound (Sakura) and frozen in an isopentane bath chilled by liquid nitrogen. Embedded lung lobes were stored at -80°C until cryosectioning. The tissue blocks were transferred to -20°C for temperature adjustment approximately 30 min before sectioning. The functionalised, bead-coated Vizgen slides were warmed up to RT before use. 10 μm sections were cut (Leica CM1850 Cryostat) and the OCT surrounding of the frozen tissue was gently removed using a fine brush. The tissue slices were then placed on the designated area of the slides. The filled slides were placed in a petri dish, incubated at -20°C for 5 min and fixed with 10 mL of 4% PFA-PBS for 15 min at RT. The sections were washed three times with 10 mL of PBS for 5 min, followed by a 70% ethanol wash for 5 min. Following the fix/wash procedure, the slides were transferred into the provided polytube bags with 10 mL 70% ethanol after which the prepared samples were shipped to Vizgen (USA) to perform MERFISH imaging, decoding and cell segmentation.

Fluorescent probes were used to visualise gene expression on tissue samples, in this case a panel of 322 genes was designed of which 287 genes were targetable, meaning sufficient target regions exist for the probes and there is no overabundance of the transcripts (Supplementary Table 3). Gene expression and coordinates matrices were obtained from the instrument output. For cell segmentation, the Cellpose2 algorithm was used, which leverages both the DAPI and PolyT cell boundary stain to more accurately assign RNA transcripts.

Vizgen MERSCOPE spatial transcriptomics: analysis

Data were analysed using MERSCOPE Vizualizer software v2.3 (Vizgen Technologies) and the Scanpy v1.10.2, Squidpy v1.5.0, and Monkeybread v1.0.0 packages in Python v3.9.13. Cells with less than 5 detected transcripts and a volume lower than 10 were left out for further analysis (termed “not identified”). Analogous to scRNA-seq data, data from spatial transcriptomics were normalised to the total expression, scaled (log transformation), dimensionally reduced (PCA), clustered (Leiden clustering) and a UMAP was calculated. Clusters were subsequently annotated based on differential gene expression, known marker genes and gene signatures from previous scRNA-seq annotation (Supplementary Table 4). Tumour and adjacent regions were delineated manually via the MERSCOPE Vizualizer. The tumour core was defined as the centroid of the manually delineated tumour nodule, calculated by the “centroid” function of the Shapely v2.0.6 package.

Niches were calculated with neighbourhood analysis using the Monkeybread package. Clustering parameters were set to resolution 0.45, radius 50 and 60 n_neighbours. Niches were defined as “other” when containing less than 150 cells.

Transcripts of genes (ISG) were visualised on the DAPI/PolyT stain image (merged image) using the MERSCOPE Vizualizer software. Transcripts detected across all planes were shown.

Analysis of ISG signature on human data

Human data was retrieved from TCGA and GTEx databases, using GEPIA2 software[137] (Human LUAD: 483 T, 347 N). Matched normal data (N) retrieved from TCGA normal + GTEx normal databases. ISG signature was defined as *RSAD2, ISG15, OAS3, CXCL10, IFIT1, OASL, MX1, CXCL9.* The expression data are first $\log_2$(TPM+1) transformed for differential analysis and the $\log_2$FC is defined as median(Tumour) - median(Normal). Genes with higher |$\log_2$FC| values (1) and lower q values (0.01) than pre-set thresholds are considered differentially expressed genes. One-way ANOVA for differential analysis, using disease state (Tumour or Normal) as variable for calculating differential expression. Transcripts Per Million (TPM).

Analysis of spatial distribution of ISGs on human data

The publicly available dataset was retrieved from the 10x Genomics website (Dataset: FFPE Human Lung Cancer Data with Human Immuno-Oncology Profiling Panel and Custom Add-on). Sample was FFPE-preserved tissue purchased from Discovery Life Sciences (Lung NSCLC; Stage I-B; Grade 2). The Xenium Human Immuno-Oncology Profiling Panel (380 genes) was pre-designed by 10x Genomics. Transcripts were visualised using Xenium Explorer v3.1.1.

Immunohistochemistry (IHC): tissue preparation and imaging

Immunostaining with antibodies specific for CD4, CD8, CD20 and PanCK was performed according to conventional protocols[138]. Fluorescence samples are prepared independently of spatial transcriptomics samples. ORTHO tumour-bearing lungs (14 and 21 dpi) were collected after perfusion, split into tumour and adjacent tissue in pieces of ±5x5 mm and transferred to 4% PFA for 24h. Thereafter, samples were transferred to 70% ethanol. Tumour specimens were fixed in neutral buffered 10% formalin solution and embedded in paraffin as per standard procedures. In brief, 4 µm-thick tissue sections were deparaffinised and rehydrated in a descending alcohol series (100, 96, 70, and 50%), followed by antigen retrieval with Target Retrieval Solution (Leica) in pH 9. Sections were treated with normal horse serum (2.5%) for 20 min and incubated with primary antibodies. First, staining was performed with anti-mouse CD4 (1:150, 1h), followed by the revelation of enzymatic activity (ImPRESS HRP anit-rabbit IgG (peroxidase) polymer for detection, AEC+ substrate chromogen system for revelation). Sections were counterstained with hematoxylin (DAKO) for 30 seconds. Images were acquired using a Leica Aperio AT2 scanner (Leica). Thereafter the same sections were restained with antibodies specific for CD20 (1:100, 1h incubation; ImPRESS HRP anti-rabbit IgG (peroxidase) polymer for detection, AEC+ substrate chromogen system for revelation), PanCK (1:50, 2h incubation; ImPRESS HRP anti-rabbit IgG (peroxidase) polymer for detection, AEC+ substrate chromogen system for revelation) and CD8 (1:250, 1h incubation; ImPRESS EXCEL amplified anti-rabbit IgG for detection, DAB+ substrate chromogen system for revelation). Between every staining step the slides were scanned, and final image was composed by the HALO10 software (Indica labs) using the registration algorithm.

H&E tissue preparation and staining

For H&E, lungs were perfused with HBSS and inflated with 4% PFA. Fixation was done for 24h in 4% PFA. Afterwards, sectioning and H&E staining was performed using standard protocols.

Quantification and statistical analysis

The obtained data were either analysed using GraphPad Prism v10.3.1 (GraphPad Software, La Jolla, California, United States of America) or R. Statistical tests that were applied to compare groups are shown in the legends of Figures. The (corrected) p-value for statistically relevant differences is indicated in graphs as follows: *p≤0.05, **p≤0.01, ***p≤0.001, ****p≤0.0001.

To assess the differential abundance between experimental conditions (SEPARATE-Seq), we employed generalized linear mixed models with a negative binomial distribution (nbinom2: lowest AIC, best residuals, best fit), implemented using the glmmTMB package in R. Models were fit separately for each pairwise comparison of interest between conditions 1 and 2, restricting the dataset to the relevant subsets of observations. The following comparisons were made for general immune cell types and specific immune cell subsets:

(1) 'ORTHO-T vs SUBCUT'/'ORTHO-T vs ORTHO-A'/'ORTHO-A vs ORTHO-M' within total immune cells
(2) 'ORTHO-T vs SUBCUT'/'ORTHO-T vs ORTHO-A'/'ORTHO-A vs ORTHO-M' within vascular/intratissue immune cells
(3) SUBCUT/ ORTHO-T/ORTHO-A/ORTHO-M: 'intratissue vs vascular' immune cells

The employed model:

$$\begin{aligned}&\mathrm{glmmTMB}(\mathrm{count} \sim \mathrm{cond} * \mathrm{cells} + \mathrm{offset}(\log(\mathrm{total\_count}) + (1|\mathrm{mouse}),\\&\qquad \mathrm{dispformula} = \ \sim 1 + (1|\mathrm{cell}),\\&\qquad \mathrm{family} = \mathrm{nbinom2}(\mathrm{link} = \log),\\&\qquad \mathrm{data} = \mathrm{droplevels}(\mathrm{cell\_excl}))\end{aligned}$$

with count: raw count of the cell subset of interest in a specific condition; cond: conditions (= sample type for comparisons (1) and (2), and location for comparison (3)); cells: cell subset; total_count, raw count of the total cells within a mouse for comparisons (1) and (3) or raw count of the total cells within a specific location (vascular/intratissue) within a mouse for comparison (2); cell_excl: cell (sub)types which were not present in one of both conditions and hence excluded from the analysis.

Post hoc contrasts of conditions within each cell type were obtained using the emmeans package in R. Pairwise comparisons were adjusted for multiple testing via the Benjamini–Hochberg correction method. Quality control (QC) of residuals and model fit were quantified via the DHARMa package. All comparisons are listed in Supplementary Data 3.

For the comparison between male and female the same model was used, using gender as condition and employing the model to each sample type separately.

Human LUAD data was analysed in a similar manner employing the following model:

$$\begin{aligned}
&\mathrm{glmmTMB(count \sim cond * cells + offset(log(total\_count) + (1|study) + (1|donor\_ID),}\\
&\qquad\mathrm{dispformula = \ \sim 1 + (1|cell),}\\
&\qquad\mathrm{family = nbinom2(link = log),}
\end{aligned}$$

With count: raw count of the cell subset of interest in a specific condition; cond: conditions (= sample type); cells: cell subset; total_count, raw count of the total cells within a patient (donor_ID) per condition; cell_excl: cell (sub)types which were not present in one of both conditions and hence excluded from the analysis.

DATA AVAILABILITY

The LLC-Thy1.1 P2 mouse lung cancer cell line developed in this study will be deposited to American Type Culture Collection (ATCC). SEPARATE-Seq data and cell line scRNA-Seq data generated in this study have been deposited at GEO (NCBI) under accession number GSE304864 and are publicly available as of the date of publication (https://single-cell.be/Laouimmunology/SEPARATESeq). Spatial transcriptomics data (Vizgen Merscope) generated in this study have been deposited at GEO under accession number GSE325769. This paper analyses existing, publicly available data, including the single-cell lung cancer atlas (LuCA) (extended atlas)[14] and the subcutaneous LLC dataset[18]. Supplementary Data 1 lists the included patient samples and patient metadata from LuCA. Accession numbers are listed in Supplementary Table 5. Any additional information required to reanalyse the data reported in this paper is available from the corresponding author upon request. Source data are provided with this paper.

REFERENCES

1. Bray, F., Laversanne, M., Sung, H., Ferlay, J., Siegel, R.L., Soerjomataram, I., and Jemal, A. (2024). Global cancer statistics 2022: GLOBOCAN estimates of incidence and mortality worldwide for 36 cancers in 185 countries. CA: A Cancer Journal for Clinicians *74*, 229–263. https://doi.org/10.3322/caac.21834.

2. Zhang, Y., Vaccarella, S., Morgan, E., Li, M., Etxeberria, J., Chokunonga, E., Manraj, S.S., Kamate, B., Omonisi, A., and Bray, F. (2023). Global variations in lung cancer incidence by histological subtype in 2020: a population-based study. The Lancet Oncology *24*, 1206–1218. https://doi.org/10.1016/S1470-2045(23)00444-8.

3. Kargl, J., Busch, S.E., Yang, G.H.Y., Kim, K.-H., Hanke, M.L., Metz, H.E., Hubbard, J.J., Lee, S.M., Madtes, D.K., McIntosh, M.W., et al. (2017). Neutrophils dominate the immune cell composition in non-small cell lung cancer. Nat Commun *8*, 14381. https://doi.org/10.1038/ncomms14381.

4. Stankovic, B., Bjørhovde, H.A.K., Skarshaug, R., Aamodt, H., Frafjord, A., Müller, E., Hammarström, C., Beraki, K., Bækkevold, E.S., Woldbæk, P.R., et al. (2019). Immune Cell Composition in Human Non-small Cell Lung Cancer. Front. Immunol. *9*. https://doi.org/10.3389/fimmu.2018.03101.

5. Soo, R.A., Chen, Z., Yan Teng, R.S., Tan, H.-L., Iacopetta, B., Tai, B.C., and Soong, R. (2018). Prognostic significance of immune cells in non-small cell lung cancer: meta-analysis. Oncotarget *9*, 24801–24820. https://doi.org/10.18632/oncotarget.24835.

6. Suzuki, K., Kachala, S.S., Kadota, K., Shen, R., Mo, Q., Beer, D.G., Rusch, V.W., Travis, W.D., and Adusumilli, P.S. (2011). Prognostic Immune Markers in Non–Small Cell Lung Cancer. Clin Cancer Res *17*, 5247–5256. https://doi.org/10.1158/1078-0432.CCR-10-2805.

7. Dagogo-Jack, I., Valiev, I., Kotlov, N., Belozerova, A., Lopareva, A., Butusova, A., Samarina, N., Boyko, A., Xiang, Z., Johnson, M., et al. (2023). B-Cell Infiltrate in the Tumor Microenvironment Is Associated With Improved Survival in Resected Lung Adenocarcinoma. JTO Clinical and Research Reports *4*. https://doi.org/10.1016/j.jtocrr.2023.100527.

8. Tamminga, M., Hiltermann, T.J.N., Schuuring, E., Timens, W., Fehrmann, R.S., and Groen, H.J. (2020). Immune microenvironment composition in non-small cell lung cancer and its association with survival. Clinical & Translational Immunology *9*, e1142. https://doi.org/10.1002/cti2.1142.

9. Lee, I.-H., Wang, H.-Y., Chen, Y.-Y., Chen, C.-Y., and Liao, H.-F. (2024). Synergistic B and T lymphocyte interaction: prognostic implications in non-small cell lung cancer. Am J Cancer Res *14*, 1227–1242. https://doi.org/10.62347/TDIV2436.

10. Hynds, R.E., Frese, K.K., Pearce, D.R., Grönroos, E., Dive, C., and Swanton, C. (2021). Progress towards non-small-cell lung cancer models that represent clinical evolutionary trajectories. Open Biology *11*, 200247. https://doi.org/10.1098/rsob.200247.

11. Janker, F., Weder, W., Jang, J.-H., and Jungraithmayr, W. (2018). Preclinical, non-genetic models of lung adenocarcinoma: a comparative survey. Oncotarget *9*, 30527–30538. https://doi.org/10.18632/oncotarget.25668.

12. Jia, H., Chang, Y., Chen, Y., Chen, X., Zhang, H., Hua, X., Xu, M., Sheng, Y., Zhang, N., Cui, H., et al. (2024). A single-cell atlas of lung homeostasis reveals dynamic changes during development and aging. Commun Biol *7*, 1–18. https://doi.org/10.1038/s42003-024-06111-x.

13. Chang, C.-Y., Armstrong, D., Corry, D.B., and Kheradmand, F. (2023). Alveolar macrophages in lung cancer: opportunities and challenges. Front Immunol *14*, 1268939. https://doi.org/10.3389/fimmu.2023.1268939.

14. Salcher, S., Sturm, G., Horvath, L., Untergasser, G., Kuempers, C., Fotakis, G., Panizzolo, E., Martowicz, A., Trebo, M., Pall, G., et al. (2022). High-resolution single-cell atlas reveals diversity and plasticity of tissue-resident neutrophils in non-small cell lung cancer. Cancer Cell *40*, 1503-1520.e8. https://doi.org/10.1016/j.ccell.2022.10.008.

15. Casanova-Acebes, M., Dalla, E., Leader, A.M., LeBerichel, J., Nikolic, J., Morales, B.M., Brown, M., Chang, C., Troncoso, L., Chen, S.T., et al. (2021). Tissue-resident macrophages provide a pro-tumorigenic niche to early NSCLC cells. Nature *595*, 578–584. https://doi.org/10.1038/s41586-021-03651-8.

16. Marceaux, C., Weeden, C.E., Gordon, C.L., and Asselin-Labat, M.-L. (2021). Holding our breath: the promise of tissue-resident memory T cells in lung cancer. Transl Lung Cancer Res *10*, 2819–2829. https://doi.org/10.21037/tlcr-20-819.

17. Weeden, C.E., Gayevskiy, V., Marceaux, C., Batey, D., Tan, T., Yokote, K., Ribera, N.T., Clatch, A., Christo, S., Teh, C.E., et al. (2023). Early immune pressure initiated by tissue-resident memory T cells sculpts tumor evolution in non-small cell lung cancer. Cancer Cell *41*, 837-852.e6. https://doi.org/10.1016/j.ccell.2023.03.019.

18. Murgaski, A., Kiss, M., Van Damme, H., Kancheva, D., Vanmeerbeek, I., Keirsse, J., Hadadi, E., Brughmans, J., Arnouk, S.M., Hamouda, A.E.I., et al. (2022). Efficacy of CD40 Agonists Is Mediated by Distinct cDC Subsets and Subverted by Suppressive Macrophages. Cancer Research *82*, 3785–3801. https://doi.org/10.1158/0008-5472.CAN-22-0094.

19. Chalmers, Z.R., Connelly, C.F., Fabrizio, D., Gay, L., Ali, S.M., Ennis, R., Schrock, A., Campbell, B., Shlien, A., Chmielecki, J., et al. (2017). Analysis of 100,000 human cancer genomes reveals the landscape of tumor mutational burden. Genome Medicine *9*, 34. https://doi.org/10.1186/s13073-017-0424-2.

20. Park, J.W., Park, J.M., Park, D.M., Kim, D.-Y., and Kim, H.K. (2016). Stem Cells Antigen-1 Enriches for a Cancer Stem Cell-Like Subpopulation in Mouse Gastric Cancer. STEM CELLS *34*, 1177–1187. https://doi.org/10.1002/stem.2329.

21. Chu, Y.W., Seftor, E.A., Romer, L.H., and Hendrix, M.J. (1996). Experimental coexpression of vimentin and keratin intermediate filaments in human melanoma cells augments motility. Am J Pathol *148*, 63–69.

22. Han, W., Hu, C., Fan, Z.-J., and Shen, G.-L. (2021). Transcript levels of keratin 1/5/6/14/15/16/17 as potential prognostic indicators in melanoma patients. Sci Rep *11*, 1023. https://doi.org/10.1038/s41598-020-80336-8.

23. Curtis, S.J., Sinkevicius, K.W., Li, D., Lau, A.N., Roach, R.R., Zamponi, R., Woolfenden, A.E., Kirsch, D.G., Wong, K.-K., and Kim, C.F. (2010). Primary tumor genotype is an important determinant in identification of lung cancer propagating cells. Cell Stem Cell *7*, 127–133. https://doi.org/10.1016/j.stem.2010.05.021.

24. Barletta, K.E., Cagnina, R.E., Wallace, K.L., Ramos, S.I., Mehrad, B., and Linden, J. (2012). Leukocyte compartments in the mouse lung: Distinguishing between marginated, interstitial, and alveolar cells in response to injury. Journal of Immunological Methods *375*, 100–110. https://doi.org/10.1016/j.jim.2011.09.013.

25. Patel, B.V., Tatham, K.C., Wilson, M.R., O'Dea, K.P., and Takata, M. (2015). In vivo compartmental analysis of leukocytes in mouse lungs. Am J Physiol Lung Cell Mol Physiol *309*, L639–L652. https://doi.org/10.1152/ajplung.00140.2015.

26. Stoeckius, M., Zheng, S., Houck-Loomis, B., Hao, S., Yeung, B.Z., Mauck, W.M., Smibert, P., and Satija, R. (2018). Cell Hashing with barcoded antibodies enables multiplexing and doublet detection for single cell genomics. Genome Biology *19*, 224. https://doi.org/10.1186/s13059-018-1603-1.

27. McGinnis, C.S., Patterson, D.M., Winkler, J., Conrad, D.N., Hein, M.Y., Srivastava, V., Hu, J.L., Murrow, L.M., Weissman, J.S., Werb, Z., et al. (2019). MULTI-seq: sample multiplexing for single-cell RNA sequencing using lipid-tagged indices. Nat Methods *16*, 619–626. https://doi.org/10.1038/s41592-019-0433-8.

28. Zhu, Q., Conrad, D.N., and Gartner, Z.J. (2024). deMULTIplex2: robust sample demultiplexing for scRNA-seq. Genome Biol *25*, 37. https://doi.org/10.1186/s13059-024-03177-y.

29. Gao, Y., Li, J., Cheng, W., Diao, T., Liu, H., Bo, Y., Liu, C., Zhou, W., Chen, M., Zhang, Y., et al. (2024). Cross-tissue human fibroblast atlas reveals myofibroblast subtypes with distinct roles in immune modulation. Cancer Cell *42*, 1764-1783.e10. https://doi.org/10.1016/j.ccell.2024.08.020.

30. Krishnamurty, A.T., Shyer, J.A., Thai, M., Gandham, V., Buechler, M.B., Yang, Y.A., Pradhan, R.N., Wang, A.W., Sanchez, P.L., Qu, Y., et al. (2022). LRRC15+ myofibroblasts dictate the stromal setpoint to suppress tumour immunity. Nature *611*, 148–154. https://doi.org/10.1038/s41586-022-05272-1.

31. Tian, B., Chen, X., Zhang, H., Li, X., Wang, J., Han, W., Zhang, L.-Y., Fu, L., Li, Y., Nie, C., et al. (2017). Urokinase plasminogen activator secreted by cancer-associated fibroblasts induces tumor progression via PI3K/AKT and ERK signaling in esophageal squamous cell carcinoma. Oncotarget *8*, 42300–42313. https://doi.org/10.18632/oncotarget.15857.

32. Li, C., Lv, J., Wumaier, G., Zhao, Y., Dong, L., Zeng, Y., Zhu, N., Zhang, X., Wang, J., Xia, J., et al. (2023). NDRG1 promotes endothelial dysfunction and hypoxia-induced pulmonary hypertension by targeting TAF15. Precision Clinical Medicine *6*, pbad024. https://doi.org/10.1093/pcmedi/pbad024.

33. Crinier, A., Milpied, P., Escalière, B., Piperoglou, C., Galluso, J., Balsamo, A., Spinelli, L., Cervera-Marzal, I., Ebbo, M., Girard-Madoux, M., et al. (2018). High-Dimensional Single-Cell Analysis Identifies Organ-Specific Signatures and Conserved NK Cell Subsets in Humans and Mice. Immunity *49*, 971-986.e5. https://doi.org/10.1016/j.immuni.2018.09.009.

34. Chiossone, L., Chaix, J., Fuseri, N., Roth, C., Vivier, E., and Walzer, T. (2009). Maturation of mouse NK cells is a 4-stage developmental program. Blood *113*, 5488–5496. https://doi.org/10.1182/blood-2008-10-187179.

35. Dean, I., Lee, C.Y.C., Tuong, Z.K., Li, Z., Tibbitt, C.A., Willis, C., Gaspal, F., Kennedy, B.C., Matei-Rascu, V., Fiancette, R., et al. (2024). Rapid functional impairment of natural killer cells following tumor entry limits anti-tumor immunity. Nat Commun *15*, 683. https://doi.org/10.1038/s41467-024-44789-z.

36. Vivier, E., Artis, D., Colonna, M., Diefenbach, A., Di Santo, J.P., Eberl, G., Koyasu, S., Locksley, R.M., McKenzie, A.N.J., Mebius, R.E., et al. (2018). Innate Lymphoid Cells: 10 Years On. Cell *174*, 1054–1066. https://doi.org/10.1016/j.cell.2018.07.017.

37. Chandra, S., Ascui, G., Riffelmacher, T., Chawla, A., Ramírez-Suástegui, C., Castelan, V.C., Seumois, G., Simon, H., Murray, M.P., Seo, G.-Y., et al. (2023). Transcriptomes and metabolism define mouse and human MAIT cell populations. Sci Immunol *8*, eabn8531. https://doi.org/10.1126/sciimmunol.abn8531.

38. Lee, M., Lee, E., Han, S.K., Choi, Y.H., Kwon, D., Choi, H., Lee, K., Park, E.S., Rha, M.-S., Joo, D.J., et al. (2020). Single-cell RNA sequencing identifies shared differentiation paths of mouse thymic innate T cells. Nat Commun *11*, 4367. https://doi.org/10.1038/s41467-020-18155-8.

39. Szremska, A.P., Kenner, L., Weisz, E., Ott, R.G., Passegué, E., Artwohl, M., Freissmuth, M., Stoxreiter, R., Theussl, H.-C., Parzer, S.B., et al. (2003). JunB inhibits proliferation and transformation in B-lymphoid cells. Blood *102*, 4159–4165. https://doi.org/10.1182/blood-2003-03-0915.

40. Blonska, M., Zhu, Y., Chuang, H.H., You, M.J., Kunkalla, K., Vega, F., and Lin, X. (2014). Jun-regulated genes promote interaction of diffuse large B-cell lymphoma with the microenvironment. Blood *125*, 981. https://doi.org/10.1182/blood-2014-04-568188.

41. Zhang, T., Sun, J., Cheng, J., Yin, W., Li, J., Miller, H., Herrada, A.A., Gu, H., Song, H., Chen, Y., et al. (2021). The role of ubiquitinase in B cell development and function. Journal of Leukocyte Biology *109*, 395–405. https://doi.org/10.1002/JLB.1MR0720-185RR.

42. Mlynarczyk, C., Teater, M., Pae, J., Chin, C.R., Wang, L., Arulraj, T., Barisic, D., Papin, A., Hoehn, K.B., Kots, E., et al. (2023). BTG1 mutation yields supercompetitive B cells primed for malignant transformation. Science *379*, eabj7412. https://doi.org/10.1126/science.abj7412.

43. Grötsch, B., Brachs, S., Lang, C., Luther, J., Derer, A., Schlötzer-Schrehardt, U., Bozec, A., Fillatreau, S., Berberich, I., Hobeika, E., et al. (2014). The AP-1 transcription factor Fra1 inhibits follicular B cell differentiation into plasma cells. Journal of Experimental Medicine *211*, 2199–2212. https://doi.org/10.1084/jem.20130795.

44. Wittner, J., and Schuh, W. (2023). Krüppel-like factor 2: a central regulator of B cell differentiation and plasma cell homing. Front. Immunol. *14*. https://doi.org/10.3389/fimmu.2023.1172641.

45. Dennig, D., Lacerda, J., Yan, Y., Gasparetto, C., and O'Reilly, R.J. (1994). ICAM-1 (CD54) Expression on B Lymphocytes Is Associated with Their Costimulatory Function and Can Be Increased by Coactivation with IL-1 and IL-7. Cellular Immunology *156*, 414–423. https://doi.org/10.1006/cimm.1994.1186.

46. Zaretsky, I., Atrakchi, O., Mazor, R.D., Stoler-Barak, L., Biram, A., Feigelson, S.W., Gitlin, A.D., Engelhardt, B., and Shulman, Z. (2017). ICAMs support B cell interactions with T follicular helper cells and promote clonal selection. Journal of Experimental Medicine *214*, 3435–3448. https://doi.org/10.1084/jem.20171129.

47. Luo, Y., Wang, J., Li, K., Li, M., Xu, S., Liu, X., Zhang, Z., Xu, X., Zhang, Y., Pan, J., et al. (2022). Single-cell genomics identifies distinct B1 cell developmental pathways and reveals aging-related changes in the B-cell receptor repertoire. Cell & Bioscience *12*, 57. https://doi.org/10.1186/s13578-022-00795-6.

48. Sorrentino, R., Terlizzi, M., Di Crescenzo, V.G., Popolo, A., Pecoraro, M., Perillo, G., Galderisi, A., and Pinto, A. (2015). Human Lung Cancer–Derived Immunosuppressive Plasmacytoid Dendritic Cells Release IL-1α in an AIM2 Inflammasome-Dependent Manner. The American Journal of Pathology *185*, 3115–3124. https://doi.org/10.1016/j.ajpath.2015.07.009.

49. Karrich, J.J., Romera-Hernández, M., Papazian, N., Veenbergen, S., Cornelissen, F., Aparicio-Domingo, P., Stenhouse, F.H., Peddie, C.D., Hoogenboezem, R.M., Hollander, C.W.J. den, et al. (2018). Expression of Plet1 controls interstitial migration of murine small intestinal dendritic cells. European Journal of Immunology *49*, 290. https://doi.org/10.1002/eji.201847671.

50. Ramessur, A., Ambasager, B., Valle Aramburu, I., Peakman, F., Gleason, K., Lehmann, C., Papayannopoulos, V., Coombes, R.C., and Malanchi, I. (2023). Circulating neutrophils from patients

with early breast cancer have distinct subtype-dependent phenotypes. Breast Cancer Research *25*, 125. https://doi.org/10.1186/s13058-023-01707-3.

51. Casbon, A.-J., Reynaud, D., Park, C., Khuc, E., Gan, D.D., Schepers, K., Passegué, E., and Werb, Z. (2015). Invasive breast cancer reprograms early myeloid differentiation in the bone marrow to generate immunosuppressive neutrophils. Proceedings of the National Academy of Sciences *112*, E566–E575. https://doi.org/10.1073/pnas.1424927112.

52. Gabrilovich, D.I., Ostrand-Rosenberg, S., and Bronte, V. (2012). Coordinated regulation of myeloid cells by tumours. Nat Rev Immunol *12*, 253–268. https://doi.org/10.1038/nri3175.

53. Wellenstein, M.D., Coffelt, S.B., Duits, D.E.M., van Miltenburg, M.H., Slagter, M., de Rink, I., Henneman, L., Kas, S.M., Prekovic, S., Hau, C.-S., et al. (2019). Loss of p53 triggers WNT-dependent systemic inflammation to drive breast cancer metastasis. Nature *572*, 538–542. https://doi.org/10.1038/s41586-019-1450-6.

54. Mitchell, K.G., Diao, L., Karpinets, T., Negrao, M.V., Tran, H.T., Parra, E.R., Corsini, E.M., Reuben, A., Federico, L., Bernatchez, C., et al. (2020). Neutrophil expansion defines an immunoinhibitory peripheral and intratumoral inflammatory milieu in resected non-small cell lung cancer: a descriptive analysis of a prospectively immunoprofiled cohort. J Immunother Cancer *8*, e000405. https://doi.org/10.1136/jitc-2019-000405.

55. Bodac, A., Mayet, A., Rana, S., Pascual, J., Bowler, A.D., Roh, V., Fournier, N., Craciun, L., Demetter, P., Radtke, F., et al. (2023). Bcl-xL targeting eliminates ageing tumor-promoting neutrophils and inhibits lung tumor growth. EMBO Molecular Medicine *16*, 158. https://doi.org/10.1038/s44321-023-00013-x.

56. Pfirschke, C., Engblom, C., Gungabeesoon, J., Lin, Y., Rickelt, S., Zilionis, R., Messemaker, M., Siwicki, M., Gerhard, G.M., Kohl, A., et al. (2020). Tumor-Promoting Ly-6G+ SiglecFhigh Cells Are Mature and Long-Lived Neutrophils. Cell Reports *32*, 108164. https://doi.org/10.1016/j.celrep.2020.108164.

57. Grieshaber-Bouyer, R., Radtke, F.A., Cunin, P., Stifano, G., Levescot, A., Vijaykumar, B., Nelson-Maney, N., Blaustein, R.B., Monach, P.A., and Nigrovic, P.A. (2021). The neutrotime transcriptional signature defines a single continuum of neutrophils across biological compartments. Nat Commun *12*, 2856. https://doi.org/10.1038/s41467-021-22973-9.

58. Chakarov, S., Lim, H.Y., Tan, L., Lim, S.Y., See, P., Lum, J., Zhang, X.-M., Foo, S., Nakamizo, S., Duan, K., et al. (2019). Two distinct interstitial macrophage populations coexist across tissues in specific subtissular niches. Science *363*, eaau0964. https://doi.org/10.1126/science.aau0964.

59. Rizzo, G., Gropper, J., Piollet, M., Vafadarnejad, E., Rizakou, A., Bandi, S.R., Arampatzi, P., Krammer, T., DiFabion, N., Dietrich, O., et al. (2023). Dynamics of monocyte-derived macrophage diversity in experimental myocardial infarction. Cardiovascular Research *119*, 772–785. https://doi.org/10.1093/cvr/cvac113.

60. Guimarães, G.R., Maklouf, G.R., Teixeira, C.E., de Oliveira Santos, L., Tessarollo, N.G., de Toledo, N.E., Serain, A.F., de Lanna, C.A., Pretti, M.A., da Cruz, J.G.V., et al. (2024). Single-cell resolution characterization of myeloid-derived cell states with implication in cancer outcome. Nat Commun *15*, 5694. https://doi.org/10.1038/s41467-024-49916-4.

61. Sikkema, L., Ramírez-Suástegui, C., Strobl, D.C., Gillett, T.E., Zappia, L., Madissoon, E., Markov, N.S., Zaragosi, L.-E., Ji, Y., Ansari, M., et al. (2023). An integrated cell atlas of the lung in health and disease. Nat Med *29*, 1563–1577. https://doi.org/10.1038/s41591-023-02327-2.

62. Madissoon, E., Wilbrey-Clark, A., Miragaia, R.J., Saeb-Parsy, K., Mahbubani, K.T., Georgakopoulos, N., Harding, P., Polanski, K., Huang, N., Nowicki-Osuch, K., et al. (2019). scRNA-seq assessment of the human lung, spleen, and esophagus tissue stability after cold preservation. Genome Biology *21*, 1. https://doi.org/10.1186/s13059-019-1906-x.

63. Loyher, P.-L., Hamon, P., Laviron, M., Meghraoui-Kheddar, A., Goncalves, E., Deng, Z., Torstensson, S., Bercovici, N., Baudesson de Chanville, C., Combadière, B., et al. (2018). Macrophages of distinct origins contribute to tumor development in the lung. Journal of Experimental Medicine *215*, 2536–2553. https://doi.org/10.1084/jem.20180534.

64. Ikeda, N., Kubota, H., Suzuki, R., Morita, M., Yoshimura, A., Osada, Y., Kishida, K., Kitamura, D., Iwata, A., Yotsumoto, S., et al. (2023). The early neutrophil-committed progenitors aberrantly differentiate into immunoregulatory monocytes during emergency myelopoiesis. Cell Reports *42*, 112165. https://doi.org/10.1016/j.celrep.2023.112165.

65. Gudenschwager Basso, E.K., Ju, J., Soliman, E., de Jager, C., Wei, X., Pridham, K.J., Olsen, M.L., and Theus, M.H. (2024). Immunoregulatory and neutrophil-like monocyte subsets with distinct single-cell transcriptomic signatures emerge following brain injury. Journal of Neuroinflammation *21*, 41. https://doi.org/10.1186/s12974-024-03032-8.

66. Yáñez, A., Coetzee, S.G., Olsson, A., Muench, D.E., Berman, B.P., Hazelett, D.J., Salomonis, N., Grimes, H.L., and Goodridge, H.S. (2017). Granulocyte-Monocyte Progenitors and Monocyte-Dendritic Cell Progenitors Independently Produce Functionally Distinct Monocytes. Immunity *47*, 890-902.e4. https://doi.org/10.1016/j.immuni.2017.10.021.

67. Wiencke, J.K., Nissen, E., Koestler, D.C., Tamaki, S.J., Tamaki, C.M., Hansen, H.M., Warrier, G., Hadad, S., McCoy, L., Rice, T., et al. (2023). Enrichment of a neutrophil-like monocyte transcriptional state in glioblastoma myeloid suppressor cells. Research Square, rs.3.rs. https://doi.org/10.21203/rs.3.rs-3793353/v1.

68. Hayashi, Y., Kamimura-Aoyagi, Y., Nishikawa, S., Noka, R., Iwata, R., Iwabuchi, A., Watanabe, Y., Matsunuma, N., Yuki, K., Kobayashi, H., et al. (2024). IL36G-producing neutrophil-like monocytes promote cachexia in cancer. Nat Commun *15*, 7662. https://doi.org/10.1038/s41467-024-51873-x.

69. Zilionis, R., Engblom, C., Pfirschke, C., Savova, V., Zemmour, D., Saatcioglu, H.D., Krishnan, I., Maroni, G., Meyerovitz, C.V., Kerwin, C.M., et al. (2019). Single-Cell Transcriptomics of Human and Mouse Lung Cancers Reveals Conserved Myeloid Populations across Individuals and Species. Immunity *50*, 1317-1334.e10. https://doi.org/10.1016/j.immuni.2019.03.009.

70. Governa, V., de Oliveira, K.G., Bång-Rudenstam, A., Offer, S., Cerezo-Magaña, M., Li, J., Beyer, S., Johansson, M.C., Månsson, A.-S., Edvardsson, C., et al. (2024). Protumoral lipid droplet–loaded macrophages are enriched in human glioblastoma and can be therapeutically targeted. Science Translational Medicine *16*, eadk1168. https://doi.org/10.1126/scitranslmed.adk1168.

71. Masetti, M., Carriero, R., Portale, F., Marelli, G., Morina, N., Pandini, M., Iovino, M., Partini, B., Erreni, M., Ponzetta, A., et al. (2021). Lipid-loaded tumor-associated macrophages sustain tumor growth and invasiveness in prostate cancer. Journal of Experimental Medicine *219*, e20210564. https://doi.org/10.1084/jem.20210564.

72. Kloosterman, D.J., Erbani, J., Boon, M., Farber, M., Handgraaf, S.M., Ando-Kuri, M., Sánchez-López, E., Fontein, B., Mertz, M., Nieuwland, M., et al. (2024). Macrophage-mediated myelin recycling fuels brain cancer malignancy. Cell *187*, 5336-5356.e30. https://doi.org/10.1016/j.cell.2024.07.030.

73. Timperi, E., Gueguen, P., Molgora, M., Magagna, I., Kieffer, Y., Lopez-Lastra, S., Sirven, P., Baudrin, L.G., Baulande, S., Nicolas, A., et al. (2022). Lipid-Associated Macrophages Are Induced by Cancer-

Associated Fibroblasts and Mediate Immune Suppression in Breast Cancer. Cancer Res *82*, 3291–3306. https://doi.org/10.1158/0008-5472.CAN-22-1427.

74. Daveri, E., Vergani, B., Lalli, L., Ferrero, G., Casiraghi, E., Cova, A., Zorza, M., Huber, V., Gariboldi, M., Pasanisi, P., et al. (2024). Cancer-associated foam cells hamper protective T cell immunity and favor tumor progression in human colon carcinogenesis. Journal for Immunotherapy of Cancer *12*, e009720. https://doi.org/10.1136/jitc-2024-009720.

75. Huggins, D.N., LaRue, R.S., Wang, Y., Knutson, T.P., Xu, Y., Williams, J.W., and Schwertfeger, K.L. (2021). Characterizing Macrophage Diversity in Metastasis-Bearing Lungs Reveals a Lipid-Associated Macrophage Subset. Cancer Research *81*, 5284–5295. https://doi.org/10.1158/0008-5472.CAN-21-0101.

76. Li, Y.-S., Lai, W.-P., Yin, K., Zheng, M.-M., Tu, H.-Y., Guo, W.-B., Li, L., Lin, S.-H., Wang, Z., Zeng, L., et al. (2024). Lipid-associated macrophages for osimertinib resistance and leptomeningeal metastases in NSCLC. Cell Reports *43*. https://doi.org/10.1016/j.celrep.2024.114613.

77. Jaitin, D.A., Adlung, L., Thaiss, C.A., Weiner, A., Li, B., Descamps, H., Lundgren, P., Bleriot, C., Liu, Z., Deczkowska, A., et al. (2019). Lipid-Associated Macrophages Control Metabolic Homeostasis in a Trem2-Dependent Manner. Cell *178*, 686-698.e14. https://doi.org/10.1016/j.cell.2019.05.054.

78. Remmerie, A., and Scott, C.L. (2018). Macrophages and lipid metabolism. Cellular Immunology *330*, 27–42. https://doi.org/10.1016/j.cellimm.2018.01.020.

79. Ramos, R.N., Missolo-Koussou, Y., Gerber-Ferder, Y., Bromley, C.P., Bugatti, M., Núñez, N.G., Boari, J.T., Richer, W., Menger, L., Denizeau, J., et al. (2022). Tissue-resident FOLR2+ macrophages associate with CD8+ T cell infiltration in human breast cancer. Cell *185*, 1189-1207.e25. https://doi.org/10.1016/j.cell.2022.02.021.

80. Bernstein, M.N., Scott, D., Hession, C.C., Nieuwenhuis, T., Gerritsen, J., Tabrizi, S., Nandivada, V., Huggins, M.A., Duan, M., Malu, S., et al. (2023). Monkeybread: A Python toolkit for the analysis of cellular niches in single-cell resolution spatial transcriptomics data. Preprint at bioRxiv, https://doi.org/10.1101/2023.09.14.557736 https://doi.org/10.1101/2023.09.14.557736.

81. Di Pilato, M., Kfuri-Rubens, R., Pruessmann, J.N., Ozga, A.J., Messemaker, M., Cadilha, B.L., Sivakumar, R., Cianciaruso, C., Warner, R.D., Marangoni, F., et al. (2021). CXCR6 positions cytotoxic T cells to receive critical survival signals in the tumor microenvironment. Cell *184*, 4512-4530.e22. https://doi.org/10.1016/j.cell.2021.07.015.

82. Lee, C.Y.C., Kennedy, B.C., Richoz, N., Dean, I., Tuong, Z.K., Gaspal, F., Li, Z., Willis, C., Hasegawa, T., Whiteside, S.K., et al. (2024). Tumour-retained activated CCR7+ dendritic cells are heterogeneous and regulate local anti-tumour cytolytic activity. Nat Commun *15*, 682. https://doi.org/10.1038/s41467-024-44787-1.

83. Houda, I., Dickhoff, C., Uyl-de Groot, C.A., Reguart, N., Provencio, M., Levy, A., Dziadziuszko, R., Pompili, C., Di Maio, M., Thomas, M., et al. (2024). New systemic treatment paradigms in resectable non-small cell lung cancer and variations in patient access across Europe. Lancet Reg Health Eur *38*, 100840. https://doi.org/10.1016/j.lanepe.2024.100840.

84. Wang, C., Zeng, Q., Gül, Z.M., Wang, S., Pick, R., Cheng, P., Bill, R., Wu, Y., Naulaerts, S., Barnoud, C., et al. (2024). Circadian tumor infiltration and function of CD8(+) T cells dictate immunotherapy efficacy. Cell *187*, 2690-2702.e17. https://doi.org/10.1016/j.cell.2024.04.015.

85. Hektoen, H.H., Tsuruda, K.M., Brustugun, O.T., Neumann, K., and Andreassen, B.K. (2025). Real-world comparison of pembrolizumab alone and combined with chemotherapy in metastatic lung

adenocarcinoma patients with PD-L1 expression ≥50%. ESMO Open *10*. https://doi.org/10.1016/j.esmoop.2025.105073.

86. Gandhi, L., Rodríguez-Abreu, D., Gadgeel, S., Esteban, E., Felip, E., De Angelis, F., Domine, M., Clingan, P., Hochmair, M.J., Powell, S.F., et al. (2018). Pembrolizumab plus Chemotherapy in Metastatic Non-Small-Cell Lung Cancer. N Engl J Med *378*, 2078–2092. https://doi.org/10.1056/NEJMoa1801005.

87. Martinez-Usatorre, A., Kadioglu, E., Boivin, G., Cianciaruso, C., Guichard, A., Torchia, B., Zangger, N., Nassiri, S., Keklikoglou, I., Schmittnaegel, M., et al. (2021). Overcoming microenvironmental resistance to PD-1 blockade in genetically engineered lung cancer models. Science translational medicine *13*. https://doi.org/10.1126/scitranslmed.abd1616.

88. Chow, A., Uddin, F.Z., Liu, M., Dobrin, A., Nabet, B.Y., Mangarin, L., Lavin, Y., Rizvi, H., Tischfield, S.E., Quintanal-Villalonga, A., et al. (2023). The ectonucleotidase CD39 identifies tumor-reactive CD8(+) T cells predictive of immune checkpoint blockade efficacy in human lung cancer. Immunity *56*, 93-106.e6. https://doi.org/10.1016/j.immuni.2022.12.001.

89. Berckmans, Y., Ceusters, J., Vankerckhoven, A., Wouters, R., Riva, M., and Coosemans, A. (2023). Preclinical studies performed in appropriate models could help identify optimal timing of combined chemotherapy and immunotherapy. Front Immunol *14*, 1236965. https://doi.org/10.3389/fimmu.2023.1236965.

90. Emens, L.A., Romero, P.J., Anderson, A.C., Bruno, T.C., Capitini, C.M., Collyar, D., Gulley, J.L., Hwu, P., Posey, A.D., Silk, A.W., et al. (2024). Challenges and opportunities in cancer immunotherapy: a Society for Immunotherapy of Cancer (SITC) strategic vision. J Immunother Cancer *12*, e009063. https://doi.org/10.1136/jitc-2024-009063.

91. Scheff, N.N., Bhattacharya, A., Dowse, E., Dang, R.X., Dolan, J.C., Wang, S., Kim, H., Albertson, D.G., and Schmidt, B.L. (2018). Neutrophil-Mediated Endogenous Analgesia Contributes to Sex Differences in Oral Cancer Pain. Front Integr Neurosci *12*, 52. https://doi.org/10.3389/fnint.2018.00052.

92. Tang, J.-J., Pan, Y.-F., Chen, C., Cui, X.-L., Yan, Z.-J., Zhou, D.-X., Guo, L.-N., Cao, D., Yu, L.-X., and Wang, H.-Y. (2022). Androgens drive sexual dimorphism in liver metastasis by promoting hepatic accumulation of neutrophils. Cell Rep *39*, 110987. https://doi.org/10.1016/j.celrep.2022.110987.

93. Lao, J., Xu, H., Liang, Z., Luo, C., Shu, L., Xie, Y., Wu, Y., Hao, Y., and Yuan, Y. (2023). Peripheral changes in T cells predict efficacy of anti-PD-1 immunotherapy in non-small cell lung cancer. Immunobiology *228*, 152391. https://doi.org/10.1016/j.imbio.2023.152391.

94. Martini, E., Kunderfranco, P., Peano, C., Carullo, P., Cremonesi, M., Schorn, T., Carriero, R., Termanini, A., Colombo, F.S., Jachetti, E., et al. (2019). Single-Cell Sequencing of Mouse Heart Immune Infiltrate in Pressure Overload–Driven Heart Failure Reveals Extent of Immune Activation. Circulation *140*, 2089–2107. https://doi.org/10.1161/CIRCULATIONAHA.119.041694.

95. Suchanek, O., Ferdinand, J.R., Tuong, Z.K., Wijeyesinghe, S., Chandra, A., Clauder, A.-K., Almeida, L.N., Clare, S., Harcourt, K., Ward, C.J., et al. (2023). Tissue-resident B cells orchestrate macrophage polarisation and function. Nat Commun *14*, 7081. https://doi.org/10.1038/s41467-023-42625-4.

96. Alisjahbana, A., Mohammad, I., Gao, Y., Evren, E., and Willinger, T. (2023). Single-cell RNA sequencing of human lung innate lymphoid cells in the vascular and tissue niche reveals molecular features of tissue adaptation. Discovery Immunology *2*, kyad007. https://doi.org/10.1093/discim/kyad007.

97. Vafadarnejad, E., Rizzo, G., Krampert, L., Arampatzi, P., Arias-Loza, A.-P., Nazzal, Y., Rizakou, A., Knochenhauer, T., Bandi, S.R., Nugroho, V.A., et al. (2020). Dynamics of Cardiac Neutrophil Diversity in Murine Myocardial Infarction. Circulation Research *127*, e232–e249. https://doi.org/10.1161/CIRCRESAHA.120.317200.

98. Van Overmeire, E., Stijlemans, B., Heymann, F., Keirsse, J., Morias, Y., Elkrim, Y., Brys, L., Abels, C., Lahmar, Q., Ergen, C., et al. (2016). M-CSF and GM-CSF Receptor Signaling Differentially Regulate Monocyte Maturation and Macrophage Polarization in the Tumor Microenvironment. Cancer Research *76*, 35–42. https://doi.org/10.1158/0008-5472.CAN-15-0869.

99. Ng, M.S.F., Kwok, I., Tan, L., Shi, C., Cerezo-Wallis, D., Tan, Y., Leong, K., Calvo, G.F., Yang, K., Zhang, Y., et al. (2024). Deterministic reprogramming of neutrophils within tumors. Science *383*, eadf6493. https://doi.org/10.1126/science.adf6493.

100. Bui, T.M., Yalom, L.K., Ning, E., Urbanczyk, J.M., Ren, X., Herrnreiter, C.J., Disario, J.A., Wray, B., Schipma, M.J., Velichko, Y.S., et al. (2024). Tissue-specific reprogramming leads to angiogenic neutrophil specialization and tumor vascularization in colorectal cancer. J Clin Invest *134*. https://doi.org/10.1172/JCI174545.

101. Gong, Z., Li, Q., Shi, J., Li, P., Hua, L., Shultz, L.D., and Ren, G. (2023). Immunosuppressive Reprogramming of Neutrophils by Lung Mesenchymal Cells Promotes Breast Cancer Metastasis. Sci Immunol *8*, eadd5204. https://doi.org/10.1126/sciimmunol.add5204.

102. Qian, J., Olbrecht, S., Boeckx, B., Vos, H., Laoui, D., Etlioglu, E., Wauters, E., Pomella, V., Verbandt, S., Busschaert, P., et al. (2020). A pan-cancer blueprint of the heterogeneous tumor microenvironment revealed by single-cell profiling. Cell Research *30*, 1–18. https://doi.org/10.1038/s41422-020-0355-0.

103. Kiss, M., Van Gassen, S., Movahedi, K., Saeys, Y., and Laoui, D. (2018). Myeloid cell heterogeneity in cancer: not a single cell alike. Cellular Immunology *330*, 188–201. https://doi.org/10.1016/j.cellimm.2018.02.008.

104. Pittet, M.J., Michielin, O., and Migliorini, D. (2022). Clinical relevance of tumour-associated macrophages. Nat Rev Clin Oncol *19*, 402–421. https://doi.org/10.1038/s41571-022-00620-6.

105. Movahedi, K., Laoui, D., Gysemans, C., Baeten, M., Stangé, G., Van den Bossche, J., Mack, M., Pipeleers, D., In't Veld, P., De Baetselier, P., et al. (2010). Different Tumor Microenvironments Contain Functionally Distinct Subsets of Macrophages Derived from Ly6C(high) Monocytes. Cancer Research *70*, 5728–5739. https://doi.org/10.1158/0008-5472.CAN-09-4672.

106. Luo, Q., Zheng, N., Jiang, L., Wang, T., Zhang, P., Liu, Y., Zheng, P., Wang, W., Xie, G., Chen, L., et al. (2020). Lipid accumulation in macrophages confers protumorigenic polarization and immunity in gastric cancer. Cancer Science *111*, 4000–4011. https://doi.org/10.1111/cas.14616.

107. Marelli, G., Morina, N., Portale, F., Pandini, M., Iovino, M., Di Conza, G., Ho, P.-C., and Di Mitri, D. (2022). Lipid-loaded macrophages as new therapeutic target in cancer. J Immunother Cancer *10*, e004584. https://doi.org/10.1136/jitc-2022-004584.

108. Rabold, K., Aschenbrenner, A., Thiele, C., Boahen, C.K., Schiltmans, A., Smit, J.W.A., Schultze, J.L., Netea, M.G., Adema, G.J., and Netea-Maier, R.T. (2020). Enhanced lipid biosynthesis in human tumor-induced macrophages contributes to their protumoral characteristics. J Immunother Cancer *8*, e000638. https://doi.org/10.1136/jitc-2020-000638.

109. Su, P., Wang, Q., Bi, E., Ma, X., Liu, L., Yang, M., Qian, J., and Yi, Q. (2020). Enhanced Lipid Accumulation and Metabolism Are Required for the Differentiation and Activation of Tumor-Associated Macrophages. Cancer Research *80*, 1438–1450. https://doi.org/10.1158/0008-5472.CAN-19-2994.

110. Li, A.C., and Glass, C.K. (2002). The macrophage foam cell as a target for therapeutic intervention. Nat Med *8*, 1235–1242. https://doi.org/10.1038/nm1102-1235.

111. Jiang, Y., Li, Y., and Zhu, B. (2015). T-cell exhaustion in the tumor microenvironment. Cell Death Dis *6*, e1792–e1792. https://doi.org/10.1038/cddis.2015.162.

112. Iwai, Y., Terawaki, S., and Honjo, T. (2005). PD-1 blockade inhibits hematogenous spread of poorly immunogenic tumor cells by enhanced recruitment of effector T cells. International Immunology *17*, 133–144. https://doi.org/10.1093/intimm/dxh194.

113. Hodi, F.S., Mihm, M.C., Soiffer, R.J., Haluska, F.G., Butler, M., Seiden, M.V., Davis, T., Henry-Spires, R., MacRae, S., Willman, A., et al. (2003). Biologic activity of cytotoxic T lymphocyte-associated antigen 4 antibody blockade in previously vaccinated metastatic melanoma and ovarian carcinoma patients. Proc Natl Acad Sci U S A *100*, 4712–4717. https://doi.org/10.1073/pnas.0830997100.

114. Pouxvielh, K., Marotel, M., Drouillard, A., Villard, M., Moreews, M., Bossan, A., Poiget, M., Khoryati, L., Benezech, S., Fallone, L., et al. (2024). Tumor-induced natural killer cell dysfunction is a rapid and reversible process uncoupled from the expression of immune checkpoints. Science Advances *10*, eadn0164. https://doi.org/10.1126/sciadv.adn0164.

115. Li, Q., Cai, S., Li, M., Zhou, X., Wu, G., Kang, K., Yuan, J., Wang, R., Huyan, T., and Zhang, W. (2021). Natural killer cell exhaustion in lung cancer. International Immunopharmacology *96*, 107764. https://doi.org/10.1016/j.intimp.2021.107764.

116. Slattery, K., Woods, E., Zaiatz-Bittencourt, V., Marks, S., Chew, S., Conroy, M., Goggin, C., MacEochagain, C., Kennedy, J., Lucas, S., et al. (2021). TGFβ drives NK cell metabolic dysfunction in human metastatic breast cancer. J Immunother Cancer *9*, e002044. https://doi.org/10.1136/jitc-2020-002044.

117. Murgaski, A., Bardet, P.M.R., Arnouk, S.M., Clappaert, E.J., and Laoui, D. (2019). Unleashing Tumour-Dendritic Cells to Fight Cancer by Tackling Their Three A's: Abundance, Activation and Antigen-Delivery. Cancers *11*, 670. https://doi.org/10.3390/cancers11050670.

118. Wculek, S.K., Cueto, F.J., Mujal, A.M., Melero, I., Krummel, M.F., and Sancho, D. (2020). Dendritic cells in cancer immunology and immunotherapy. Nat Rev Immunol *20*, 7–24. https://doi.org/10.1038/s41577-019-0210-z.

119. López, L., Morosi, L.G., La Terza, F., Bourdely, P., Rospo, G., Amadio, R., Piperno, G.M., Russo, V., Volponi, C., Vodret, S., et al. (2024). Dendritic cell-targeted therapy expands CD8 T cell responses to bona-fide neoantigens in lung tumors. Nat Commun *15*, 2280. https://doi.org/10.1038/s41467-024-46685-y.

120. Caronni, N., Piperno, G.M., Simoncello, F., Romano, O., Vodret, S., Yanagihashi, Y., Dress, R., Dutertre, C.-A., Bugatti, M., Bourdeley, P., et al. (2021). TIM4 expression by dendritic cells mediates uptake of tumor-associated antigens and anti-tumor responses. Nat Commun *12*, 2237. https://doi.org/10.1038/s41467-021-22535-z.

121. Caronni, N., Simoncello, F., Stafetta, F., Guarnaccia, C., Ruiz-Moreno, J.S., Opitz, B., Galli, T., Proux-Gillardeaux, V., and Benvenuti, F. (2018). Downregulation of Membrane Trafficking Proteins and Lactate Conditioning Determine Loss of Dendritic Cell Function in Lung Cancer. Cancer Research *78*, 1685–1699. https://doi.org/10.1158/0008-5472.CAN-17-1307.

122. Zagorulya, M., Yim, L., Morgan, D.M., Edwards, A., Torres-Mejia, E., Momin, N., McCreery, C.V., Zamora, I.L., Horton, B.L., Fox, J.G., et al. (2023). Tissue-specific abundance of interferon-gamma

drives regulatory T cells to restrain DC1-mediated priming of cytotoxic T cells against lung cancer. Immunity *56*, 386-405.e10. https://doi.org/10.1016/j.immuni.2023.01.010.

123. Maier, B., Leader, A.M., Chen, S.T., Tung, N., Chang, C., LeBerichel, J., Chudnovskiy, A., Maskey, S., Walker, L., Finnigan, J.P., et al. (2020). A conserved dendritic-cell regulatory program limits antitumour immunity. Nature *580*, 257–262. https://doi.org/10.1038/s41586-020-2134-y.

124. Bayerl, F., Meiser, P., Donakonda, S., Hirschberger, A., Lacher, S.B., Pedde, A.-M., Hermann, C.D., Elewaut, A., Knolle, M., Ramsauer, L., et al. (2023). Tumor-derived prostaglandin E2 programs cDC1 dysfunction to impair intratumoral orchestration of anti-cancer T cell responses. Immunity *56*, 1341-1358.e11. https://doi.org/10.1016/j.immuni.2023.05.011.

125. Bosteels, C., Neyt, K., Vanheerswynghels, M., van Helden, M.J., Sichien, D., Debeuf, N., De Prijck, S., Bosteels, V., Vandamme, N., Martens, L., et al. (2020). Inflammatory Type 2 cDCs Acquire Features of cDC1s and Macrophages to Orchestrate Immunity to Respiratory Virus Infection. Immunity *52*, 1039-1056.e9. https://doi.org/10.1016/j.immuni.2020.04.005.

126. Duong, E., Fessenden, T.B., Lutz, E., Dinter, T., Yim, L., Blatt, S., Bhutkar, A., Wittrup, K.D., and Spranger, S. (2022). Type I interferon activates MHC class I-dressed CD11b+ conventional dendritic cells to promote protective anti-tumor CD8+ T cell immunity. Immunity *55*, 308-323.e9. https://doi.org/10.1016/j.immuni.2021.10.020.

127. Mattiuz, R., Brousse, C., Ambrosini, M., Cancel, J., Bessou, G., Mussard, J., Sanlaville, A., Caux, C., Bendriss-Vermare, N., Valladeau-Guilemond, J., et al. (2021). Type 1 conventional dendritic cells and interferons are required for spontaneous CD4+ and CD8+ T-cell protective responses to breast cancer. Clin Transl Immunology *10*, e1305. https://doi.org/10.1002/cti2.1305.

128. Lei, X., de Groot, D.C., Welters, M.J.P., de Wit, T., Schrama, E., van Eenennaam, H., Santegoets, S.J., Oosenbrug, T., van der Veen, A., Vos, J.L., et al. (2024). CD4+ T cells produce IFN-I to license cDC1s for induction of cytotoxic T-cell activity in human tumors. Cell Mol Immunol *21*, 374–392. https://doi.org/10.1038/s41423-024-01133-1.

129. Zheng, C., Wang, J., Zhou, Y., Duan, Y., Zheng, R., Xie, Y., Wei, X., Wu, J., Shen, H., Ye, M., et al. (2024). IFNα-induced BST2+ tumor-associated macrophages facilitate immunosuppression and tumor growth in pancreatic cancer by ERK-CXCL7 signaling. Cell Reports *43*, 114088. https://doi.org/10.1016/j.celrep.2024.114088.

130. Benguigui, M., Cooper, T.J., Kalkar, P., Schif-Zuck, S., Halaban, R., Bacchiocchi, A., Kamer, I., Deo, A., Manobla, B., Menachem, R., et al. (2024). Interferon-stimulated neutrophils as a predictor of immunotherapy response. Cancer Cell *42*, 253-265.e12. https://doi.org/10.1016/j.ccell.2023.12.005.

131. Gungabeesoon, J., Gort-Freitas, N.A., Kiss, M., Bolli, E., Messemaker, M., Siwicki, M., Hicham, M., Bill, R., Koch, P., Cianciaruso, C., et al. (2023). A neutrophil response linked to tumor control in immunotherapy. Cell *186*, 1448-1464.e20. https://doi.org/10.1016/j.cell.2023.02.032.

132. Guanizo, A.C., Luong, Q., Jayasekara, W.S.N., de Geus, E.D., Inampudi, C., Xue, V.S., Chen, J., de Weerd, N.A., Matthews, A.Y., Gantier, M.P., et al. (2024). A STAT3–STING–IFN axis controls the metastatic spread of small cell lung cancer. Nat Immunol *25*, 2259–2269. https://doi.org/10.1038/s41590-024-02014-5.

133. Ninh, V.K., Calcagno, D.M., Yu, J.D., Zhang, B., Taghdiri, N., Sehgal, R., Mesfin, J.M., Chen, C.J., Kalhor, K., Toomu, A., et al. (2024). Spatially clustered type I interferon responses at injury borderzones. Nature *633*, 174–181. https://doi.org/10.1038/s41586-024-07806-1.

134. Liu, Q., Luo, Q., Ju, Y., and Song, G. (2020). Role of the mechanical microenvironment in cancer development and progression. Cancer Biology & Medicine *17*, 282. https://doi.org/10.20892/j.issn.2095-3941.2019.0437.

135. Scheyltjens, I., Van Hove, H., De Vlaminck, K., Kancheva, D., Bastos, J., Vara-Pérez, M., Pombo Antunes, A.R., Martens, L., Scott, C.L., Van Ginderachter, J.A., et al. (2022). Single-cell RNA and protein profiling of immune cells from the mouse brain and its border tissues. Nat Protoc *17*, 2354–2388. https://doi.org/10.1038/s41596-022-00716-4.

136. Zhu, Q., Conrad, D.N., and Gartner, Z.J. (2023). deMULTIplex2: robust sample demultiplexing for scRNA-seq. bioRxiv, 2023.04.11.536275. https://doi.org/10.1101/2023.04.11.536275.

137. Tang, Z., Kang, B., Li, C., Chen, T., and Zhang, Z. (2019). GEPIA2: an enhanced web server for large-scale expression profiling and interactive analysis. Nucleic Acids Research *47*, W556–W560. https://doi.org/10.1093/nar/gkz430.

138. Kasikova, L., Rakova, J., Hensler, M., Lanickova, T., Tomankova, J., Pasulka, J., Drozenova, J., Mojzisova, K., Fialova, A., Vosahlikova, S., et al. (2024). Tertiary lymphoid structures and B cells determine clinically relevant T cell phenotypes in ovarian cancer. Nat Commun *15*, 2528. https://doi.org/10.1038/s41467-024-46873-w.

ACKNOWLEDGEMENTS

We thank Nadia Abou, Eleonora Omasta, Ellen Vaneetvelde, Maité Schuurmans and Yvon Elkrim for administrative and technical assistance. We would like to thank the VIB Nucleomics Core, the VIB Single Cell Core and VIB Flow Core for providing access to RNA sequencing technologies, their support and access to the instrument park (vib.be/core-facilities). We thank VIB Tech Watch Core for supporting access to the Vizgen technology. We thank Marnik Vuylsteke and Kurt Barbé for statistical consult. Computational resources and services used in this work were provided by the VSC (Flemish Supercomputer Center), funded by the Research Foundation - Flanders (FWO) and the Flemish Government. We would like to warmly thank Alexia, for supporting P.M.R.B during the revisions.

FUNDING STATEMENT

P.M.R.B. is supported by a predoctoral grant from FWO Vlaanderen (1154720N) and by the Award Cancer Research - Oncology Center VUB, funded by the bequests of Ms. Esther Desmedt and Ms. Irma Noë. L.A. is supported by a predoctoral grant from FWO Vlaanderen (11P1824N) and by a back-up mandate of the Research Council VUB (OZR4011). E.H. is supported by a postdoctoral grant from FWO Vlaanderen (12Y1922N). M.P. and A.V.A. are supported by predoctoral grants from FNRS. S.V., M.H. and J.F. are supported by Sotio Biotech, Prague, Czech Republic. A.A.C is supported by a predoctoral grant from FWO Vlaanderen (1169523N) and an Emmanuel Van der Schueren Grant of Kom op tegen Kanker. S.D. is supported by a postdoctoral grant from Stichting tegen kanker (2021-023). E.M. is supported by Kom op tegen Kanker and the VUB Leerstoel Alex Agnew. A.E.I.H. is supported by a postdoctoral grant from FWO Vlaanderen (1267925N). P.C. is a FNRS Senior Research Associate. F.A.N. is supported by the Fonds de la Recherche Scientifique FNRS (Belgium) Grants and Fellowships. D.L is supported by grants from FWO, Kom op tegen Kanker, Stichting tegen kanker, VIB and Vrije Universiteit Brussel. This article was published with the support of the University Foundation of Belgium.

AUTHOR CONTRIBUTIONS

Conceptualisation: P.M.R.B., L.A., E.H., D.L.
Investigation: P.M.R.B., L.A., E.H., M.P., S.V., A.A.C., A.V.A., A.D., R.R., M.H., G.M.C., E.M., A.E.I.H.
Formal analysis: P.M.R.B., L.A., E.H., D.K., M.P., M.H., D.H.
Visualisation: D.K., K.V.
Provision of antibodies or samples: L.B., A.B.
Intellectual input: S.D., J.P.B, J.F, P.C., F.A.N
Funding acquisition: G.R., S.D., F.A.N., D.L.
Writing - original draft: P.M.R.B., L.A., D.L.
Writing – review & editing: P.M.R.B., L.A., E.H., D.L., E.M., A.A.C., A.E.I.H., J.F., P.C., F.A.N.

Supervision: D.L.

COMPETING INTERESTS STATEMENT

The authors declare no potential conflicts of interest.

FIGURE LEGENDS/CAPTIONS

Fig. 1: Introducing a dissectible LLC-derived orthotopic mouse model. (A) UMAP of immune cells (479,493 cells from 106 patients) from primary LUAD tumours and adjacent tissue. Data subsetted and reanalysed from Salcher *et al.*, 2022[14]. Human icon created in BioRender. Laoui, D. (2026) https://BioRender.com/61mtp59. **(B)** UMAP of immune cells (15,544 cells) from murine subcutaneous LLC tumours. Data subsetted and reanalysed from Murgaski *et al.*, 2022[18]. Mouse icon created in BioRender. Laoui, D. (2026) https://BioRender.com/vsy9o7g. **(C)** Percentages of main immune subsets in primary LUAD tumour and adjacent tissue (left) and in murine subcutaneous LLC tumours (right). **(D)** Blobbogram showing the differential abundance of general immune cell types in primary LUAD tumour (n=104) and paired adjacent (n=59) samples, irrespective of their location. P-values and confidence intervals were estimated using a generalized linear mixed-effects model (GLMM) as described in the Methods. Human icon created in BioRender. Laoui, D. (2026) https://BioRender.com/61mtp59. **(E)** Different investigated lung cancer inoculation methods. Created in BioRender. Laoui, D. (2026) https://BioRender.com/lsuihxr. **(F)** Schematic overview of the generation of the P2 cell line through *in vivo* passaging. Created in BioRender. Laoui, D. (2026) https://BioRender.com/8mdwntc. **(G)** ORTHO lungs inoculated with P0 (left) or P2 (right) at 21 dpi. **(H)** UMAP of P0 (2,469 cells) and P2 cell lines, with P2 displaying Ly6a$^+$ (983 cells) and Ly6a$^-$ (2,490 cells) states. **(C-D)** Source data are provided as a Source Data file.

Fig. 2: Characterisation of the immune compartment of orthotopic and subcutaneous tumours via SEPARATE-Seq and flow cytometry. (A) Schematic overview of SEPARATE-Seq combined with flow cytometry (FLOW) on P2 SUBCUT and ORTHO-T/-A/-M. Created in BioRender. Laoui, D. (2026) https://BioRender.com/d09c7zk. **(B)** UMAP of all immune cells (49,826 cells) from SUBCUT and ORTHO-T/-A/-M (n=4 for each sample type). **(C)** General immune cell composition of each sample type split based on intratissue/vascular origin. Data based on SEPARATE-Seq analysis of P2 SUBCUT and ORTHO-T/-A/-M (n=4 for each sample type). Bar charts illustrate the cell composition as percentage within total sample type. Data averaged over n=4 and rescaled to a total of 100% per sample type. Corresponding UMAPs shown above/below the bar charts. **(D)** Percentage of intratissue or vascular immune cells as determined by SEPARATE-Seq (left, data derived from 2B) or flow cytometry (right). AMs were analysed separately due to their intrinsic autofluorescence. **(E)** Blobbograms showing the differential abundance of general immune cell types in ORTHO-T (n=4) vs SUBCUT (n=4), ORTHO-T (n=4) vs ORTHO-A (n=4), ORTHO-A (n=4) vs ORTHO-M (n=4), irrespective of their location. Data shown as log of rate ratio with 95% confidence

interval. P-values (< 0.05 in bold) are reported for each individual cell type in the blobbogram. P-values and confidence intervals were estimated using a generalized linear mixed-effects model (GLMM) as described in the Methods. **(C-E)** Source data are provided as a Source Data file.

Fig. 3: Comparing the immune composition of lung cancer using SEPARATE-Seq and spatial transcriptomics. (A) Overview of our spatial transcriptomics analysis pipeline. All detected transcripts on a DAPI-stained tissue section (Vizgen slide 1 (VIZ1) and Vizgen slide 2 (VIZ2)) of tumour-bearing lungs (left) and delineation of tumour nodules (T) and adjacent (A) tissue (right). Bar charts showing the percentage of immune, non-immune and unidentified cells from VIZ1 (top) and VIZ2 (bottom). UMAP of all immune cells (15,580 cells) in tumour-bearing lungs identified in VIZ1. Spatial lay-out of main cell clusters in VIZ1 and VIZ2. VIZ1 and VIZ2 are derived from 2 different murine tumour-bearing lungs (n=2). Mouse and lung icons created in BioRender. Laoui, D. (2026) https://BioRender.com/whcotzr. **(B)** Percentage of each general immune cell type in tumour and adjacent tissue determined via spatial transcriptomics (left, VIZ1) or SEPARATE-Seq (right, data from Fig. 2B). **(A-B)** Source data are provided as a Source Data file.

Fig. 4: Comparing the detailed immune composition of LUAD patient tumour and adjacent samples using scRNA-Seq. (A) Percentages of the different human lymphoid subsets (subclustered from Fig. 1A). Shown within total lymphoid cells in primary LUAD tumour or adjacent tissue. Percentages normalised per patient. **(B)** Percentages of the different human myeloid subsets (subclustered from Fig. 1A). Shown within total myeloid cells in primary LUAD tumour or adjacent tissue. Percentages normalised per patient. **(C)** Blobbogram showing the differential abundance of immune cell subtypes across paired tumour and adjacent tissue (n=4). Data shown as log of rate ratio with 95% confidence interval. Adjusted p-values (< 0.05 in bold) are reported for each individual cell type in the blobbogram (Bonferroni correction). P-values and confidence intervals were estimated using a generalized linear mixed-effects model (GLMM) as described in the Methods. **(A-C)** Source data are provided as a Source Data file. **(A-C)** Human icon created in BioRender. Laoui, D. (2026) https://BioRender.com/61mtp59.

Fig. 5: In tumours, T and NK cells adopt distinct phenotypes versus adjacent tissue. (A) UMAP of T cell, NK-cell and ILC subsets (subclustered from Fig. 2B) from SUBCUT and ORTHO-T/-A/-M. **(B)** UMAP of T cell, NK-cell and ILC subsets split across different sample types and their intratissue/vascular origin. Bar charts illustrate the cell composition as percentage within T/NK/ILC subset per sample type. Data averaged over n=4 and rescaled to a total of 100% per sample type. Corresponding UMAPs shown above/below the bar charts. **(C)** Spatial distribution of T cell, NK-cell and ILC subsets in VIZ1 (left). Density plot of each subset in function of distance to the tumour core. Bar chart showing the percentage of each subset within total T-, NK and ILC cells split across tumour or adjacent tissue (2,122 and 1,129 cells resp.; right). **(B-C)** Source data are provided as a Source Data file.

Fig. 6: Plasma cells are preferentially enriched in tumour tissue. (A) UMAP of B-cell subsets (subclustered from Fig. 2B) from SUBCUT and ORTHO-T/-A/-M. **(B)** UMAP of B-cell subsets split across different sample types and their intratissue/vascular origin. Bar charts illustrate the cell composition as

percentage within B-cell subset per sample type. Data averaged over n=4 and rescaled to a total of 100% per sample type. **(C)** Spatial distribution of B-cell subsets in VIZ1 (top). Density plot of each subset in function of distance to the tumour core (bottom). Bar chart showing the percentage of each subset within total B cells split across tumour or adjacent tissue (872 and 1,452 cells resp.; right). **(D)** Immunofluorescence of CD4, CD8, CD20, and PanCK staining on ORTHO lung (21 dpi). Scale bars 50, 100 and 500 µm. Representative for n=2. (**B-C)** Source data are provided as a Source Data file.

Fig. 7: In tumours, cDCs adopt a mature or ISG phenotype and neutrophils show an increased hypoxic signature. (A) UMAP of DC subsets (subclustered from Fig. 2B) from SUBCUT and ORTHO-T/-A/-M. **(B)** UMAP of DC subsets split across different sample types and their intratissue/vascular origin. Bar charts illustrate the cell composition as percentage within DC subset per sample type. Data averaged over n=4 and rescaled to a total of 100% per sample type. **(C)** Spatial distribution of DC subsets in VIZ1 (left). Density plot of each subset in function of distance to the tumour core. Bar chart showing the percentage of each subset within total DCs split across tumour or adjacent tissue (783 and 446 cells resp.; right). **(D)** ISG signature score (Rsad2, Ifit1, Ifit3, Cxcl10, Isg15, Oasl2, Oas3) on the full immune UMAP from Fig. 2B. **(E)** UMAP of neutrophil subsets (subclustered from Fig. 2B) from SUBCUT and ORTHO-T/-A/-M. **(F)** UMAP of neutrophil subsets split across different sample types and their intratissue/vascular origin. Bar charts illustrate the cell composition as percentage within neutrophil subset per sample type. Data averaged over n=4 and rescaled to a total of 100% per sample type. **(G)** Spatial distribution of neutrophil subsets in VIZ1 (left). Density plot of each subset in function of distance to the tumour core. Bar chart showing the percentage of each subset within total neutrophils split across tumour or adjacent tissue (674 and 276 cells resp.; right). **(B-C, F-G)** Source data are provided as a Source Data file.

Fig. 8: Monocyte/macrophage analysis reveals heterogeneity across models, with Lipid TAMs as the main TAM subset in ORTHO-T. (A) UMAP of AM subsets (subclustered from Fig. 2B) from ORTHO-T/-A/-M. **(B)** Spatial distribution of monocyte/macrophage subsets in VIZ1 (left). Density plot of each subset in function of distance to the tumour core. Bar chart showing the percentage of each subset within total macrophages split across tumour or adjacent tissue (6,093 and 1,633 cells resp.; right). **(C)** UMAP of monocyte/macrophage subsets (subclustered from Fig. 2B, excluding AMs) from SUBCUT and ORTHO-T/-A/-M. **(D)** UMAP of monocyte/macrophage subsets split across different sample types and their intratissue/vascular origin. Bar charts illustrate the cell composition as percentage within T/NK/ILC subset per sample type. Data averaged over n=4 and rescaled to a total of 100% per sample type. **(E)** UMAP of TAM subsets (subclustered from Fig. 8D) from ORTHO-T. Mouse icon created in BioRender. Laoui, D. (2026) https://BioRender.com/whcotzr. **(F)** UMAP of TAM subsets (subclustered from Fig. 6D) from SUBCUT. Mouse icon created in BioRender. Laoui, D. (2026) https://BioRender.com/vsy9o7g. **(B, D-F)** Source data are provided as a Source Data file.

Fig. 9: Spatial transcriptomics reveals Lipid-TAM- and ISG-niches in lung tumours. (A) Spatial distribution of cellular niches (Niche_1 to Niche_11) in VIZ1. “Other” designates non-assigned cells. **(B)**

Neighbourhood plot showing the enrichment of specific immune and non-immune cell subsets across the different niches. Normalised within a cell subset (row). **(C)** Neighbourhood plot showing the distribution of specific immune and non-immune cell subsets across the different niches. Normalised within a niche (column). Values represent the percentage of specific cell subsets within the niche. '%' column represents the percentage of a cell subset within the total number of cells (15,580 cells). Sum (∑) rows represent the fraction of total immune (I) or non-immune (NI) cells within a niche. **(D)** Spatial expression of different ISGs in VIZ1 (n=1). **(E)** Spatial expression of different ISGs in a NSCLC patient sample (Xenium, n=1). Dotted line delineates adjacent (A) from tumour (T) tissue. **(F)** Expression of the ISG signature (RSAD2, ISG15, OAS3, CXCL10, IFIT1, OASL, MX1, CXCL9) in LUAD tumours (T; n=483) and non-tumoural (NT; n=347) lung samples. Boxplot showing the distribution of $\log_2$FC(TPM+1) expression per tissue type. Centre of the boxplot is the median, lower and upper boundaries are Q1 and Q3 respectively. Whiskers represent the 1.5 interquartile range. TPM, transcripts per million. **(B-C)** Source data are provided as a Source Data file.

Fig. 10: Therapy responsiveness of ORTHO and SUBCUT tumour models. (A) Schematic overview of the injection regimen. Created in BioRender. Laoui, D. (2026) https://BioRender.com/lsuihxr. **(B)** Kaplan-Meier plot of survival of ORTHO tumour-bearing mice treated with isotype and vehicle (0.9% saline) (control group), cisplatin (cis) and isotype, anti-PD-1 (αPD-1) and vehicle or combination therapy (n=12 per group). Therapy started upon confirming tumour foci presence by µCT. **(C)** Kaplan-Meier plot of survival of SUBCUT tumour-bearing mice treated with isotype and vehicle (control group), cisplatin and isotype, αPD-1 and vehicle or combination therapy (n=7 per group). Therapy started at 11 days post-inoculation (dpi) (average tumour size ±100 mm^3). Dpt, days post treatment. **(B-C)** Log-rank (Mantel-Cox) tests were performed. *p≤0.05, **p≤0.01, ***p≤0.001, ****p≤0.0001. Source data are provided as a Source Data file.

Editor's Summary

Single-cell transcriptomics has improved the characterisation of pre-clinical tumour models. Here, the authors present a method to distinguish vascular from intratissue cells for single-cell transcriptomics, apply it to an orthotopic lung adenocarcinoma (LUAD) mouse model and use spatial transcriptomics to map these populations and identify distinct immune niches within the tumours.

Peer Review Information: *Nature Communications* thanks Leng Han, who co-reviewed with Yamei Chen; and the other, anonymous, reviewer(s) for their contribution to the peer review of this work. A peer review file is available.

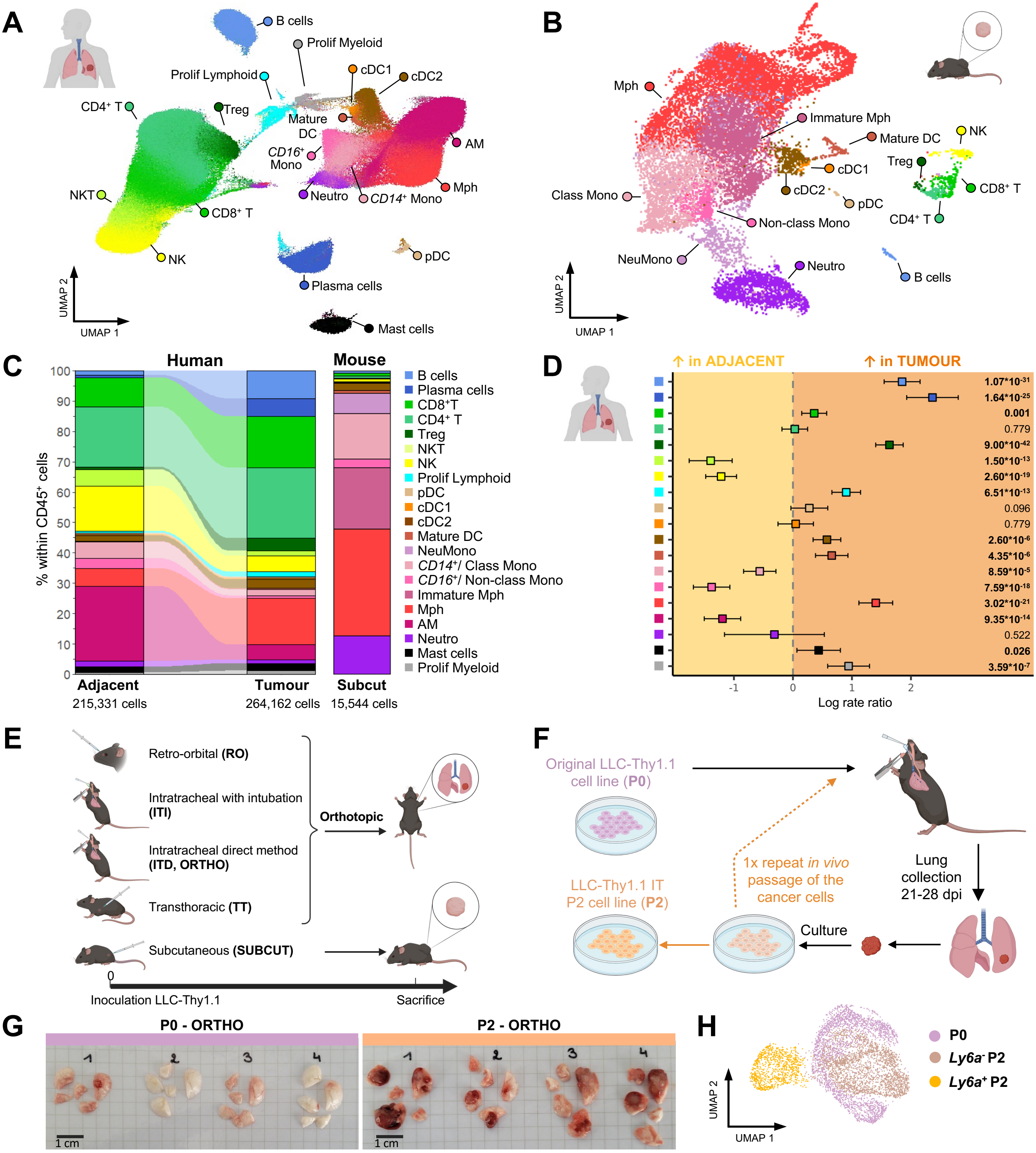
A
B cells
Prolif Myeloid
Prolif Lymphoid
cDC1
cDC2
CD4⁺ T
Treg
Mature DC
AM
CD16⁺ Mono
NKT
CD8⁺ T
Neutro
CD14⁺ Mono
Mph
NK
pDC
Plasma cells
Mast cells
UMAP 2
UMAP 1
B
Mph
Immature Mph
Mature DC
NK
Treg
cDC1
CD8⁺ T
Class Mono
cDC2
pDC
Non-class Mono
CD4⁺ T
NeuMono
Neutro
B cells
UMAP 2
UMAP 1
C
Human
Mouse
% within CD45⁺ cells
0
10
20
30
40
50
60
70
80
90
100
Adjacent
215,331 cells
Tumour
264,162 cells
Subcut
15,544 cells
B cells
Plasma cells
CD8⁺T
CD4⁺ T
Treg
NKT
NK
Prolif Lymphoid
pDC
cDC1
cDC2
Mature DC
NeuMono
CD14⁺/ Class Mono
CD16⁺/ Non-class Mono
Immature Mph
Mph
AM
Neutro
Mast cells
Prolif Myeloid
D
↑ in ADJACENT
↑ in TUMOUR
1.07*10⁻³¹
1.64*10⁻²⁵
0.001
0.779
9.00*10⁻⁴²
1.50*10⁻¹³
2.60*10⁻¹⁹
6.51*10⁻¹³
0.096
0.779
2.60*10⁻⁶
4.35*10⁻⁶
8.59*10⁻⁵
7.59*10⁻¹⁸
3.02*10⁻²¹
9.35*10⁻¹⁴
0.522
0.026
3.59*10⁻⁷
-1
0
1
2
Log rate ratio
E
Retro-orbital (RO)
Intratracheal with intubation (ITI)
Intratracheal direct method (ITD, ORTHO)
Transthoracic (TT)
Orthotopic
Subcutaneous (SUBCUT)
0
Inoculation LLC-Thy1.1
Sacrifice
F
Original LLC-Thy1.1 cell line (P0)
Lung collection 21-28 dpi
1x repeat in vivo passage of the cancer cells
LLC-Thy1.1 IT P2 cell line (P2)
Culture
G
P0 - ORTHO
P2 - ORTHO
1
2
3
4
1
2
3
4
1 cm
1 cm
H
P0
Ly6a⁻ P2
Ly6a⁺ P2
UMAP 2
UMAP 1

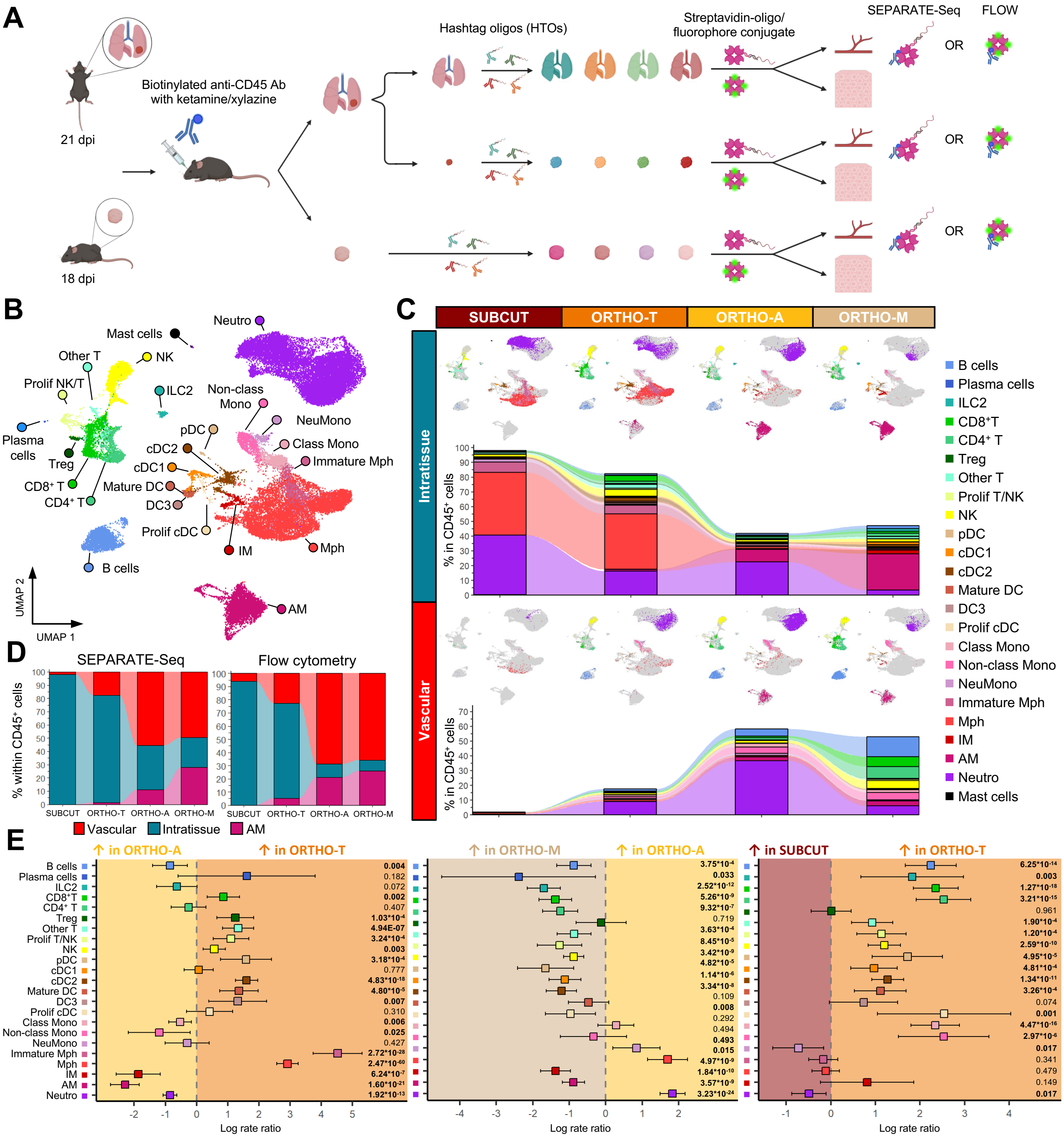
A
21 dpi
18 dpi
Biotinylated anti-CD45 Ab with ketamine/xylazine
Hashtag oligos (HTOs)
Streptavidin-oligo/ fluorophore conjugate
SEPARATE-Seq
FLOW
OR
B
Mast cells
Neutro
NK
Other T
Prolif NK/T
ILC2
Non-class Mono
NeuMono
Class Mono
Immature Mph
pDC
cDC2
cDC1
Mature DC
DC3
Prolif cDC
IM
Mph
Plasma cells
Treg
CD8⁺ T
CD4⁺ T
B cells
AM
UMAP 2
UMAP 1
C
SUBCUT
ORTHO-T
ORTHO-A
ORTHO-M
Intratissue
Vascular
% in CD45⁺ cells
B cells
Plasma cells
ILC2
CD8⁺T
CD4⁺ T
Treg
Other T
Prolif T/NK
NK
pDC
cDC1
cDC2
Mature DC
DC3
Prolif cDC
Class Mono
Non-class Mono
NeuMono
Immature Mph
Mph
IM
AM
Neutro
Mast cells
D
SEPARATE-Seq
Flow cytometry
% within CD45⁺ cells
SUBCUT
ORTHO-T
ORTHO-A
ORTHO-M
Vascular
Intratissue
AM
E
↑ in ORTHO-A
↑ in ORTHO-T
B cells 0.004
Plasma cells 0.182
ILC2 0.072
CD8⁺T 0.002
CD4⁺ T 0.407
Treg 1.03*10⁻⁴
Other T 4.94E-07
Prolif T/NK 3.24*10⁻⁴
NK 0.003
pDC 3.18*10⁻⁴
cDC1 0.777
cDC2 4.83*10⁻¹⁸
Mature DC 4.80*10⁻⁵
DC3 0.007
Prolif cDC 0.310
Class Mono 0.006
Non-class Mono 0.025
NeuMono 0.427
Immature Mph 2.72*10⁻²⁸
Mph 2.47*10⁻⁶⁰
IM 6.24*10⁻⁷
AM 1.60*10⁻²¹
Neutro 1.92*10⁻¹³
Log rate ratio
↑ in ORTHO-M
↑ in ORTHO-A
3.75*10⁻⁴
0.033
2.52*10⁻¹²
5.26*10⁻⁹
9.32*10⁻⁷
0.719
3.63*10⁻⁴
8.45*10⁻⁵
3.42*10⁻⁹
4.82*10⁻⁵
1.14*10⁻⁶
3.34*10⁻⁸
0.109
0.008
0.292
0.494
0.493
0.015
4.97*10⁻⁹
1.84*10⁻¹⁰
3.57*10⁻⁹
3.23*10⁻²⁴
Log rate ratio
↑ in SUBCUT
↑ in ORTHO-T
6.25*10⁻¹⁴
0.003
1.27*10⁻¹⁸
3.21*10⁻¹⁵
0.961
1.90*10⁻⁴
1.20*10⁻⁴
2.59*10⁻¹⁰
4.95*10⁻⁵
4.81*10⁻⁴
1.34*10⁻¹¹
3.26*10⁻⁴
0.074
0.001
4.47*10⁻¹⁶
2.97*10⁻⁶
0.017
0.341
0.479
0.149
0.017
Log rate ratio

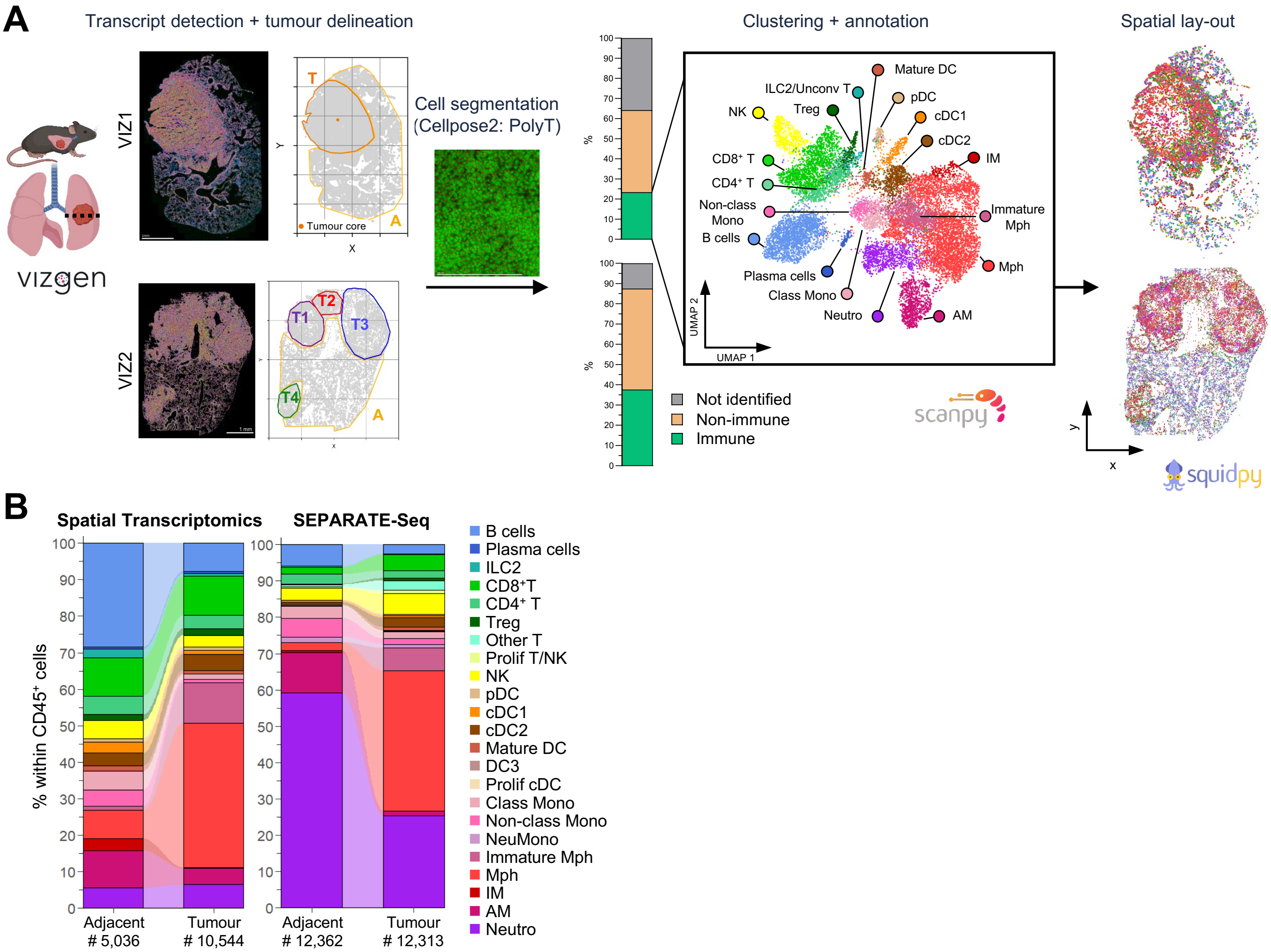
A
Transcript detection + tumour delineation
vizgen
VIZ1
VIZ2
T
A
Tumour core
T1
T2
T3
T4
Y
X
Cell segmentation
(Cellpose2: PolyT)
Clustering + annotation
%
100
90
80
70
60
50
40
30
20
10
0
Not identified
Non-immune
Immune
Mature DC
ILC2/Unconv T
pDC
NK
Treg
cDC1
cDC2
CD8⁺ T
IM
CD4⁺ T
Non-class
Mono
Immature
Mph
B cells
Mph
Plasma cells
Class Mono
Neutro
AM
UMAP 2
UMAP 1
scanpy
Spatial lay-out
y
x
squidpy
B
Spatial Transcriptomics
SEPARATE-Seq
% within CD45⁺ cells
Adjacent
5,036
Tumour
10,544
Adjacent
12,362
Tumour
12,313
B cells
Plasma cells
ILC2
CD8⁺T
CD4⁺ T
Treg
Other T
Prolif T/NK
NK
pDC
cDC1
cDC2
Mature DC
DC3
Prolif cDC
Class Mono
Non-class Mono
NeuMono
Immature Mph
Mph
IM
AM
Neutro

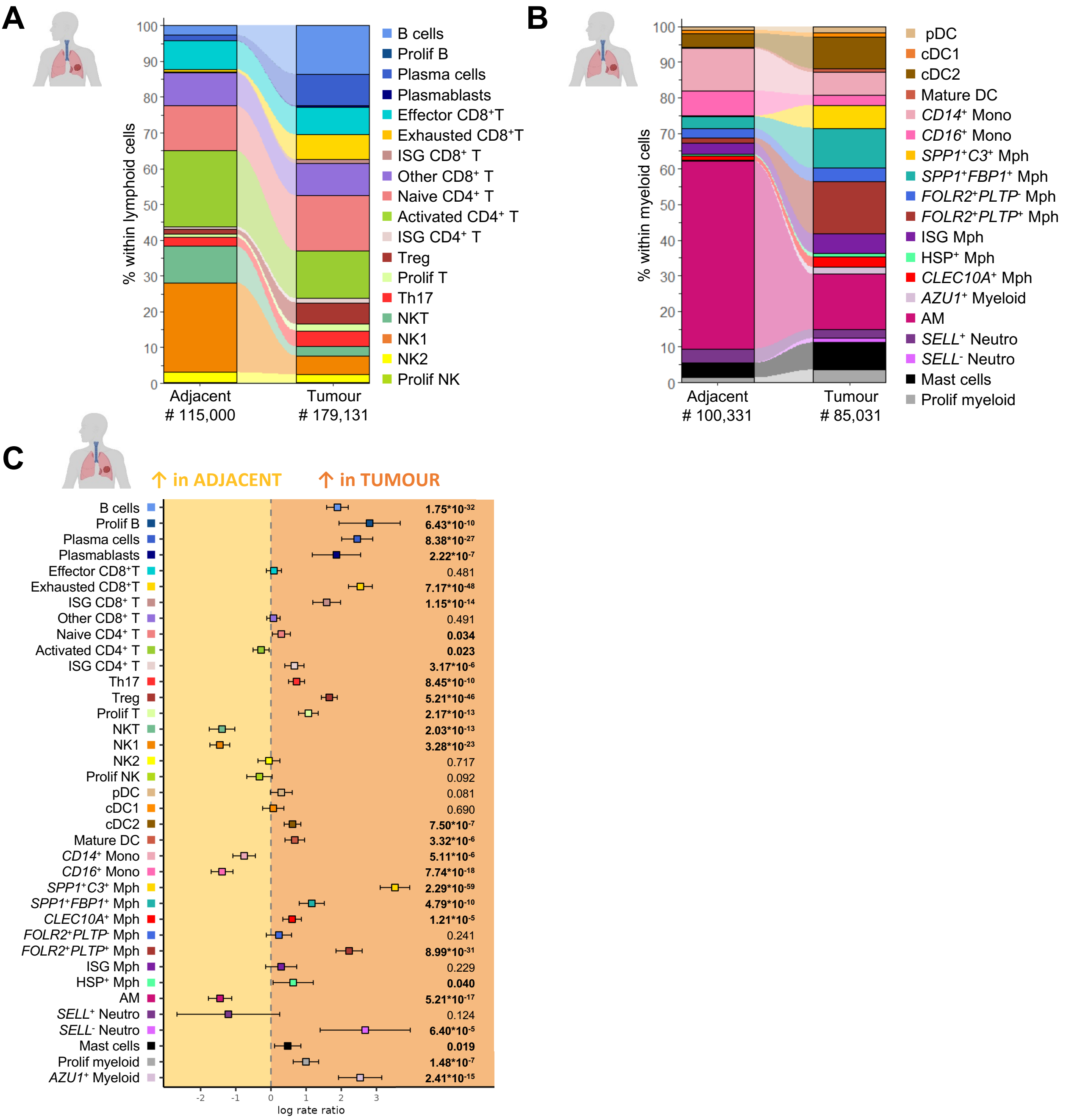
A
% within lymphoid cells
100
90
80
70
60
50
40
30
20
10
0
Adjacent
115,000
Tumour
179,131
B cells
Prolif B
Plasma cells
Plasmablasts
Effector CD8⁺T
Exhausted CD8⁺T
ISG CD8⁺ T
Other CD8⁺ T
Naive CD4⁺ T
Activated CD4⁺ T
ISG CD4⁺ T
Treg
Prolif T
Th17
NKT
NK1
NK2
Prolif NK
B
% within myeloid cells
Adjacent
100,331
Tumour
85,031
pDC
cDC1
cDC2
Mature DC
CD14⁺ Mono
CD16⁺ Mono
SPP1⁺C3⁺ Mph
SPP1⁺FBP1⁺ Mph
FOLR2⁺PLTP⁻ Mph
FOLR2⁺PLTP⁺ Mph
ISG Mph
HSP⁺ Mph
CLEC10A⁺ Mph
AZU1⁺ Myeloid
AM
SELL⁺ Neutro
SELL⁻ Neutro
Mast cells
Prolif myeloid
C
↑ in ADJACENT
↑ in TUMOUR
B cells 1.75*10-32
Prolif B 6.43*10-10
Plasma cells 8.38*10-27
Plasmablasts 2.22*10-7
Effector CD8⁺T 0.481
Exhausted CD8⁺T 7.17*10-48
ISG CD8⁺ T 1.15*10-14
Other CD8⁺ T 0.491
Naive CD4⁺ T 0.034
Activated CD4⁺ T 0.023
ISG CD4⁺ T 3.17*10-6
Th17 8.45*10-10
Treg 5.21*10-46
Prolif T 2.17*10-13
NKT 2.03*10-13
NK1 3.28*10-23
NK2 0.717
Prolif NK 0.092
pDC 0.081
cDC1 0.690
cDC2 7.50*10-7
Mature DC 3.32*10-6
CD14⁺ Mono 5.11*10-6
CD16⁺ Mono 7.74*10-18
SPP1⁺C3⁺ Mph 2.29*10-59
SPP1⁺FBP1⁺ Mph 4.79*10-10
CLEC10A⁺ Mph 1.21*10-5
FOLR2⁺PLTP⁻ Mph 0.241
FOLR2⁺PLTP⁺ Mph 8.99*10-31
ISG Mph 0.229
HSP⁺ Mph 0.040
AM 5.21*10-17
SELL⁺ Neutro 0.124
SELL⁻ Neutro 6.40*10-5
Mast cells 0.019
Prolif myeloid 1.48*10-7
AZU1⁺ Myeloid 2.41*10-15
-2
-1
0
1
2
3
log rate ratio

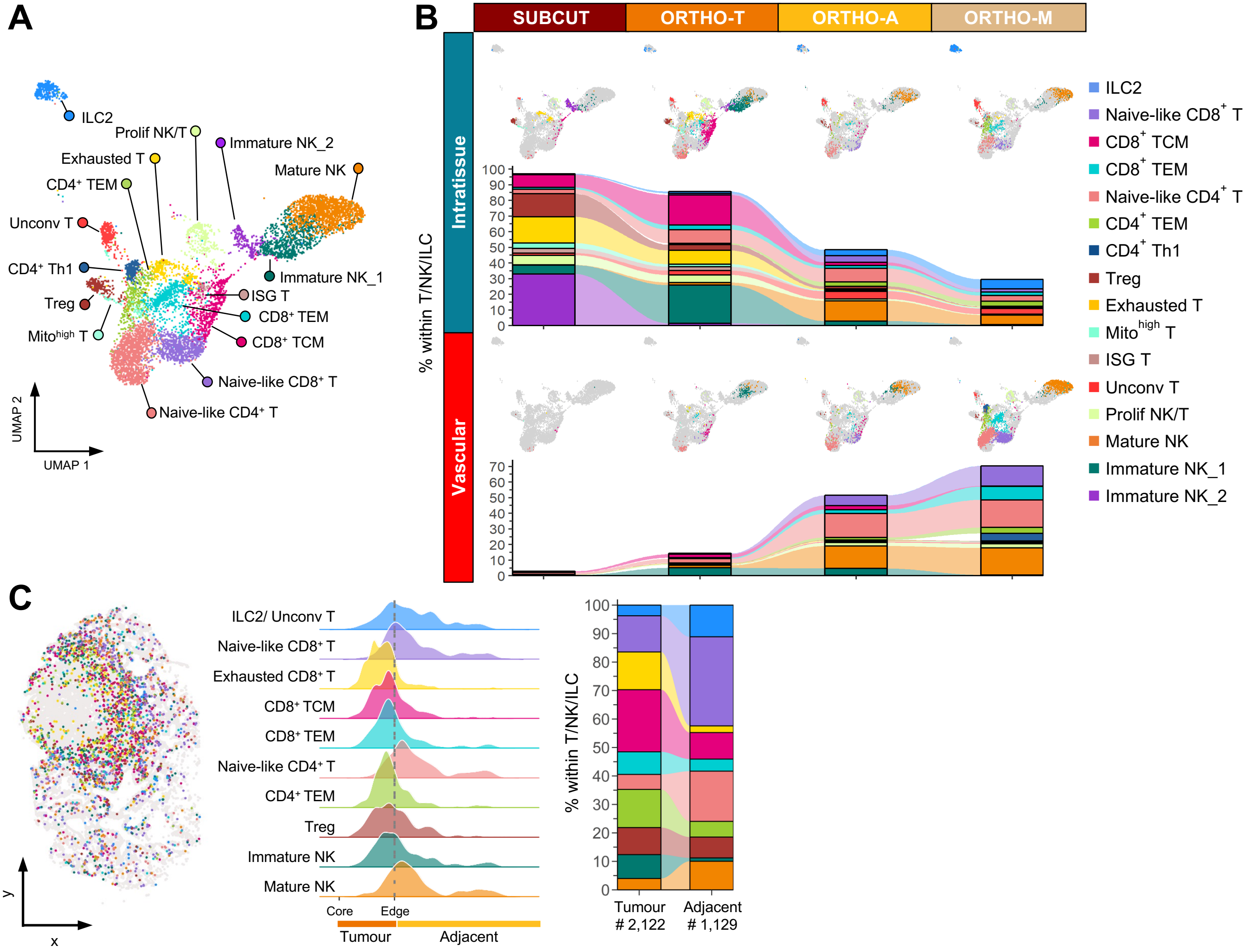
A
ILC2
Prolif NK/T
Immature NK_2
Exhausted T
Mature NK
CD4⁺ TEM
Unconv T
CD4⁺ Th1
Immature NK_1
ISG T
Treg
CD8⁺ TEM
Mito^high T
CD8⁺ TCM
Naive-like CD8⁺ T
Naive-like CD4⁺ T
UMAP 2
UMAP 1
B
SUBCUT
ORTHO-T
ORTHO-A
ORTHO-M
Intratissue
Vascular
% within T/NK/ILC
100
90
80
70
60
50
40
30
20
10
0
70
60
50
40
30
20
10
0
ILC2
Naive-like CD8⁺ T
CD8⁺ TCM
CD8⁺ TEM
Naive-like CD4⁺ T
CD4⁺ TEM
CD4⁺ Th1
Treg
Exhausted T
Mito^high T
ISG T
Unconv T
Prolif NK/T
Mature NK
Immature NK_1
Immature NK_2
C
y
x
ILC2/ Unconv T
Naive-like CD8⁺ T
Exhausted CD8⁺ T
CD8⁺ TCM
CD8⁺ TEM
Naive-like CD4⁺ T
CD4⁺ TEM
Treg
Immature NK
Mature NK
Core
Edge
Tumour
Adjacent
% within T/NK/ILC
100
90
80
70
60
50
40
30
20
10
0
Tumour
2,122
Adjacent
1,129

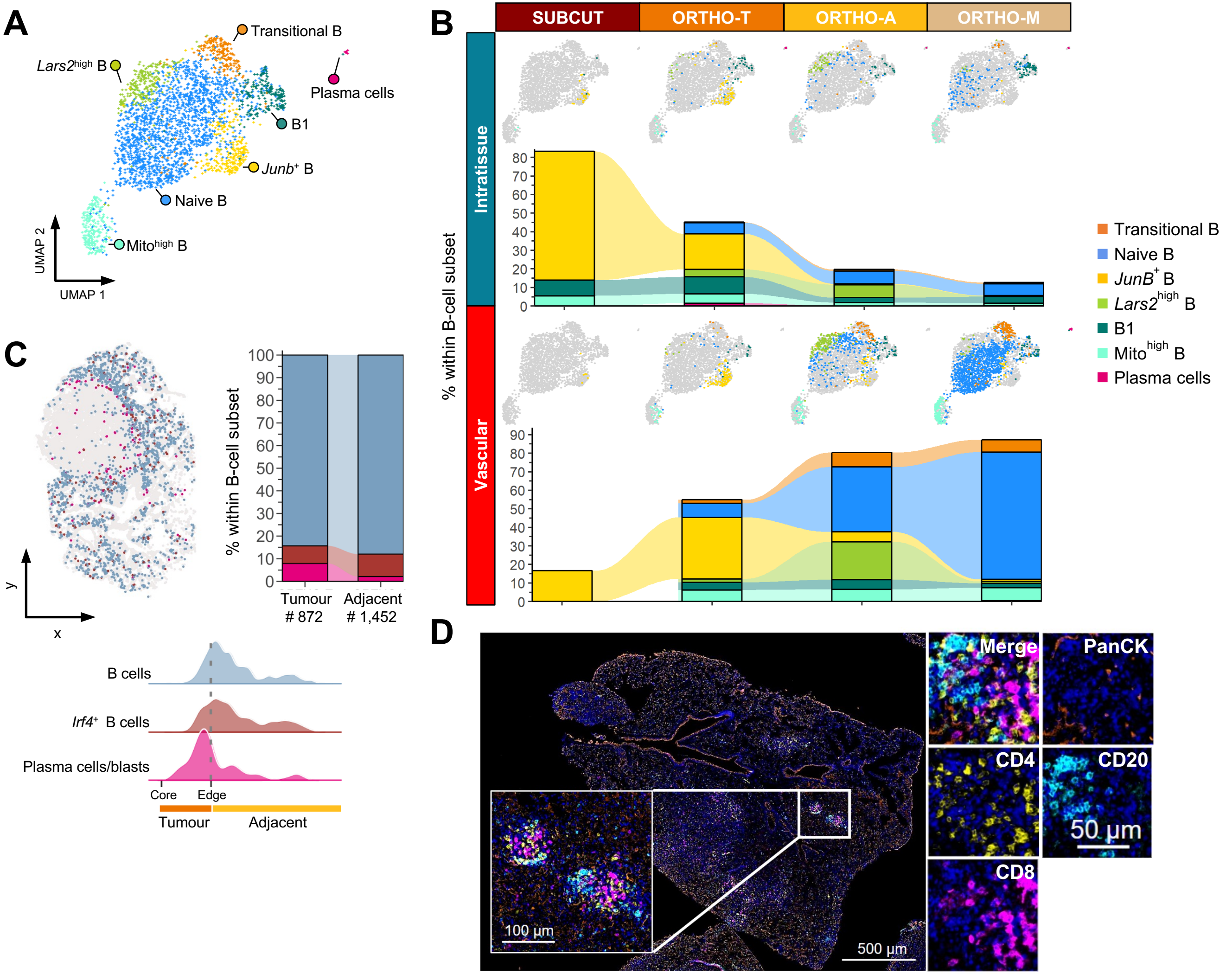
A
Transitional B
*Lars2*high B
Plasma cells
B1
Junb+ B
Naive B
Mitohigh B
UMAP 2
UMAP 1
B
SUBCUT
ORTHO-T
ORTHO-A
ORTHO-M
Intratissue
Vascular
% within B-cell subset
80
70
60
50
40
30
20
10
0
90
Transitional B
Naive B
JunB+ B
*Lars2*high B
B1
Mitohigh B
Plasma cells
C
y
x
% within B-cell subset
100
90
80
70
60
50
40
30
20
10
0
Tumour
872
Adjacent
1,452
B cells
Irf4+ B cells
Plasma cells/blasts
Core
Edge
Tumour
Adjacent
D
Merge
PanCK
CD4
CD20
CD8
50 µm
100 µm
500 µm

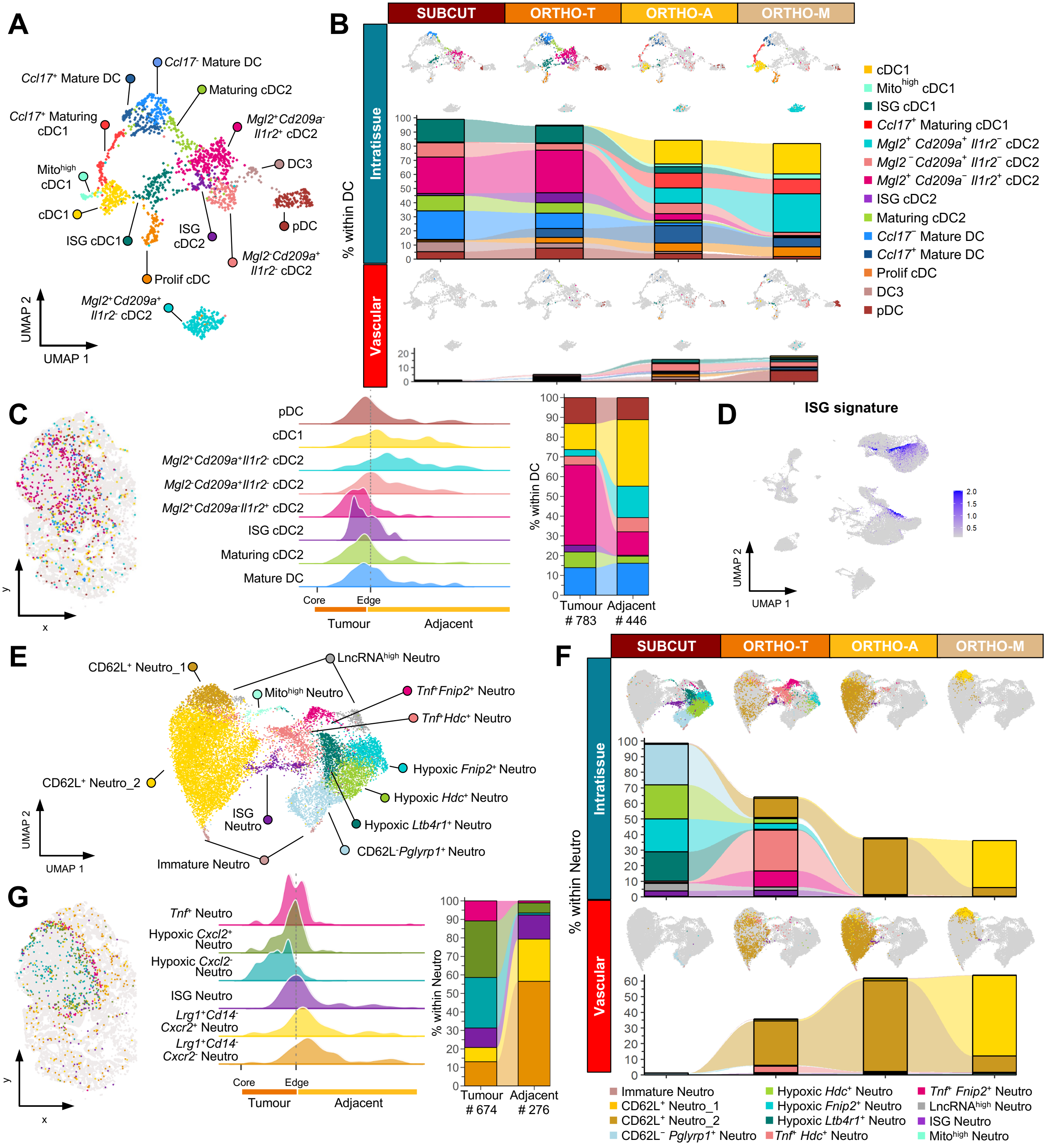
A
Ccl17- Mature DC
Ccl17+ Mature DC
Maturing cDC2
Ccl17+ Maturing cDC1
Mgl2+Cd209a- Il1r2+ cDC2
DC3
Mitohigh cDC1
cDC1
pDC
ISG cDC1
ISG cDC2
Mgl2-Cd209a+ Il1r2- cDC2
Prolif cDC
Mgl2+Cd209a+ Il1r2- cDC2
UMAP 2
UMAP 1
B
SUBCUT
ORTHO-T
ORTHO-A
ORTHO-M
Intratissue
Vascular
% within DC
100
90
80
70
60
50
40
30
20
10
0
cDC1
Mitohigh cDC1
ISG cDC1
Ccl17+ Maturing cDC1
Mgl2+ Cd209a+ Il1r2− cDC2
Mgl2− Cd209a+ Il1r2− cDC2
Mgl2+ Cd209a− Il1r2+ cDC2
ISG cDC2
Maturing cDC2
Ccl17− Mature DC
Ccl17+ Mature DC
Prolif cDC
DC3
pDC
C
pDC
cDC1
Mgl2+Cd209a+Il1r2- cDC2
Mgl2-Cd209a+Il1r2- cDC2
Mgl2+Cd209a-Il1r2+ cDC2
ISG cDC2
Maturing cDC2
Mature DC
Core
Edge
Tumour
Adjacent
% within DC
Tumour
783
Adjacent
446
y
x
D
ISG signature
2.0
1.5
1.0
0.5
UMAP 2
UMAP 1
E
CD62L+ Neutro_1
LncRNAhigh Neutro
Mitohigh Neutro
Tnf+Fnip2+ Neutro
Tnf+Hdc+ Neutro
CD62L+ Neutro_2
Hypoxic Fnip2+ Neutro
Hypoxic Hdc+ Neutro
ISG Neutro
Hypoxic Ltb4r1+ Neutro
CD62L-Pglyrp1+ Neutro
Immature Neutro
UMAP 2
UMAP 1
F
SUBCUT
ORTHO-T
ORTHO-A
ORTHO-M
Intratissue
Vascular
% within Neutro
Immature Neutro
CD62L+ Neutro_1
CD62L+ Neutro_2
CD62L− Pglyrp1+ Neutro
Hypoxic Hdc+ Neutro
Hypoxic Fnip2+ Neutro
Hypoxic Ltb4r1+ Neutro
Tnf+ Hdc+ Neutro
Tnf+ Fnip2+ Neutro
LncRNAhigh Neutro
ISG Neutro
Mitohigh Neutro
G
Tnf+ Neutro
Hypoxic Cxcl2+ Neutro
Hypoxic Cxcl2- Neutro
ISG Neutro
Lrg1+Cd14- Cxcr2+ Neutro
Lrg1+Cd14- Cxcr2- Neutro
Core
Edge
Tumour
Adjacent
% within Neutro
Tumour
674
Adjacent
276
y
x

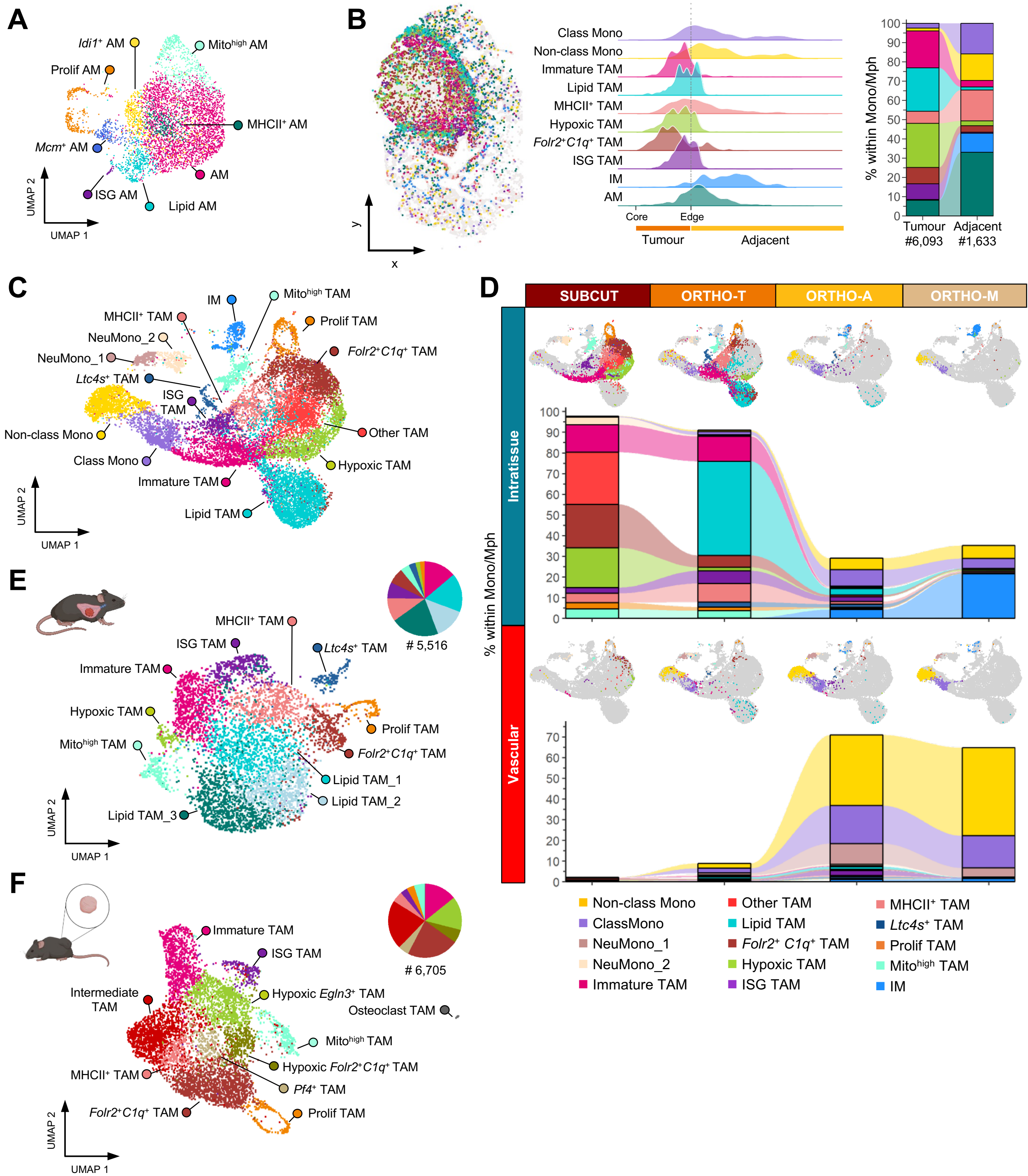
A
Idi1⁺ AM
Mito^high AM
Prolif AM
MHCII⁺ AM
Mcm⁺ AM
AM
ISG AM
Lipid AM
UMAP 2
UMAP 1
B
y
x
Class Mono
Non-class Mono
Immature TAM
Lipid TAM
MHCII⁺ TAM
Hypoxic TAM
Folr2⁺C1q⁺ TAM
ISG TAM
IM
AM
Core
Edge
Tumour
Adjacent
% within Mono/Mph
100
90
80
70
60
50
40
30
20
10
0
Tumour #6,093
Adjacent #1,633
C
IM
Mito^high TAM
MHCII⁺ TAM
Prolif TAM
NeuMono_2
Folr2⁺C1q⁺ TAM
NeuMono_1
Ltc4s⁺ TAM
ISG TAM
Non-class Mono
Other TAM
Class Mono
Hypoxic TAM
Immature TAM
Lipid TAM
UMAP 2
UMAP 1
D
SUBCUT
ORTHO-T
ORTHO-A
ORTHO-M
Intratissue
Vascular
% within Mono/Mph
100
90
80
70
60
50
40
30
20
10
0
70
60
50
40
30
20
10
0
🟨 Non-class Mono
🟪 ClassMono
🟫 NeuMono_1
🟧 NeuMono_2
🟥 Immature TAM
🟥 Other TAM
🟦 Lipid TAM
🟫 Folr2⁺ C1q⁺ TAM
🟩 Hypoxic TAM
🟪 ISG TAM
🟥 MHCII⁺ TAM
🟦 Ltc4s⁺ TAM
🟧 Prolif TAM
🟩 Mito^high TAM
🟦 IM
E
5,516
MHCII⁺ TAM
ISG TAM
Ltc4s⁺ TAM
Immature TAM
Hypoxic TAM
Prolif TAM
Mito^high TAM
Folr2⁺C1q⁺ TAM
Lipid TAM_1
Lipid TAM_2
Lipid TAM_3
UMAP 2
UMAP 1
F
Immature TAM
6,705
ISG TAM
Intermediate TAM
Hypoxic Egln3⁺ TAM
Osteoclast TAM
Mito^high TAM
Hypoxic Folr2⁺C1q⁺ TAM
MHCII⁺ TAM
Pf4⁺ TAM
Folr2⁺C1q⁺ TAM
Prolif TAM
UMAP 2
UMAP 1

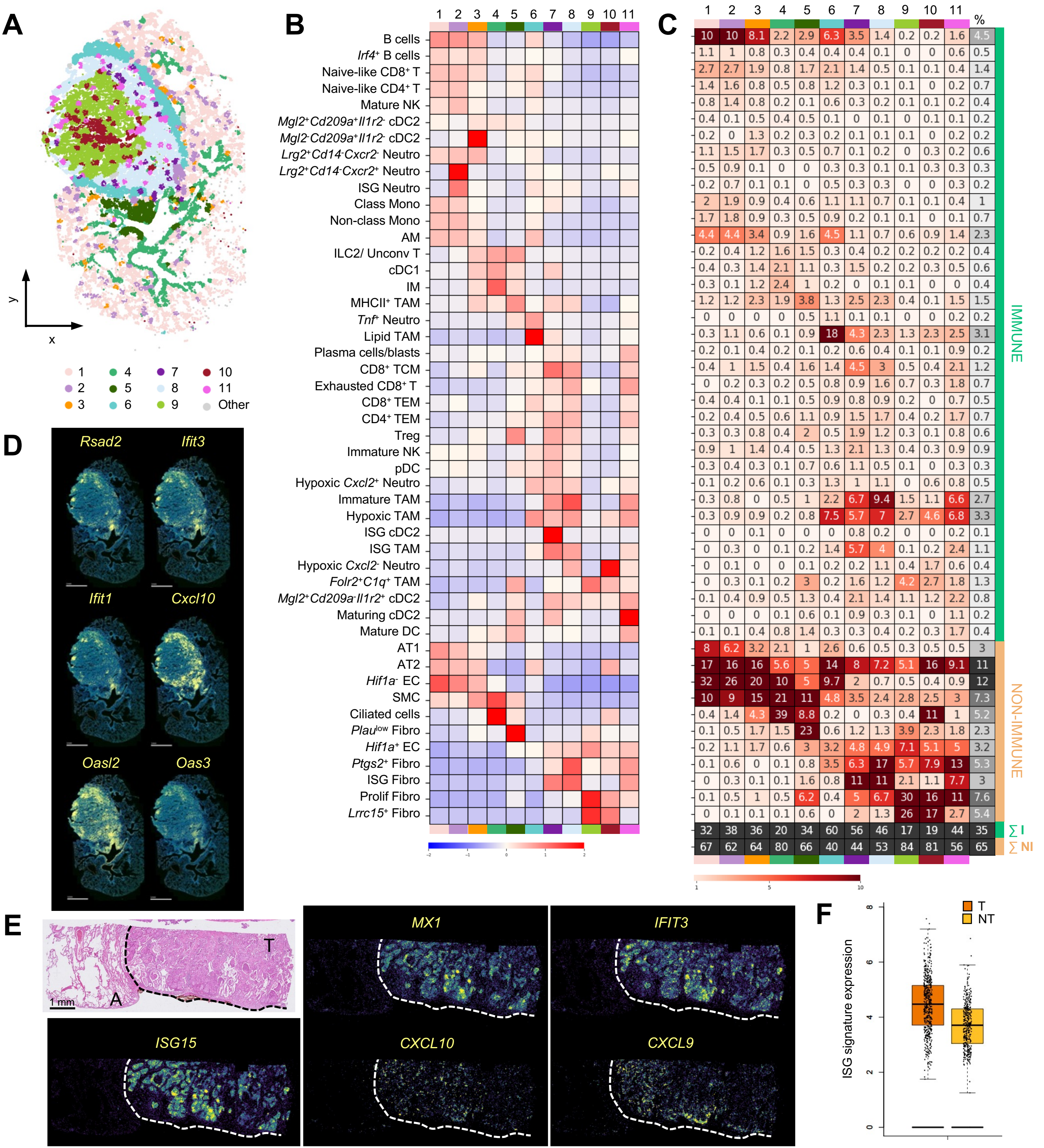

	1	2	3	4	5	6	7	8	9	10	11	%	
B cells	10	10	8.1	2.2	2.9	6.3	3.5	1.4	0.2	0.2	1.6	4.5	IMMUNE
Irf4^{+} B cells	1.1	1	0.8	0.3	0.4	0.4	0.4	0.1	0	0	0.6	0.5	
Naive-like CD8^{+} T	2.7	2.7	1.9	0.8	1.7	2.1	1.4	0.5	0.1	0.1	0.4	1.4	
Naive-like CD4^{+} T	1.4	1.6	0.8	0.5	0.8	1.2	0.3	0.1	0.1	0	0.2	0.7	
Mature NK	0.8	1.4	0.8	0.2	0.1	0.6	0.3	0.2	0.1	0.1	0.2	0.4	
Mgl2^{+}*Cd209a*$^{+}$*Il1r2*$^{-}$ cDC2	0.4	0.1	0.5	0.4	0.5	0.1	0	0.1	0	0.1	0.1	0.2	
Mgl2^{-}*Cd209a*$^{+}$*Il1r2*$^{-}$ cDC2	0.2	0	1.3	0.2	0.3	0.2	0.1	0.1	0.1	0	0.2	0.2	
Lrg2^{+}*Cd14*$^{-}$*Cxcr2*$^{-}$ Neutro	1.1	1.5	1.7	0.3	0.5	0.7	0.1	0.2	0	0.3	0.2	0.6	
Lrg2^{+}*Cd14*$^{-}$*Cxcr2*$^{+}$ Neutro	0.5	0.9	0.1	0	0	0.3	0.3	0.1	0.1	0.3	0.3	0.3	
ISG Neutro	0.2	0.7	0.1	0.1	0	0.5	0.3	0.3	0	0	0.3	0.2	
Class Mono	2	1.9	0.9	0.4	0.6	1.1	1.1	0.7	0.1	0.1	0.4	1	
Non-class Mono	1.7	1.8	0.9	0.3	0.5	0.9	0.2	0.1	0.1	0	0.1	0.7	
AM	4.4	4.4	3.4	0.9	1.6	4.5	1.1	0.7	0.6	0.9	1.4	2.3	
ILC2/ Unconv T	0.2	0.4	1.2	1.6	1.5	0.3	0.4	0.2	0.2	0.2	0.2	0.4	
cDC1	0.4	0.3	1.4	2.1	1.1	0.3	1.5	0.2	0.2	0.3	0.5	0.6	
IM	0.3	0.1	1.2	2.4	1	0.2	0	0.1	0.1	0	0	0.4	
MHCII^{+} TAM	1.2	1.2	2.3	1.9	3.8	1.3	2.5	2.3	0.4	0.1	1.5	1.5	
Tnf^{+} Neutro	0	0	0	0	0.5	1.1	0.1	0.1	0	0	0.2	0.2	
Lipid TAM	0.3	1.1	0.6	0.1	0.9	18	4.3	2.3	1.3	2.3	2.5	3.1	
Plasma cells/blasts	0.2	0.1	0.4	0.2	0.1	0.2	0.6	0.4	0.1	0.1	0.9	0.2	
CD8^{+} TCM	0.4	1	1.5	0.4	1.6	1.4	4.5	3	0.5	0.4	2.1	1.2	
Exhausted CD8^{+} T	0	0.2	0.3	0.2	0.5	0.8	0.9	1.6	0.7	0.3	1.8	0.7	
CD8^{+} TEM	0.4	0.4	0.1	0.1	0.5	0.9	0.8	0.9	0.2	0	0.7	0.5	
CD4^{+} TEM	0.2	0.4	0.5	0.6	1.1	0.9	1.5	1.7	0.4	0.2	1.7	0.7	
Treg	0.3	0.3	0.8	0.4	2	0.5	1.9	1.2	0.3	0.1	0.8	0.6	
Immature NK	0.9	1	1.4	0.4	0.5	1.3	2.1	1.3	0.4	0.3	0.9	0.9	
pDC	0.3	0.4	0.3	0.1	0.7	0.6	1.1	0.5	0.1	0	0.3	0.3	
Hypoxic *Cxcl2*$^{+}$ Neutro	0.1	0.2	0.6	0.1	0.3	1.3	1	1.1	0	0.6	0.8	0.5	
Immature TAM	0.3	0.8	0	0.5	1	2.2	6.7	9.4	1.5	1.1	6.6	2.7	
Hypoxic TAM	0.3	0.9	0.9	0.2	0.8	7.5	5.7	7	2.7	4.6	6.8	3.3	
ISG cDC2	0	0	0.1	0	0	0	0.8	0.2	0	0	0.2	0.1	
ISG TAM	0	0.3	0	0.1	0.2	1.4	5.7	4	0.1	0.2	2.4	1.1	
Hypoxic *Cxcl2*$^{-}$ Neutro	0	0.1	0	0	0.1	0.2	0.2	1.1	0.4	1.7	0.6	0.4	
Folr2^{+}*C1q*$^{+}$ TAM	0	0.3	0.1	0.2	3	0.2	1.6	1.2	4.2	2.7	1.8	1.3	
Mgl2^{+}*Cd209a*$^{-}$*Il1r2*$^{+}$ cDC2	0.1	0.4	0.9	0.5	1.3	0.4	2.1	1.4	1.1	1.2	2.2	0.8	
Maturing cDC2	0	0	0	0.1	0.6	0.1	0.9	0.3	0.1	0	1.1	0.2	
Mature DC	0.1	0.1	0.4	0.8	1.4	0.3	0.3	0.4	0.2	0.3	1.7	0.4	
AT1	8	6.2	3.2	2.1	1	2.6	0.6	0.5	0.3	0.5	0.5	3	NON-IMMUNE
AT2	17	16	16	5.6	5	14	8	7.2	5.1	16	9.1	11	
Hif1a^{-} EC	32	26	20	10	5	9.7	2	0.7	0.5	0.4	0.9	12	
SMC	10	9	15	21	11	4.8	3.5	2.4	2.8	2.5	3	7.3	
Ciliated cells	0.4	1.4	4.3	39	8.8	0.2	0	0.3	0.4	11	1	5.2	
Plau^{low} Fibro	0.1	0.5	1.7	1.5	23	0.6	1.2	1.3	3.9	2.3	1.8	2.3	
Hif1a^{+} EC	0.2	1.1	1.7	0.6	3	3.2	4.8	4.9	7.1	5.1	5	3.2	
Ptgs2^{+} Fibro	0.1	0.6	0	0.1	0.8	3.5	6.3	17	5.7	7.9	13	5.3	
ISG Fibro	0	0.3	0.1	0.1	1.6	0.8	11	11	2.1	1.1	7.7	3	
Prolif Fibro	0.1	0.5	1	0.5	6.2	0.4	5	6.7	30	16	11	7.6	
Lrrc15^{+} Fibro	0	0.1	0.1	0.1	0.6	0	2	1.3	26	17	2.7	5.4	
	32	38	36	20	34	60	56	46	17	19	44	35	∑ I
	67	62	64	80	66	40	44	53	84	81	56	65	∑ NI

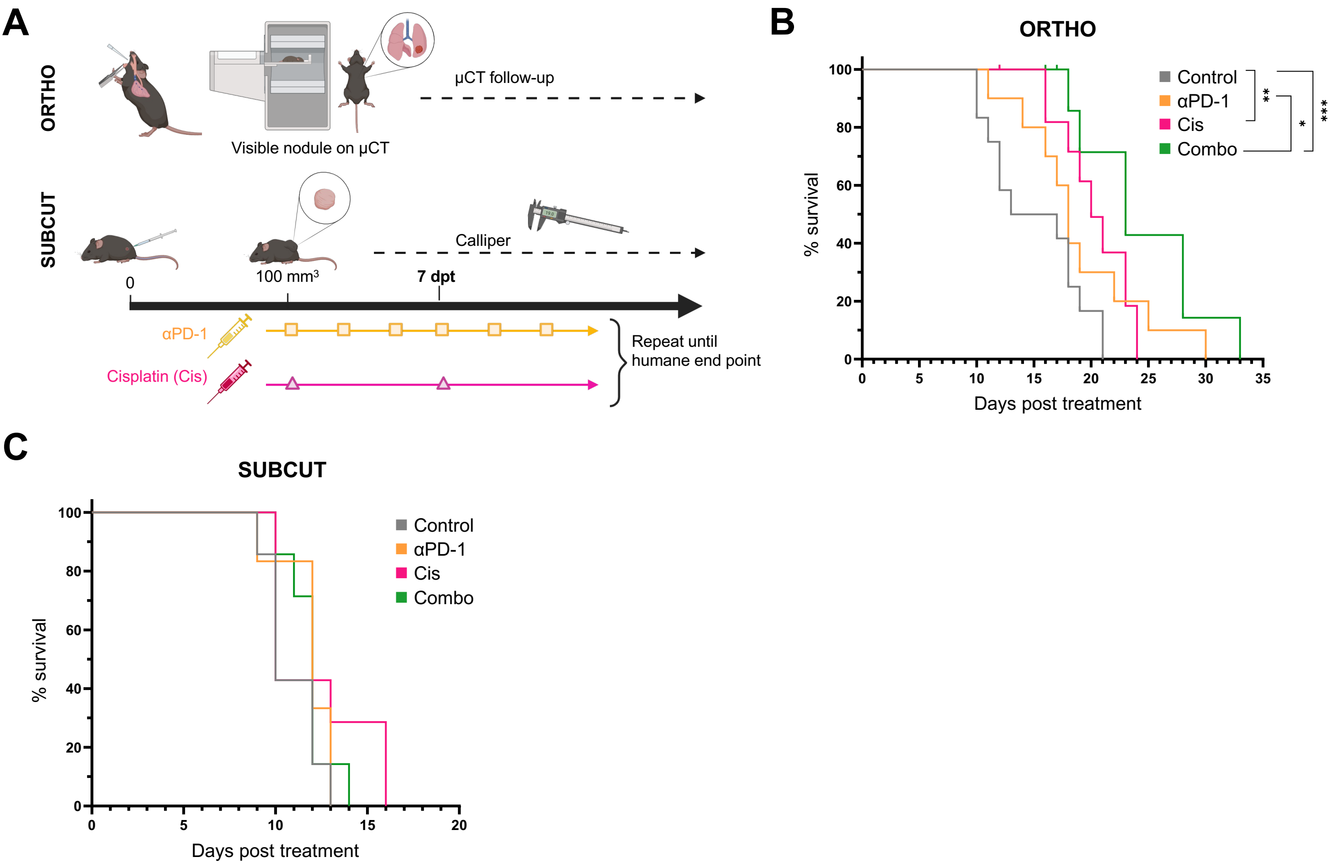
A
ORTHO
Visible nodule on µCT
µCT follow-up
SUBCUT
Calliper
0
100 mm³
7 dpt
αPD-1
Cisplatin (Cis)
Repeat until humane end point
B
ORTHO
% survival
Days post treatment
100
80
60
40
20
0
0
5
10
15
20
25
30
35
Control
αPD-1
Cis
Combo
**
*
***
C
SUBCUT
% survival
Days post treatment
100
80
60
40
20
0
0
5
10
15
20
Control
αPD-1
Cis
Combo